Subject-Specific Modeling of Human Facet Capsular Ligament

A DISSERTATION
SUBMITTED TO THE FACULTY OF THE
UNIVERSITY OF MINNESOTA
BY

Maryam Nikpasand

IN PARTIAL FULFILLMENT OF THE REQUIREMENTS
FOR THE DEGREE OF
DOCTOR OF PHILOSOPHY

Advised by: Victor Barocas, PhD

August 2022

Acknowledgements

I would like to sincerely thank my advisor, Victor Barocas, for his technical advice and direction as well as his personal support. I thank Victor for being a compassionate advisor and an excellent mentor since our very first meeting when I was thinking about dropping out of graduate school. Thank you, Victor, for believing in me when I did not believe in myself. Thanks for prioritizing my ambitions and goals by constantly asking "what do *you* want to do?" even when I did not have the faintest idea about what I wanted to do. Thanks for helping me grow not only in my academic life but also in all aspects of my life by constantly reminding me by your words and actions that "family and friends are important". Thank you, Victor, for giving me the most enjoyable graduate school experience imaginable.

This work would not have been possible without substantive contributions of many researchers, including, in no particular order, Ryan R. Mahutga, Lauren M. Bersie-Larson, Elizabeth Gacek, Jill M. Middendorf, Jonathan Marcelin, Beth A. Winkelstein, Rebecca Abbott, Craig C. Kage, Sagar Singh, Arin M Ellingson, and Victor Barocas. I appreciate contributions from colleagues in our weekly FCL and shoulder meetings including Matthew MacEwen, Paula Kudewig, Cyrus Rezvanifar, Gaura Saini.

I would like to thank Arin M. Ellingson and Beth A. Winkelstein for taking on the role of unofficial co-advisors and contributing to my education and understanding of spine and providing valuable feedback during my research.

Thank you to members of my committee, Julianna Abel, Patrick Alford, Arin Ellingson, and Victor Barocas, for discussions, constructive feedback, and directions of research. Special thanks to Victor Barocas for providing inspiration, perspective and context for this

research as well as continuous guidance and technical direction during the development of this work.

I would like to express my thanks for friendship. Thank you Hoda Mousavi, Mehran Shams Kondori, Amirsina Torfi, and Sommayeh Yarahmadi for being an incredible family away from home. Thanks to Joshua Punnoose for being my workout buddy though most of our workout sessions ended up being an opportunity to catch up and vent our frustrations in our research. Thanks to my labmates, present and past, including Elizabeth (Liz) Gacek, Jill Middendorf, Marisa Bazzi, Ryan Mahutga, Lauren Bersie-Larson, Carly Donahue, Shannon Flanary (AKA cruise director), Adam Ley, Hadi Wiputra, Shannen Kizilski, Shion Matsumoto for providing continuous support and making the lab a delightful place to work. Thank you Liz and Jill for teaching me a lot about spine and facet capsular ligament and answering my questions whenever I got stuck in a problem. You two were my first resort to seek help. Thank you Marisa for being a compassionate friend who always pushed me to be a better version of myself, whether it was in science or in our weekly volleyball games or even through our shared exercise tracking app. Thank you Ryan and Lauren for providing guidance and teaching me about the multiscale code when I had just joined the lab and did not know anything about it.

Finally, thanks to my husband and partner in crime, Nader Tavaf, for all of his emotional and technical support especially during the last 6 months leading to my graduation. Thank you, Nader, for always being my first motivator to think outside the box and to trust myself.

Last but not least, thanks to my family for all their support from thousand of miles away. Thanks for all the sacrifices that you made so that I can get one step closer to my dreams. Thanks to my dad, Masoud, who never complained about me leaving them to follow my dreams even when that dream put multiple time zones between us. Thanks to my mom, Marzieh, for always reminding me to take life easy, to take time to rest and that it is OK not to be perfect all the time. Thanks to my brother, Amir, for continuous advice on how to approach technically challenging tasks. Thanks to my sister-in-law, Azam, for being there for my family when I was away and could not travel to visit them. Thanks to my niece and nephew, Sara and Ali, for their presence and laughs were heartwarming and an incentive to keep going.

Parts of this work were supported by the National Institutes of Health through the grants U01 AT010326, U54 CA210190, T32 AR050938, U01 HL139471, R03 HD09771, and K12 HD073945. Additionally, parts of this work were supported by the Minnesota Partnership for Biotechnology and Medical Genomics (MHP IF #14.02).

Dedication

To the future stars, my niece and nephew,
Sara and Ali.

Table of Contents

List of Tables

List of Figures

CHAPTER 1

Introduction

Science, for me, gives a partial explanation for life.

Rosalind Franklin

1.1 Background and Motivation

The cervical spine is composed of seven bones (C1 to C7, the first seven vertebrae of the spinal column) separated by intervertebral discs and connected to muscles, ligaments, nerves and tendons that collectively form the human neck, support the head, and, critically, protect the human spinal cord. The wide range of rotation enabled by the cervical spine exposes its components to various injuries that manifest as neck pain. At least one out of three people experiences neck pain at least once a year, resulting in neck pain being recognized as a leading contributor to years lived with disability [1–3]. A diverse range of factors can cause neck pain [4], with injuries to the facet joint and its capsular ligament [3, 5] being the cause of primary interest to this research.

The capsular ligaments, together with the synovium layers, encapsulate the facet joints and serve a diverse range of mechanosensory functionalities. Damage to the facet capsular ligament compromises such mechanosensory capabilities and is, therefore, a prevalent source of neck pain. However, with the exact mechanics of facet joints understudied, limited understanding of these injuries translates into constraints on the long term efficacy of existing non-invasive treatments [3, 5].

1.1.1 Facet Capsular Ligament Structure and Function

The diarthrodial, zygapophysial (also known as facet) joints, along with the intervertebral disc, form the spine functional unit [6]. There are two facet joints on either side of

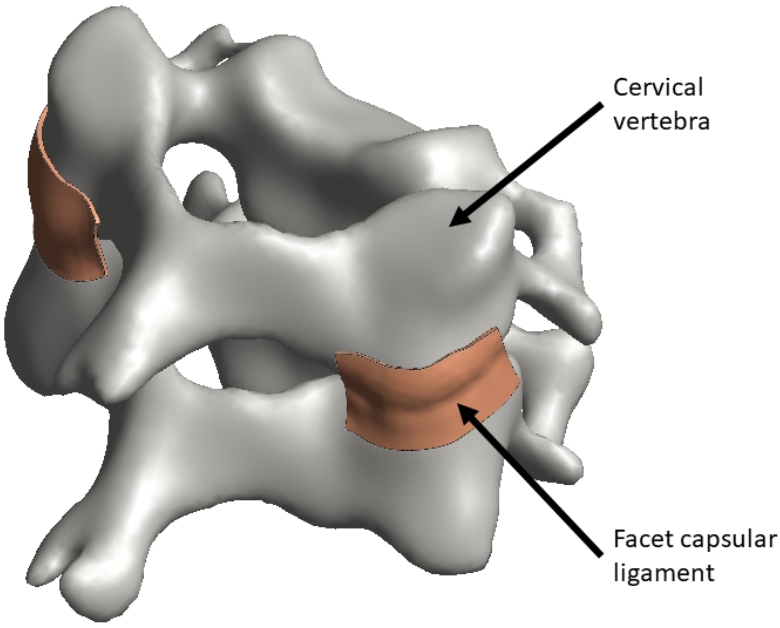

Figure 1.1: Location of cervical facet capsular ligament in a spine motion segment.

each spinal motion segment. The joints are positioned symmetrically with respect to the mid-sagittal plane and connect the superior articular facets of one vertebra to the inferior articular facet of the vertebra above [3, 7, 8], as is shown in Figure 1.1. The geometry and orientation of the facet joints varies with their position from the cervical to the lumbar section of the spine. This variation helps the joints appropriately constrain spinal motion in each level [8]. The facet joints, like all synovial joints, are encapsulated by a ligamentous capsule, called the facet capsular ligament.

The facet capsular ligament plays a variety of mechanical and sensory roles in the spine. Keeping the synovial fluid inside the joint space to ensure joint and cartilage lubrication is the defining role of a capsule. In addition, Izzo et al. [9] argue that the facet capsular ligament orientation in the spine enables it to control and restrict the spinal motion, redirect the load on the spine, and maintain spinal stability. The increase in the range of motion due to facet capsular ligament removal [8, 10] is consistent with that view. Being highly innervated, the facet capsular ligament also plays mechanosensory roles, including propa-

gation of proprioceptive (position) and nociceptive (pain) signals to the brain [11–13] and has been identified as one of the causes of neck pain [7, 12].

Yamashita et al. [12] showed that the facet capsular ligament is composed of two primary layers: the white, strong outer (posterior) side, which is composed of regularly-arranged crimped type-I collagen fibers, and the yellow, extensible inner (anterior) layer of parallel bundles of elastin fibers. The bilayer structure allows the tissue to bear substantial strain in different loading scenarios without damaging the microstructure of the facet capsular ligament [8].

1.1.2 Cervical Facet Capsular Ligament and Neck Pain

Excessive and chronic tension on the axons in the facet capsular ligament due to macroscale ligament elongation is correlated with back and neck pain [8]. The tension is characterized by the magnitude and rate of strain imposed on the tissue [14–16]. Macroscale strains of high magnitude and/or rate can disturb the microstructure surrounding the neurons in the tissue and cause the mechano-sensitive ion channels of the cell membrane to become activated, which can manifest in pain signals [14, 15, 17–19]. The risk of mechanical instability in the spine due to laxity in the joint is associated with repetitive cyclic loading of the facet capsular ligament among other factors, even when the load and corresponding motion are within the normal physiological ranges [20–22]. Microstructural deformations preceding laxity and pain in the tissue are attributed to excessive loading rates on the cervical facet capsular ligament [22–25]. While existing literature establishes a potential correlation between the loading rate and mechanical response of the tissue, it falls short of accurately characterizing the mechanisms by which the macroscale tissue loading rate affects microstructural loading and neuronal response.

1.1.3 Cervical Facet Capsular ligament Characterization

Characterization of mechanical properties of the facet capsular ligament has been the subject of many experimental studies [5, 13, 17, 24, 26–30]. For instance, in their study, Troyer et al. [30] used physiologically relevant cyclic loading conditions to characterize the viscoelastic behavior of the human lower cervical spine ligaments. Their results showed that both magnitude and frequency of the applied strain are consequential in defining the material properties of the human cervical ligaments. The range of motion in axial rotation and lateral flexion of cadaveric cervical spines can also be substantially compromised due to cervical facet capsular ligament injuries [28]. Excessive elongation of the facet capsular ligament beyond the normal physiological range of tissue strain has been shown to correlate with capsular ligament laxity and with the concomitant microstructual deformations in the capsule fiber organization [24, 29, 31]. Whereas experimental data of this sort are useful to characterize the facet capsular ligament tissue as a whole, they cannot define the effect of environmental stimuli on the facet capsular ligament's axonal responses. To better understand the facet capsular ligament's contribution to neck pain, tissue-equivalent gel models involving axons embedded in collagen gels are developed as *in vitro* models of the facet capsular ligament and its embedded neurons [14, 32–34]. These *in vitro* models enable systematic isolation and characterization of the role of various tissue constituents as well as an investigation of the consequences of macroscopic loading on the microstructural reorganization of the collagen network and the neuronal response. Yet, the structural differences between the collagen gel and the facet capsular ligament impose constraints on generalizability/applicability of the insights obtained from gel model experiments to the tissue response. One such key difference is the collagen concentration, which is lower in gels than in tissue and causes variations in matrix stiffness and results in higher axonal outgrowth in gel due to the lower collagen concentration [35, 36]. Neurite survival rate is

also adversely affected by increases in collagen concentration in gels subject to high deformation rates [35]. These studies necessitate that the neuronal stresses and strains resulting from collagen gel-based experiments be adjusted to take into account the differences between the collagen gel and the native tissue before being translated and applied to the native ligament.

Understanding the facet capsular ligament's role in the biomechanical response of the spine further requires characterization of the role of material nonlinearities as well [37–41]. For example, the stiffness of the left C5-C6 cervical capsular ligament was studied in Wang et al.'s investigation of ligament degeneration and its effects on segmental motion [38]. The mechanical characteristics of cervical spine ligaments including the facet capsular ligament under normal physiological strain rates have also been studied in [39] where the macroscopic strain within the tissue was used to characterize and explain its mechanical response. Given the observations that (1) the microscopic structure of the tissue has been shown to affect its macroscopic response [37, 42], and (2) the cervical facet capsular ligament has a heterogeneous collagen fiber structure, the investigation of the complexities of the mechanical response of the cervical facet capsular ligament requires a multiscale approach.

1.1.4 Computation Modeling of Cervical Facet Capsular ligament

Tissue-level heterogeneity of the collagen fiber network in the facet capsular ligament varies due to its anatomical location [43]. It has been shown that the degree of intra- and inter-sample heterogeneity is higher in the cervical facet capsular ligaments compared to the lumbar facet capsular ligaments [43]. These structural differences are more pronounced when the tissue is stretched. Experimental studies have shown that the changes in the structural arrangement of collagen fibers under different loading scenarios or due to the degenerative diseases are major determinants of the facet capsular ligament's me-

chanical and physiological behavior [12, 31, 44–46]. These results suggest that a comprehensive computational characterization of the mechanical behavior of the facet capsular ligament requires incorporation of the fiber orientation into computational models of the tissue. One approach to gain insight into the mechanics of the facet capsular ligament is to develop computational models based on the tissue's underlying structure and perform fully coupled multiscale simulation. Developing a discrete-fiber network model with many fibers presented on the macroscale results in prohibitively high computational expense; therefore, improved efficiency becomes the motivation for developing multiscale models. Multiscale models work based on representative discrete fiber structures, and relates macroscopic behavior to smaller-scale structural network. Barocas and collaborators developed a computational multiscale technique based on this idea to investigate the mechanics of the connective tissue [47, 48]. Using this technique, Zarei et al. developed a multiscale structure-based finite element model of an L4-L5 facet capsular ligament [49]. They extrapolated surface images of collagen fiber alignments through the depth of one generic facet capsular ligament geometry to show that fiber alignment has a significant role in translating facet capsular ligament load to the neuron load metrics. In a relevant study, Zhang and collaborators [37] developed an image-based, subject-specific, multiscale finite element model to predict the mechanical responses of the human cervical facet capsular ligament under uniaxial tensile stretch. They showed that their model can precisely simulate force-displacement response but not the fiber organization at large tissue stretches and, they introduced a potential mechanical basis to predict the failure-prone regions in the intact tissue. Although these multiscale studies have provided useful information on tissue mechanics, for complex geometries and loading scenarios, the computational costs of such simulations can be prohibitive, whereas a closed form constitutive equation model such as Holzapfel-Gasser-Ogden (HGO) [50] or a similar model, that contains microstructural detail, but leverages the speed of classical continuum-based finite-element (FE) modeling,

would be more desirable. This approach will reduce the complexity and computational load of the current multiscale model.

1.1.5 Subject-Specific Model of Human Cervical Facet Capsular Ligament

Although experimental studies have provided useful information on the tissue mechanics in isolation, they fall short of defining the role of the ligament in spinal stability and motion. To understand the facet capsular ligament's contribution to neck biomechanics, we need to investigate its interactions with other spinal components during physiological loading condition. One approach is to develop a finite element model of the spinal motion segment and simulate it with bone kinematics that mimic a realistic neck motion. The objective of such finite element models is to study the motion segment and its components' behaviors under loading conditions that are not feasible in experimental examination [38, 51–56]. Such finite element models can be an intermediate step towards subject-specific models, especially when patient anatomical and kinematic data are obtainable noninvasively, that can form the foundations of decision support systems serving the diagnosis and treatment of cervical injuries

To design an individualized, realistic FE model of cervical facet capsular ligament, all the components of the model must have realistic representations of geometry, material, and motion pattern. Generating subject-specific finite element models of cervical spines is now feasible thanks to recent advances in medical imaging technologies [38, 53, 54, 56–62]. Diagnostic imaging tools, including Computed Tomography (CT) and Magnetic Resonance Imaging (MRI) scans (complemented by postprocessing steps such as segmentation and registration), enable reconstruction of the 3D geometries of vertebrae. However, in previous studies, two-node, nonlinear tension-only truss or spring elements were used to provide a linear 2D model of the cervical ligaments including facet capsular ligament, simplifying the ligament's 3D anatomy [38, 53, 54, 56–59, 63]. An accurate characterization of the

influence of the cervical facet capsular ligament in the biomechanical behavior of the spine requires a higher fidelity volumetric model of the capsular ligament.

A geometrically precise cervical spine model cannot be informative if it does not mimic realistic neck kinematics. 3D cervical spine motion has commonly been simplified to a rotational moment (or a combination of several rotational moments) around the vertebra's center of rotation in previous studies [53, 54, 56–59, 61]. Such over-simplified kinematics ignores the variations in neck motion specific to each individual.

1.2 Research Aims

The overall goal of this dissertation was to develop and employ a numerical methodology to create a 3D, subject-specific, microstructure-based finite element approach for modeling lower cervical spine motion with focus on facet capsular ligament biomechanics. This model accounts for the role of inherent 3D structure of collagen fibers and variations in facet capsular ligament geometry and spine kinematics without the need to solve a complex fully-coupled multiscale model. This research provides a foundation for subject-specific models that can be adopted as a complementary tool in clinical settings to advance prevention, diagnosis, and treatment plans in cervical injuries.

The following three aims were pursued to form this research:

- Aim 1: Construct a hybrid microstructural-continuum multiscale modeling approach that incorporates microstructural details of a heterogeneous tissue, such as the cervical facet capsular ligament, in a continuum finite element-based model to reduce the computational cost relative to a full discrete-fiber multiscale simulation.

- Aim 2: Model the viscoelastic relaxation of an axon embedded in collagen networks with different collagen densities, to investigate the effect of the strain-dependent, viscoelastic micromechanical environment of the axon on the strains within the axon.

- Aim 3: Develop and demonstrate a methodology to create a 3D kinematically-driven, subject-specific, microstructure-based finite element model of the lower cervical spine (C4-C7), and determine 3D deformation profiles on the facet capsular ligament during physiological motion (flexion-extension, lateral bending, and axial rotation).

1.3 Resulting Research

Successful completion of the abovementioned aims has led to three main studies that form the body of my dissertation. A brief overview of each chapter follows below:

Chapter 2: A Hybrid Microstructural-Continuum Multiscale Approach for Modeling Hyperelastic Fibrous Soft Tissue [64]

The heterogeneous, nonlinear, anisotropic material behavior of biological tissues makes precise definition of an accurate constitutive model difficult. One possible solution to this issue would be to define microstructural elements and perform fully coupled multiscale simulation. However, for complex geometries and loading scenarios, the computational costs of such simulations can be prohibitive. Ideally then, we should seek a method that contains microstructural detail, but leverages the speed of classical continuum-based finite-element (FE) modeling. In this work, we demonstrate the use of the Holzapfel-Gasser-Ogden (HGO) model [50, 65] to fit the behavior of microstructural network models. We show that Delaunay microstructural networks can be fit to the HGO strain energy function by calculating fiber network strain energy and average fiber stretch ratio. We then use the HGO constitutive model in a FE framework to improve the speed of our hybrid model, and demonstrate that this method, combined with a material property update scheme, can match a full multiscale simulation. This method gives us flexibility in defining complex FE simulations that would be impossible, or at least prohibitively time consuming, in multiscale simulation, while still accounting for microstructural heterogeneity.

Chapter 3: Load Transfer from Tissue to Neuron: Computational Analysis of Mechanical Differences between Facet Capsular Ligament and Collagen Gel Experiments [66]

Back and neck pain can be associated with excessive tension on the axons embedded in the facet capsular ligament. This tension is believed to depend on both the magnitude and the rate of strain applied to the tissue, with the details of that dependency a current area of research. The emergence of experimental models involving axons embedded in collagen gels shows a relationship between macroscale tissue strains and nociceptive pain signaling, it but raises the question of how differences between collagen gel mechanics and tissue mechanics could affect the resulting strain field over the axon. That question is particularly important and challenging because of the highly complex fiber network architecture of both gels and tissues. In this study, we developed a computational method to explore the effect of macroscopic strain rates, spanning a relevant range of values, on the viscoelastic micromechanical environment of an embedded neuron in the gel (lower collagen concentration) and tissue (higher collagen concentration) models. Our results showed that changing the macroscopic-scale loading rate primarily affects the axon's predicted maximum strain in low-concentration collagen networks (gel representative models) while it has little to no effect on the maximum strain in high-concentration collagen networks such as occur in native facet capsular ligament. This behavior was seen in both isotropic and anisotropic networks, but with generally higher forces in the anisotropic cases.

Chapter 4: Estimating Cervical Facet Capsular Ligament Mechanics Based on Subject-Specific Anatomy and Kinematics [67]

To understand the facet capsular ligament's role in neck pain, the interactions between the facet capsular ligament and other spinal components must be examined. One approach is to develop a subject-specific finite element (FE) model of the cervical spine segment, simulating the motion segment and its components' behaviors under physiological loading conditions. This approach can be particularly attractive when a patient's anatomical

and kinematic data are available. In this study, we developed and demonstrated a method to create 3D subject-specific models of the lower cervical spine (C4-C7), with a focus on facet capsular ligament biomechanics. The facet capsular ligament geometries were generated based on the fact that the ligament encases the facet joints. As such, a surface was fitted to cover an estimated ligament-bone attachment regions on the joints' bony areas and the joint space. Displacement-controlled boundary conditions were applied to the bones such that vertebrae mimicked the kinematics extracted from biplane videoradiography of different head motions, including axial rotation, lateral bending, and flexion-extension. The fiber structure and material characteristics of the tissue were extracted from available human cervical facet capsular ligament data [27, 43, 44] and were incorporated in a hybrid multiscale model [68] to generate fiber characteristics that are subsequently used in FEBio to define tissue material. The method was demonstrated by application to the cervical geometry and kinematics of a healthy 23-year-old female subject. The strain maps within the facet capsular ligaments of the resulting subject-specific model was subsequently compared to models with generic geometry, kinematics and material model to assess the effect of model specificity on the facet capsular ligament biomechanics. Asymmetry in both the kinematics and the anatomy led to asymmetry in the calculated strain fields, highlighting the importance of patient-specific models. A sensitivity study revealed that the qualitative form of the strain field was largely independent of the estimated ligament-bone contact area, but the strain in non-contact regions tended to increase with greater estimated contact area. We also found that the calculated strain field was largely independent of constitutive model, but the stress field showed more constitutive-equation-dependence, as would be expected given the highly constrained motion.

CHAPTER 2

A Hybrid Microstructural-Continuum Multiscale Approach for Modeling Hyperelastic Fibrous Soft Tissue

You have to spend some energy and effort to see the beauty of math.

Maryam Mirzakhani

2.1 INTRODUCTION

Biological soft tissues are complex, hydrated composites, typically simplified as a mixture of fibrous proteins (primarily collagen and elastin) and cells [69, 70]. The multi-constituent nature of tissues and the dependence on crimped collagen fibers to add structural reinforcement makes tissue mechanical behavior inherently nonlinear. The heterogeneous distribution of constituents due to the varied mechanical loading environments, and the various microstructural requirements of cell populations also tend to make tissues anisotropic (Figure 2.1). The behavior of these tissues, including dissonant behavior from tissue to tissue (e.g. auxetic behaviors in tendon/ligaments [71, 72] compared to the relative rubber-like behavior of arteries [73–77]), makes defining a consistent constitutive model challenging.

Despite the complexity of tissue micro-structure, a number of models have been proposed in the continuum framework to define the nonlinear, anisotropic material behavior. By far the most common method for defining the non-linearity of soft tissues is by treating the material as having stress developed as an exponential of strain [50, 78–82]. Perhaps the most significant, and widely used constitutive model for nonlinear, anisotropic materials is the Holzapfel-Gasser-Ogden (HGO) model [50, 65]. The beauty of this model is in its simplicity, its broad applicability [83–94], and its adaptability and ability to be extended [86, 95–100]. In its most basic form, the model is described by a strain energy density function of a neo-Hookean ground substrate with an exponential anisotropic fiber component. The HGO model is given by:

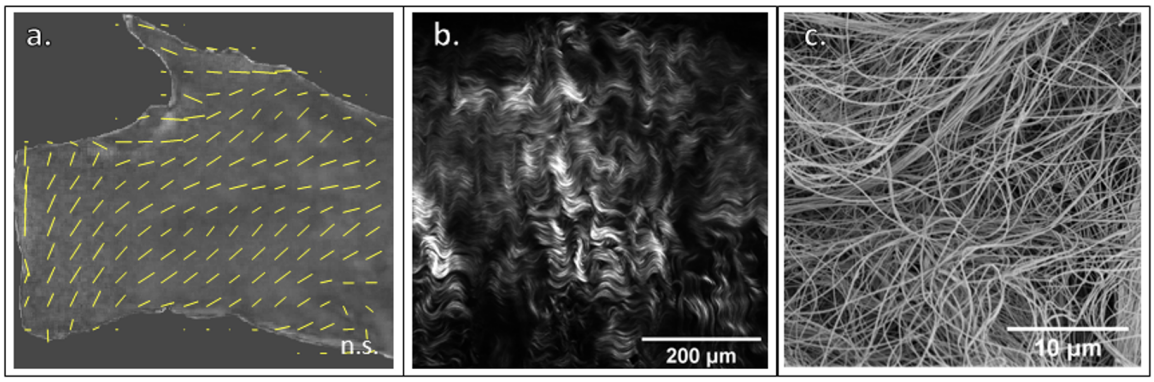

Figure 2.1: a. Quantitative Polarized Light Imaging (QPLI) of the brachiocephalic artery bifurcation showing macro-scale fiber orientation vectors. b. Second Harmonic Generation (SHG) imaging of collagen microstructure in the Facet Capsular Ligament (FCL). c. Scanning Electron Microscopy (SEM) of the collagen microstructure in the FCL

$$W = W^m + W^f = C_1 (I_1 - 3) + \frac{C_2}{(2C_3)} \left[\exp\left(C_3 (I_4 - 1)^2\right) - 1\right] \tag{2.1}$$

where W^m is the non-fibrillar matrix strain energy density, W^f is the fiber strain energy density, C_1 is the neo-Hookean material parameter, $I_1 = C_{II}$ is the first strain invariant of the right Cauchy-Green tensor (C_{IJ}), C_2 is the fiber modulus term, C_3 is the fiber nonlinearity, and $I_4 = a^0_I C_{IJ} a^0_J$ is the fourth strain invariant of the right Cauchy-Green tensor C_{IJ} and $\mathbf{a^0}$ is a vector describing the fiber direction.

A critical simplification in the analysis of such tissue behavior is the assumption that the deformation of the underlying fiber network is affine [101]. This assumption has been used countless times to lead to different soft tissue models based on invariants and/or the complete fiber distribution. However, the detailed microstructural behavior of a tissue is not, in general, affine [102, 103]. This fact leads to the use of multiscale models where one can precisely define the microstructure while still leveraging the advantages of finite-element modeling [37, 42, 104–114]. Of course, the necessity of solving many microstructural problems in the pursuit of modeling the deformation of a specific tissue leads to a huge computational cost. This computational cost is especially exacerbated when one adds in

multi-physics such as tissue failure, fluid dynamics, or microstructural remodeling [88, 90, 91, 115–127]. Thus, the ideal scenario would be to use the microstructural models when we need the structural and mechanical detail, but use a constitutive model (like the HGO) with a finite element solver when we need to run large-scale, multi-physics models.

In this work, we propose a hybrid modeling approach in which we fit an HGO model to deformations imposed on a microstructural element, then use the HGO constitutive model to enhance the speed of the finite element simulation. This technique allows one to examine microstructural features when necessary without generating and solving all the microstructural problems during the finite element solution. In this way, we enhance the flexibility in multiscale modeling by allowing for the use of larger domains with heterogeneous material definitions and complex boundary conditions without the need to run computationally expensive fully coupled multiscale simulations via a supercomputer.

2.2 METHOD

2.2.1 Mechanics Mathematical Preliminaries

Kinematic quantities important in the following analysis are given here. The first important descriptor is the deformation gradient, $\boldsymbol{F}$, which maps the deformation from the undeformed domain to the deformed domain. Out of the deformation gradient comes the Jacobian, $\boldsymbol{J}$ which is given as the determinant of $\boldsymbol{F}$, and represents the volume change due to the deformation. Additional important kinematic variables are the right Cauchy-Green tensor C, defined by $C_{IJ} = F_{kI}F_{kJ}$, and the Green-Lagrange strain tensor E, defined by $E_{IJ} = \frac{1}{2}(C_{IJ} - \delta_{IJ})$ where δ_{IJ} is the Kronecker delta. In this work, we also use several strain invariants. The isotropic first strain invariant, $I_1 = C_{II}$, and the transverse isotropic fourth strain invariant, $I_4 = a_I^0 C_{IJ} a_J^0$, dictated by a direction vector, $\boldsymbol{a^0}$. We further define the fourth strain invariant as the square of the averaged fiber stretch $\langle I_4 \rangle = H_{IJ}C_{IJ} = \hat{\lambda}_f^2$,

where H_{IJ} is the generalized structure tensor (defined below) and $\hat{\lambda}_f$ is the averaged fiber stretch. A number of mechanics quantities are also addressed in the following analysis. The first is the concept of stress. The Cauchy stress carries the physical interpretation of force per current cross-sectional area and is defined as $\boldsymbol{\sigma} = \frac{2}{J}\boldsymbol{F}\frac{\partial W}{\partial \boldsymbol{C}}\boldsymbol{F}^T$ where W is the strain energy density function for the material. The second Piola-Kirchoff stress is defined as $\boldsymbol{S} = \frac{\partial W}{\partial \boldsymbol{E}} = J\boldsymbol{F}^{-T}\boldsymbol{\sigma}\boldsymbol{F}^{-1}$, which carries no meaningful physical interpretation, but does represent a useful quantity for purposes of calculation due to both force and area being mapped to the reference configuration.

2.2.2 Methodological Principles

Our goal is to convert a discrete fiber network model, which allows a high degree of structural fidelity but is computationally intensive, into an HGO model, which is computationally much more tractable. Because our goal is computational simplicity, we use the simple form of the HGO model shown above in Eq. 2.1. It is routinely assumed in affine models of this type that the constitutive equation can be written in terms of independent contributions from a non-fibrous matrix and the fiber network. The non-fibrous matrix is often incompressible or includes a volume-dependent term to limit material compressibility. Similarly, in multiscale models [42, 108, 109], a separate neo-Hookean matrix is introduced in parallel to the network. For the present analysis, it is therefore assumed that the fiber network contribution is distinct from the neo-Hookean, incompressible non-fibrillar matrix, and the current work focuses on the fiber network contribution only. The fundamental challenge to be addressed is to convert a fiber network model into one based on the fiber stretch via I_4 (i.e. $a_I^0 C_{IJ} a_J^0$ in a model of the classical HGO form). That is, the problem is to determine parameters C_2 and C_3 such that the model

$$W^f = \frac{C_2}{2C_3}[\exp C_3(\langle I_4\rangle - 1)^2 - 1] \tag{2.2}$$

yields a fiber-network strain energy density function W^f that matches the results from the network computations. Here we delineate the difference between the square stretch, I_4, in a given direction $\boldsymbol{a^0}$, and the square stretch in the average fiber direction $\langle I_4 \rangle = H_{IJ}C_{IJ}$. The invariant $\langle I_4 \rangle$ is calculated as the double contraction of a generalized structure tensor H_{IJ} with the right Cauchy-Green tensor C_{IJ}. The generalized structure tensor H_{IJ} is defined as

$$H_{IJ} = \frac{1}{V}\int_{\Omega} N_I^m N_J^m dV = \frac{\sum_{m=1}^{k} V^m N_I^m N_J^m}{\sum_{m=1}^{k} V^m} \tag{2.3}$$

where $\boldsymbol{N}^m$ is the unit vector in the direction of fiber m, and $V^m = \pi \left(R^m\right)^2 L^m$ is the volume of a fiber with radius, R^m and length, L^m. The calculation of the generalized structure tensor and its use to calculate $\langle I_4 \rangle$ are based on the underlying assumption that, in general, the network behaves affinely. This calculation does not account for different properties of fibers such as the tension-compression asymmetry of fiber response, or the different fiber types that might occur (e.g., collagen and elastin). There are also differences incurred because the fibers are exponential and the deformation in a network is not affine, meaning the apparent modulus of any given fiber need not be the same as any other or, in fact, the average fiber. There are several ways one could approach this problem, including calculating the end-state $h_{ij} = F_{iK}H_{KL}F_{jL}$ for the network and mapping it back to the undeformed domain with or without those fibers that are in compression. This strategy, however, would rely on an accurate representation of the deformation, which is often unknown a priori. A second option would be to not calculate the structure tensor from the fiber network, but instead treat its components as additional fitting parameters. Doing so, however, would leave the underlying structural information we have from the microstructural networks unutilized.

One of the challenges with a structure-tensor-based model is the so-called tension-compression switch. Fibers are very stiff in tension but buckle and support almost no load

in compression. If the structure tensor and the resulting calculated $\langle I_4 \rangle$ do not exclude fibers in compression, then the model is at risk of overpredicting the stress response, especially if the model has been fitted to data from a different strain field. This issue has received much discussion (e.g., [96, 128]), and variations have been proposed in which compressed fibers are excluded [97, 100]. In the current work, we chose to use a simpler, all-fiber structure tensor. As noted earlier, the tension-compression switch is approximated smoothly in the discrete-fiber model by the exponential fiber constitutive equation; the specific representation of the switch has relatively little effect on the overall network mechanics [102]. We refer the reader to the in-depth discussions on structure tensors and tension-compression asymmetry in biological tissues given in other works [100, 128, 129].

There are, of course, infinitely many possible deformations, but the fitting problem can be reduced conveniently by considering the fiber network strain energy W^f as a function of $\hat{\lambda}^f = \sqrt{\langle I_4 \rangle} = \sqrt{H_{IJ}C_{IJ}}$, which represents an averaged fiber stretch in the affine, continuous model. Although the product $H_{IJ}C_{IJ}$ does not have any physical meaning within the context of the non-affine discrete fiber model, it is easily calculated and convenient for use in the fitting process. Likewise, W^f can be calculated either from computing an average stress in the domain [48] and integrating it with respect to its energy conjugate in the continuum sense to determine a strain energy, or by summing the total strain energy of all fibers and dividing by the domain volume. These two methods are given by

$$W^f = \int_{E_{IJ}=0}^{E_{IJ}} S_{IJ} dE_{IJ} = \frac{1}{V} \int_\Omega w^m dV \approx \frac{1}{V} \sum_{m=1}^{k} w^m V^m \tag{2.4}$$

where W^f is the total strain energy density of the fiber network, S_{IJ} is the second Piola-Kirchhoff stress, E_{IJ} is the Green strain, w^m is the strain energy density of fiber m, V is the domain volume, and V^m is the volume of fiber m. The individual strain energy of a fiber is given by

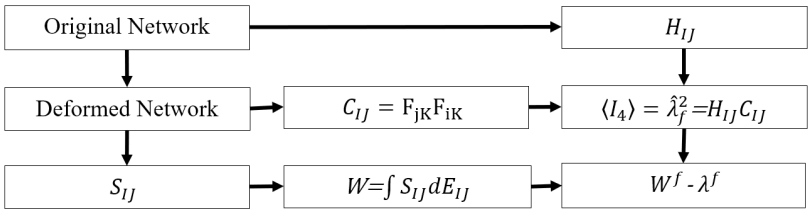

Figure 2.2: Flowchart for converting fiber network model to affine model.

$$w^m = \int_{E_{IJ}^m=0}^{E_{IJ}^m} S_{IJ}^m dE_{IJ}^m \tag{2.5}$$

The results from a network simulation of any macroscopic deformation can then be represented as W^f vs. λ^f. This method is further summarized in the flowchart in Figure 2.2. With W^f vs. λ^f from the network determined, the total-fiber constitutive law can be fit to the aggregated network-scale simulation results. Although in principle any total-fiber constitutive law could be used, a continuum model in an exponential format that is similar to the fiber's qualitative behavior is an intuitive choice to predict fibers' overall behavior. Therefore, throughout this work we use the expression of Eq. 2.2 and fit C_2 and C_3 to the W^f vs. λ^f curve.

2.2.3 Case Study: Multiple Deformations of a Single Network

To verify the ability of an HGO-type model to reproduce network mechanical response, a moderately aligned ($H_{11} = 0.69,\ H_{22} = 0.21$ and $H_{33} = 0.10$) 3D Delaunay network was generated using the Delaunay triangulation function, *delaunay*, in MATLAB (R2019a, MathWorks, Natick, MA). This alignment was chosen due to the tendency of collagenous tissues to possess a preferred alignment, observed in, for example, ligaments [11, 130]. Briefly, randomly generated seed points in the 3D space were used to generate a Delaunay tetrahedral network. The seed points represent network nodes, and the edges of the tetrahedral regions represent the fibers. After initial generation, the network was subjected to

artificial stretches to reach the desired alignment. Finally, the aligned network was clipped from the stretched network to a unit cube, and the fibers and nodes inside the cube were extracted to form the aligned networks used in these simulations. This process was done iteratively, with the number of the seed points adjusted in order to obtain a final volume fraction of 0.04 for each network, holding the fiber cross-sectional areas constant. This fiber fraction represents a collagenous tissue as in [131, 132]. The fiber volume fraction in a network is given by

$$\phi^f = \frac{V^f}{V} = \frac{\chi \sum_{m=1}^{k} \pi \left(R^m\right)^2 L^{*m}}{\chi^3 V^*} \tag{2.6}$$

where ϕ^f is the fiber volume fraction, V^f is the total fiber volume, V is the network volume, χ is a scale factor converting from computational length units to real length unit $[m]$, R^m is the radius of fiber m, L^{*m} is the length of fiber m in computational space, and V^* is the network volume in computational space.

The fibers in these networks were then modeled as one-dimensional nonlinear springs connected at freely-rotating pin joints (nodes) at two ends. The slender fibers are subjected to moderate to large strains and have negligible bending stiffness. The governing equation describing the fibers in the network was adapted from [133] and is defined as

$$f = \frac{kA}{B} \left(\exp\left[BE\right] - 1\right) \tag{2.7}$$

where f is the force generated within the fiber, A is the fiber undeformed cross-sectional area, k and B are constant and represent fiber stiffness and nonlinearity, respectively, and $E = \frac{1}{2}\left(\lambda_m^2 - 1\right)$ is the Green strain of the fiber, m, stretched to stretch ratio λ_m. The values for k and B in Eq. 2.7 and the fiber radius were set to 10 MPa, 2.5, and 100nm, respectively, following Dhume et al. [131]. We emphasize that the function in Eq. 2.7 represents a single fiber in the network, where the function itself is chosen so that the force is zero at zero strain, with large magnitude forces developed in tension and low magnitude forces

developed in compression, simulating the tension-compression switch seen in native collagen fibers. The solution of the network state given a prescribed deformation was calculated using Newton iteration to balance all forces on internal nodes. The overall Cauchy stress state for the network was then calculated as

$$\sigma_{ij} = \frac{1}{V}\int_{\Omega}\sigma_{ij}dV \approx \frac{1}{V}\sum_{m=1}^{k}\sigma_{ij}^{m}V^{m} = \frac{1}{V}\sum_{m=1}^{k}\left(\frac{f_i^m}{A^m}\right)n_j^m\left(A^m l^m\right) = \frac{1}{V}\sum_{m=1}^{k}f_i^m n_j^m l^m \tag{2.8}$$

where σ_{ij} is the network volume averaged Cauchy stress, V is the network volume, σ_{ij}^m is the Cauchy stress of fiber m, V^m is the volume of fiber m, f_i^m is the force from fiber m, A^m is the instantaneous cross-sectional area of fiber m, $\boldsymbol{n}^m$ is the fiber normal direction in the deformed state, and l^m is the current length of fiber m.

The network was subjected to five different deformations: x-direction uniaxial stretch, simple shear on the xy- and yz-faces, and equibiaxial stretch in the xy- and xz-plane (Figure 2.3a, b). The network underwent a stretch of 1.8 in the x-direction. The stretches for other deformations were calculated such that the final $\hat{\lambda}_f = \sqrt{H_{IJ}C_{IJ}}$ in all deformations was equal to the calculated $\hat{\lambda}_f$ for the x-direction uniaxial stretch experiment. These deformations were selected because the network of interest has $H_{11} > 0.33$, meaning that the main fiber direction falls mostly in the x-direction. This approach ensures $H_{IJ}C_{IJ} > 1$, which allows for proper fitting of the W^f curves. In this work, the directionality of the networks drove the deformations used for the initial HGO fits (i.e. networks aligned in x are subjected to x, xy, and/or xz deformations). For each deformation, the boundary nodes were displaced, and internal node equilibrium was attained using Newton iteration. In all deformations, the boundaries were displaced such that incompressibility was guaranteed on the network's bounding box. For each deformation, the (macroscopic) right Cauchy-Green tensor, C_{ij}, and the macroscopic volume-averaged Cauchy stress, σ_{ij}, were calculated and stress converted to W^f vs. λ^f as described previously (Eq. 2.4). The W^f vs. λ^f curves

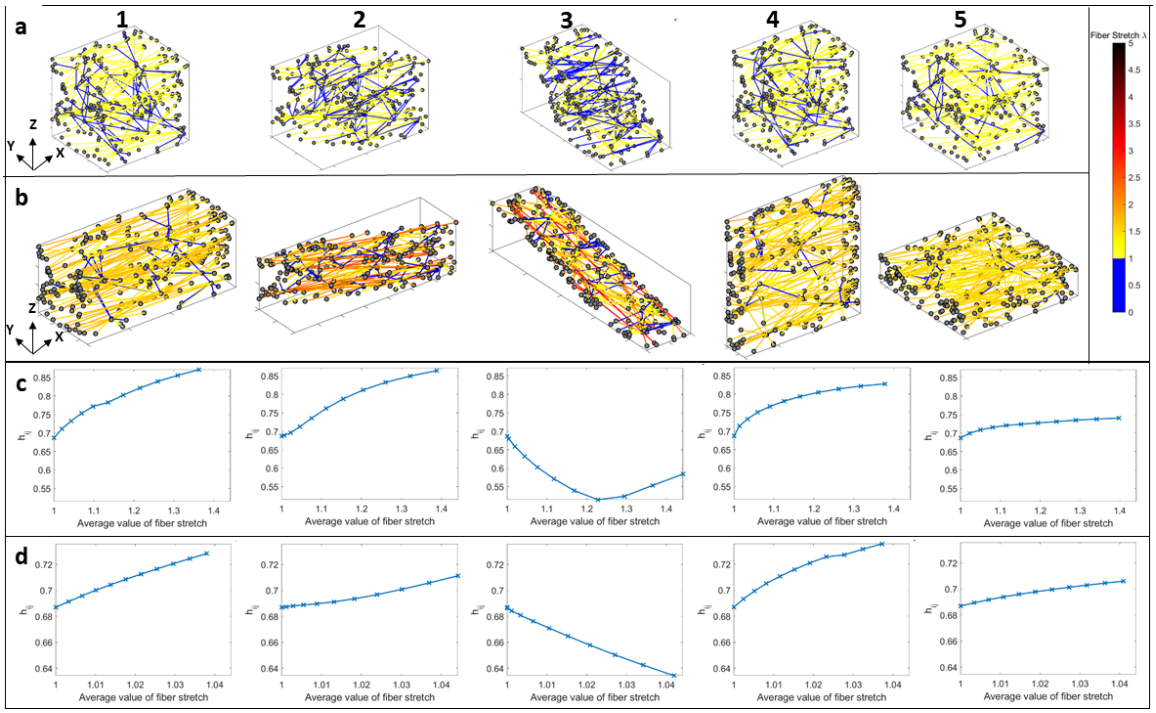

Figure 2.3: **a1-5**. Network deformations for x-uniaxial, xy-shear, yz-shear, xz-biaxial, xy-biaxial for 112% fiber Green strain. **b1-5**. Network deformations for x-uniaxial, xy-shear, yz-shear, xz-biaxial, xy-biaxial for 10% fiber Green strain. **c1-5**. The largest eigenvalue of the instantaneous orientation tensor, h_{ij} versus the average value of fiber stretch for 112% fiber Green strain. **d1-5**. The largest eigenvalue of the instantaneous orientation tensor, h_{ij} versus the average value of fiber stretch for 10% Green strain.

were plotted simultaneously for all the generated deformations, and a single constitutive HGO fiber model given in Eq. 2.2 was fit to the data using MATLAB (R2019a, MathWorks, Natick, MA) built in constrained minimization routine `fmincon`. An example of the W^f vs. λ^f curves and the fit are shown in Figure 2.5.

To show that how fiber realignment can differ in various deformations, the largest eigenvalue of the instantaneous orientation tensor at each steps, h_{ij}, was calculated and plotted vs. the average value of fiber stretch (Figure 2.3c, d).

2.2.4 Alignment Dependence for Delaunay Networks

We evaluated the proposed method by generating HGO model parameters for 750 Delaunay networks with a range of alignments. The various deformations described in Figure 2.3 were imposed on the networks, and W^f vs. λ^f plots were constructed for each deformation. For each network, the W^f vs. λ^f deformation plots were fit together with the single HGO model given in Eq. 2.2. Contour plots of the material parameters were then created to evaluate the material property variation with alignment and assess if the HGO model could be broadly applied across Delaunay networks of varying alignment.

2.2.5 Hybrid Microstructural-Continuum Multiscale Approach

The novelty of this approach is that it removes much of the computational overhead needed in fully coupled multiscale approaches. Particularly, the use of the network model to fit a continuous material model (HGO) lets us leverage the increased speed in calculating both stress and the material (or spatial) elasticity tensor of the continuum material model over the micro-network model. Take, for example, a network consisting of Q fibers and R nodes where we have Cauchy stress given by Eq. 2.8 converted to the PK2 stress to calculate the

material elasticity tensor

$$C_{IJMN} = \frac{\partial S_{IJ}}{\partial C_{MN}} = \frac{\partial}{\partial C_{MN}} \left[\frac{1}{V_0} F^{-1}_{Im} \left(\sum_{k=1}^{Q} f^k_m l^k n^k_n \right) F^{-1}_{Jn} \right] \tag{2.9}$$

where S_{IJ} is the network PK2 stress, and C_{MN} is the right Cauchy-Green tensor, V_0 is the undeformed network volume, $\boldsymbol{F^{-1}}$ is the inverse deformation gradient tensor, $\boldsymbol{f^k}$ is the fiber force vector, $\boldsymbol{n^k}$ is the fiber direction vector, and l^f is the fiber current length. If we examine these equations, it becomes clear that, at a minimum, we would need to calculate the fiber force, $\boldsymbol{f}$ for each fiber, k, and we would need to calculate something akin to the fiber elasticity, $\frac{\partial}{\partial C_{MN}} \left(\sum_{k=1}^{N} f^k_m l^k_n \right)$ for each fiber, k. For each network at each Gauss point in each element (i.e. 8 networks per hex element), we would have to calculate both of these quantities. That means we would have to run one network simulation per Gauss point and make Q calculations for the stress and Q calculations for the elasticity per network, if there existed an analytical solution to the elasticity tensor, which, in the case of non-affine networks, is not necessarily the case. Additionally, the network solution relies on determining the static force balance of internal nodes, which, if solved explicitly, would yield another R calculations. However, this solution typically involves implicit solution via Newton iteration, resulting in between 5-10 iterations to achieve static equilibrium for a well-conditioned network. Thus, in the best case scenario, we would have $2Q + R$ calculations per Gauss point. If we contrast this with the HGO model, which involves one stress calculation and one elasticity calculation per Gauss point, we expect a minimum decrease in computational cost of $Q + \frac{1}{2}R$ per network. The overall computation time is presented in Table 1.

One can fit the behavior of a network by subjecting it to many potential deformations and fitting the total data (as in Case Study 2.3), or one could simply fit one single deformation of interest. The former will give a better rough estimate if the actual deformation

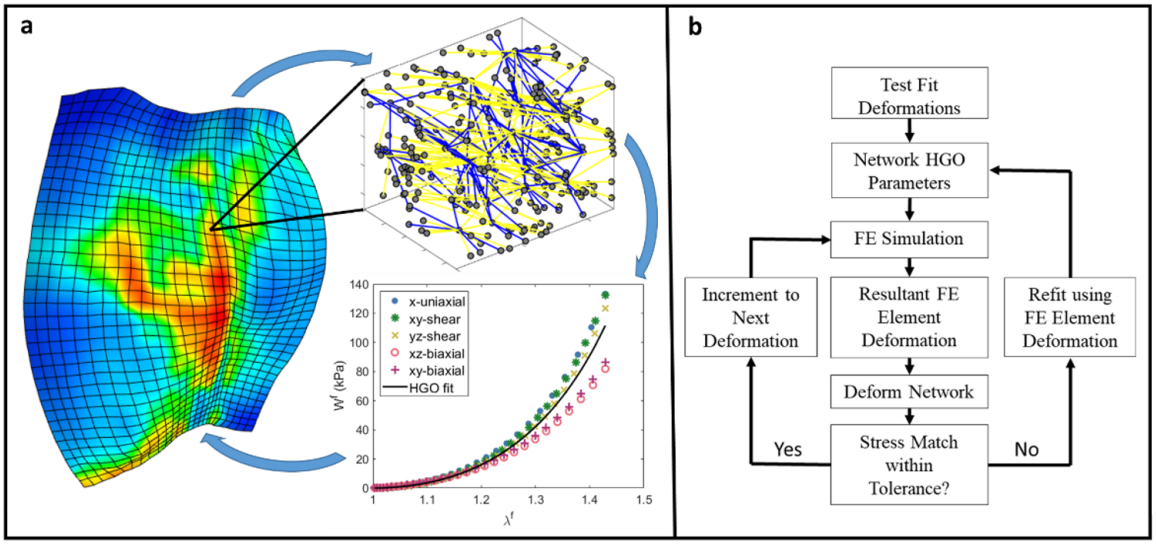

Figure 2.4: **a**. Schematic of the hybrid continuum-discrete multiscale approach. **b**. Flowchart for the hybrid continuum-discrete multiscale approach.

of the material is unknown, while the latter will be more accurate if there is confidence in the magnitude and type of deformation the network will undergo. We henceforth refer to the initial average fit to many deformations as the **HGO fit** and to the later fit to a single deformation as the **refit**. Care must be taken when refitting to a single deformation, as not all deformations will cause the average stretch to be greater than one. In these cases, the fit will not capture the behavior of the network, and an alternative fit should be used. In our model, we use two methods for dealing with this issue: 1. If the average stretch never exceeds one, we simply make the fiber modulus zero, thereby removing the fiber contribution, and 2. If the average stretch does eventually exceed one, but the fit is poor due to the behavior of the strain energy curve (i.e., Figure 2.4), we attempt to fit only the slope of the strain energy curve for which the average stretch is greater than one. This effectively allows us to fit something closer to the stress, as the stress is directly related to the slope of the W^f vs. λ^f curve.

Once the HGO properties are fitted to the network simulations, we can use those material inputs in a finite element (FE) framework as shown in Figure 2.4a. This allows us to

rely on the constitutive relation to solve the FE simulation rather than having to use costly microscale network simulations. Further, once we have the solution from the FE simulation, we can extract the deformation gradient at any point of interest and run the networks to evaluate any microstructural quantities such as fiber orientation or fiber stresses. This offers us the ability to evaluate discrete quantities in regions of interest, or to pass strains down to the microstructure to evaluate fiber remodeling or failure.

In an FE simulation, one often is concerned with an imposed deformation that occurs in a series of small steps. In this case, one can choose whether to iterate at a given step until the deformation field and model are consistent, or to adjust the model based on a given step and use the updated parameters for *the next step*. The latter approach introduces some error in that the continuum model does not match the microscopic model at the end of the step, but it has the considerable efficiency advantage of allowing an update at relatively low computational cost. The lagging update errors can also be further mitigated by imposing smaller deformation steps where in the limit of an infinitesimally small step the error becomes zero. If one only cared about the end state of the deformation, then this method would introduce little error, especially if the state or states of interest are iterated to match microscopic and macroscopic stress. For this work, we chose the less costly approach of allowing the continuum model correction to proceed with the previous step update, and only iterate the state of interest, which in our example (2.7) is the final step. This process is shown in Figure 2.4b.

2.2.6 Case Study: Single-Network Model Performance for Non-Fitted Deformation

In this study, we compared the fit of the HGO model to an array of deformations and the fit of an HGO model to a specific deformation. To do this, we first fit the network to x-uniaxial (magnitude 1.25), xy-biaxial, xz-biaxial (magnitude 1.1), xy- shear and xz-shear (magnitude 0.15). Once the HGO model had been fit, we tested it on a deformation that

differed from the ones used in fitting the model parameters. Specifically, we modeled an element from complex motion of the stretching and three-point bending of a facet capsular ligament as in [134]. We imposed the deformation gradient of an element experiencing maximum stretch during the simulated experiment:

$$\boldsymbol{F} = \begin{bmatrix} 1.239 & 0 & 0.0035 \\ 0 & 1.048 & -0.0014 \\ -0.0080 & 0.102 & 0.770 \end{bmatrix} \tag{2.10}$$

which was dissimilar to the uniaxial, biaxial, and shear deformations used to fit the initial HGO model. The deformation was imposed on the discrete network model, and the volume-averaged Cauchy stress was determined. Concurrently, the Cauchy stress was calculated by the HGO model using the parameters fitted to the suite of deformations (given above as **HGO fit**). In addition, in keeping with the **refit** update strategy discussed above, after the simulation was done, we refit the HGO model to W^f vs. λ^f giving us stress estimates for the deformation imposed in Eq. 2.10.

2.2.7 Comparison between Network-to-HGO Model and Full Multiscale Model

The goal of the proposed method is to facilitate higher-efficiency multiscale simulations based on network structure. To evaluate its potential, we performed a full multiscale simulation of a representative L4-L5 facet capsular ligament (FCL) sample during spinal flexion (reproducing the model of Zarei et al. [49]). The model boundary conditions are defined through application of nodal displacements based on the bone surface from the kinematic simulation of Bermel et al. [10]. Additional details of the simulation setup are available in [49]. The same micro-networks used in [49] were applied in the network-to-continuum scheme, and the resulting continuum biomechanics problem was solved using the open-source finite-element platform FEBio [135]. Because FEBio does not support the HGO

model, the ligament was modeled as a coupled solid mixture of a Mooney-Rivlin (effectively reduced to a neo-Hookean) ground matrix with three fiber families, leading to the strain energy density function

$$W = W^m + W^f \tag{2.11}$$

where W is the total strain energy density. The first term in the total strain energy density is the non-fibrillar matrix component of the strain energy density W^m given by

$$W^m = C_1 \left(I_1 - 3\right) - 2C_1 \ln J + \frac{\lambda}{2}(\ln J)^2 \tag{2.12}$$

where C_1 is half the second Lamé parameter relating to the neo-Hookean material parameter, I_1 is the first strain invariant of the right Cauchy-Green tensor, C_{IJ}, $J = \det(\boldsymbol{F})$ is the differential volume change of the deformation, and λ is the first Lamé parameter relating to the bulk modulus. The tissue was considered as a compressible material with a matrix modulus and bulk modulus that matched those used by Zarei et al. [49]. The compressibility of the FCL was experimentally observed by Little et al., who suggest that the Poisson's ratio is as low as 0.3 [11]. The second half of the strain energy density is the fiber component of the strain energy density W^f given by

$$W^f = C_2/(2C_3) \sum_{p=1}^{3} h^p \left(\exp\left(C_3(I_4^p - 1)^2\right) - 1\right) \tag{2.13}$$

where C_2 represents the fiber modulus, C_3 captures fiber nonlinearity, h^p is the weighting factor for fiber family p, $I_4^p = C_{IJ}N_I^p N_J^p = (\lambda^p)^2$ is the fourth strain invariant of the right Cauchy-Green tensor, C_{IJ}, $\boldsymbol{N}^p$ is the unit vector pointing in the direction of fiber family p in the undeformed state, and λ^p is the average fiber stretch of fiber family p. The undeformed direction vectors $\boldsymbol{N}^p$, were generated directly from the structure tensors H_{IJ} by taking the eigenvectors, which, since H_{IJ} is a symmetric positive definite matrix, give

three orthogonal fiber directions. For the current work, we use these three orthogonal fiber families pointing in the principal directions of H_{IJ} and assign the weight h^p to each family based on the eigenvalues of H_{IJ} corresponding to each eigenvector $\boldsymbol{N}^p$. Fiber material parameters C_2 and C_3 were fit to the W^f vs. λ^f plots using the method described above. The neo-Hookean material parameter, C_1, and the bulk modulus parameter, λ, were set to 0.025 MPa and 0.417 MPa, respectively, to match [49]. The analogous stress for this strain energy function can be found in the FEBio manual [136] under compressible materials Fiber with Exponential Power Law (4.1.3.8) and Coupled Mooney-Rivlin (4.1.3.17).

Briefly, to generate the finite-element simulation, we imported the L4-L5 FCL geometry mesh of hexahedral elements [49], and applied HGO parameters to each individual element corresponding to the microstructural networks applied in [49]. To simulate flexion, the displacement of the nodes at the entheses (left and right sides of Figure 2.4a) were specified based on the the L4-L5 motion segment model [10] as further described in [49].

Initially, micro-networks from the full multiscale model were fit to the HGO using multiple deformations, as described previously. A FEBio model of the representative FCL sample bending in flexion was then simulated using the initial HGO fit for fiber material parameters in Eq. 2.13. For added accuracy, the deformation gradient tensor for each element in the FEBio HGO model was then used to refit the fiber material parameters. For comparison, maximum shear stress and maximum shear strain fields were computed for the full multiscale model, the FEBio initial HGO model, and the FEBio refit HGO model.

2.3 Results

2.3.1 Multiple Deformations of a Single Network

A representative fiber network was chosen for detailed analysis. The network is shown after moderate (10% Green strain, Figure 2.3a) and extremely large (112% Green strain in Fig-

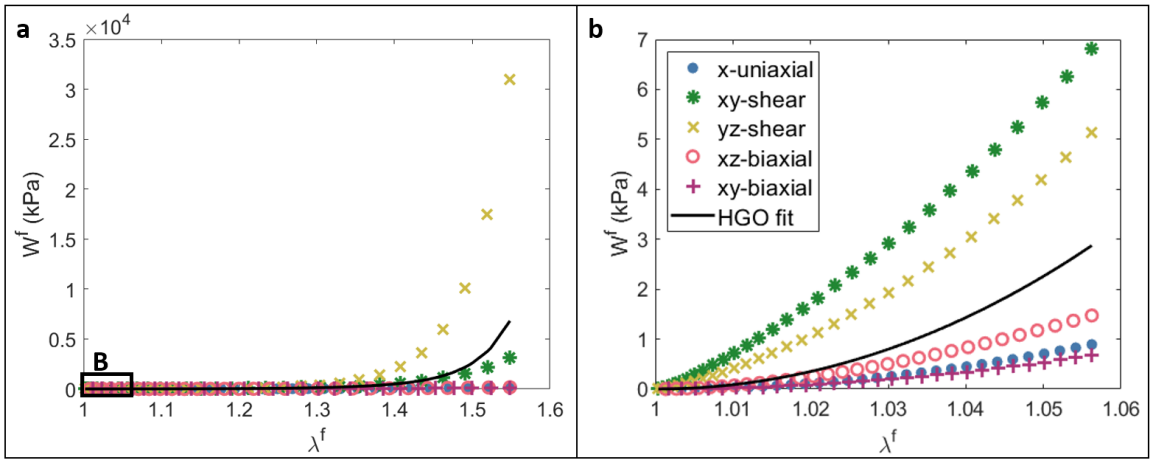

Figure 2.5: Holzapfel-Gasser-Ogden material property determination from microstructural networks under varied deformations for **a**. 112% Green strain, **b**. 10% Green strain

ure 2.3b) deformations. The deformed network is shown for x-uniaxial, xy- and xz-shear, and xy- and xz-biaxial deformations (Figure 2.3a and b). In this case, the network of interest has $H_{11} = 0.69$, meaning that the use of x-direction deformations ensures $H_{IJ}C_{IJ} > 1$ which allow us to more accurately fit the W^f curves.

The largest eigenvalue of the instantaneous orientation tensor, h_{ij}, is plotted versus the average value of fiber stretch over the full stretch range (Figure 2.3c) and in close-up of the small-stretch range (Figure 2.3d). The eigenvalues show large variation with deformations which is particularly pronounced at low strains. This result shows that the fiber realignment is highly deformation-dependent.

The fitting of network behavior to a series of different deformations is shown in Figure 2.5. We see that under relatively large strains, the W^f vs. λ^f curves become more similar. At small to moderate strains, the non-affinity of the deformation can play a significant role in the mechanics of the network, causing the plot of W^f vs. λ^f to become strongly deformation-dependent (Figure 2.5b). In the case of Figure 2.5, for example, a single HGO model cannot match the network model for all possible deformations, or even for specific families of deformations.

2.3.2 Alignment Dependence for Delaunay Networks

A total of 750 networks with different orientations ranging from isotropic ($H_{11} = 0.33$) to strongly aligned ($H_{11} = 0.8$) were studied, with the five representative networks (numbers 1-5) examined in detail in Figure 2.6. The network views in Figure 2.6a (xy-view) and Figure 2.6b (xz-view) show markedly different alignments. The orientations of these networks start with network 1 being nearly isotropic, network 2 being slightly aligned in the x-direction, network 3 being slightly aligned in the z-direction, network 4 being more strongly aligned in the x-direction, and network 5 being even more strongly aligned in the x-direction, as demonstrated by the numbering in Figure 2.6d-f. The W^f vs. λ^f curves were plotted for each network, and an HGO curve was fit to them (Figure 2.6c). It is evident from these W^f vs. λ^f plots that the fit of the HGO model becomes more variable for more highly aligned fiber networks, especially at large strains. Another particularly interesting aspect of these plots is the behavior of network 3. The W^f vs. λ^f plot would indicate that the direction transverse to the alignment direction is actually stiffer than that in the direction of alignment. However, this is not the whole story. The fiber stretch values are the double contraction of the orientation tensor and the right Cauchy-Green tensor, so when stretching in directions transverse to the primary alignment, much greater magnitudes of stretch are necessary to produce the same averaged fiber family stretch. In fact, the magnitude of the xy-biaxial stretch in network 3 was 3.33, while the magnitude of the xz-biaxial stretch was only 1.17. This effect is further evidence of the non-affine fiber realignment occurring in fiber networks that is not well captured by the HGO model. Figure 2.6c also shows that the deformations corresponding with alignment are similar to what was observed in Figure 2.5. For network 1, all deformations form a tight cluster of W^f vs. λ^f curves because the fibers are nearly isotropic. Network 2 shows slightly more spread since the primary orientation is more strongly aligned in the x-direction, and networks 4 and 5 exhibit even greater spread

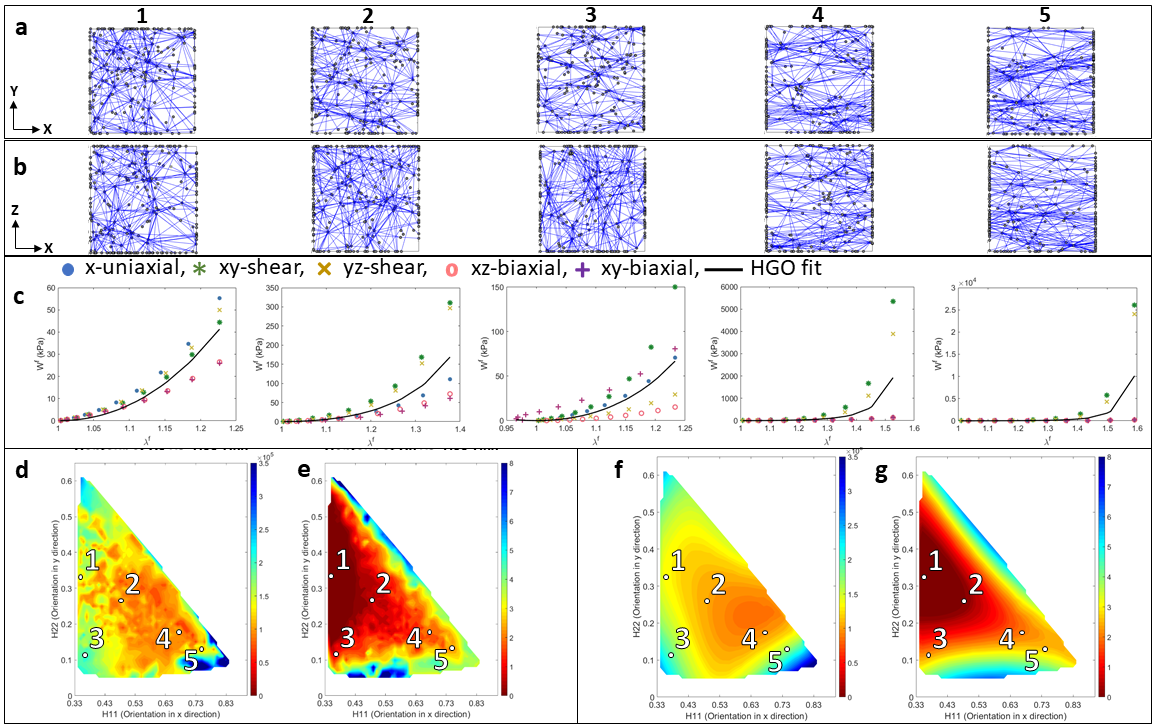

Figure 2.6: **a1-5**. xy view of networks 1-5. **b1-5** xz view of networks 1-5. **c1-5**. $W^f - \lambda^f$ of networks 1-5 with alignment, network 1: $H_{11} = 0.35$ and $H_{11} = 0.32$, network 2: $H_{11} = 0.5$ and $H_{11} = 0.32$, network 3: $H_{11} = 0.36$ and $H_{11} = 0.12$, network 4: $H_{11} = 0.66$ and $H_{11} = 0.18$, network 5: $H_{11} = 0.74$ and $H_{11} = 0.14$. **d** and **e**. Contour plots of HGO material property, C2 and C3, respectively, as a function of alignment in x, H_{11}, and y direction, H_{22}. **f** and **g**. Contour plots of fitted value of HGO material property, C2 and C3, respectively, to the multivariate nonlinear model of Eq. 2.14.

due to increased alignment in the primary x-direction.

Despite the differing W^f vs. λ^f behavior with different deformations, we still require an initial set of parameters for our simulations. We therefore fit a pair of model parameters C_2 and C_3 from Eq. 2.2 to the W^f vs. λ^f curves to allow us to readily determine material parameters without the need to run any additional simulations. We observed that the fitted parameters C_2 and C_3 were not constant over all networks, but showed considerable variation with network alignment. This result indicates that the degree of non-affinity, as indicated by the amount of correction necessary to convert the discrete fiber network model into an affine model, is dependent on fiber alignment. This result was previously obtained

by Hatami-Marbini and Picu [103], who found a greater degree of non-affinity in aligned networks loaded transverse to the preferred direction of alignment. The importance of this result lies in the fact that the constants C_2 and C_3 depend the fiber network orientation, *even for networks constructed of identical fibers and even when orientation is included in the continuum model via the construct* $H_{IJ}C_{IJ}$.

To further explore the observed dependence, contour graphs of the calculated parameters, C_2 and C_3, were generated as a function of the alignment in the 1 and 2 directions (H_{11} and H_{22}, respectively) for all networks simulated (Figure 2.6d and e). The location of networks of Figure 2.6a and b are indicated on the contours with numbers 1-5. The non-smooth appearance of the contour lines must derive from other factors that contribute to the network behavior. However, H_{11} and H_{22} are sufficient to capture the general trend via the quadratic curve fits shown in Figure 2.6f and g. The equations for those fits,

$$C_2 = \sum_{i=0}^{2}\sum_{j=0}^{2} \alpha_{ij} H_{11}^i H_{22}^j \ , \ C_3 = \sum_{i=0}^{2}\sum_{j=0}^{2} \beta_{ij} H_{11}^i H_{22}^j \tag{2.14}$$

allow estimation of C_2 and C_3 for any Delaunay network of fibers with the underlying properties specified above (Eq. 2.7). The goodness of fit was marginal ($R^2 = 0.47$ for C_2 and $R^2 = 0.73$ for C_3) due to the inherent differences between networks and other factors influencing behavior (i.e. even networks with the same alignment have varied nodal positions and fiber lengths, which can change the network response to stretch). The coefficient values are given in Table 2.1.

Large values of C_2 and the smallest values of C_3 occur when the network is close to isotropic (point 1 in Figure 2.6d and e). *If one desires to represent the behavior of an isotropic, non-affinely deforming discrete-fiber network with an affine-deformation model, the underlying fiber model in the network needs to be stiffer and less nonlinear compared to that representing a more strongly aligned network (point 5 in Figure 2.6d and e).*

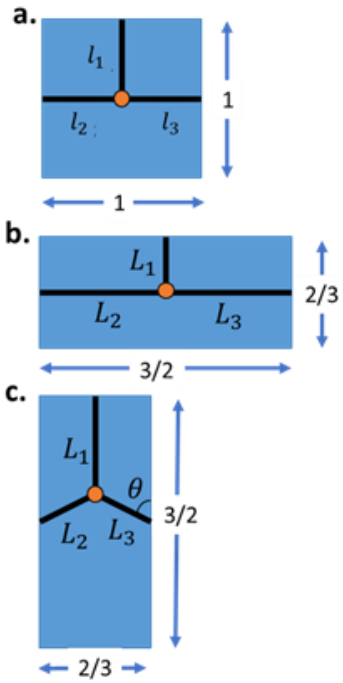

Figure 2.7: **a.** Undeformed network where $l_1 = l_2 = l_3 = l = 1/2$. **b.** Network stretched in the direction of strongest alignment where $L_2 = L_3 = 3/4$ and $L_1 = 1/3$. **c.** Network stretched transverse to the direction of strongest alignment where $L_2 = L_3$.

Table 2.1: Coefficients for the fit of HGO parameters C_2 and C_3.

ij	α_{ij} [MPa]	β_{ij} [-]
00	1.56 ± 0.22	-11.84 ± 4.46
01	-8.30 ± 1.89	94.49 ± 28.61
10	14.10 ± 3.77	70.46 ± 15.98
11	-5.56 ± 0.58	-517.60 ± 97.80
02	33.70 ± 7.63	-106.90 ± 29.40
20	-59.90 ± 16.27	-59.44 ± 13.25
12	5.47 ± 0.79	474.80 ± 69.40
21	-35.90 ± 7.57	396.00 ± 75.60
22	67.25 ± 17.50	0

As a simple verification, suppose we have the network shown in Figure 2.7a having $H_{IJ} = \begin{bmatrix} 2/3 & 0 \\ 0 & 1/3 \end{bmatrix}$. If we stretch in the direction of fibers as shown in Figure 2.7b where $F_{iJ} = \begin{bmatrix} 3/2 & 0 \\ 0 & 2/3 \end{bmatrix}$ and $C_{IJ} = \begin{bmatrix} 9/4 & 0 \\ 0 & 4/9 \end{bmatrix}$, we have an estimated average fiber stretch of $\langle \lambda_f \rangle = \sqrt{H_{IJ} C_{IJ}} = \sqrt{3/2 + 4/27} = 1.284$. If we simply compute the average stretch of the three fibers we have $\lambda_1 = 2/3$ and $\lambda_2 = \lambda_3 = 3/2$ which gives us a mean stretch of $\bar{\lambda} = 1.222$. Now if we take the same network and stretch transverse to the direction of alignment as shown in Figure 2.7c where $F_{iJ} = \begin{bmatrix} 2/3 & 0 \\ 0 & 3/2 \end{bmatrix}$ and $C_{IJ} = \begin{bmatrix} 4/9 & 0 \\ 0 & 9/4 \end{bmatrix}$, we get an estimated average stretch of $\lambda_f = \sqrt{8/27 + 3/4} = 1.023$. If we then compute the actual stretches by computing the equilibrium positions assuming that the fiber forces are linear in strain such that sum of vertical forces is zero:

$$\sum f_y = 0 = (L_1/l - 1) - 2(L_2/l - 1)\cos(\theta) \tag{2.15}$$

and enforcing the geometric constraints $L_2 \cos(\theta) + L_1 = 1.5/2$ and $2L_2 \sin(\theta) = 1/1.5$, we can solve giving $L_1 = 0.439$, $L_2 = 0.456$, and $\theta = 47.0^o$. Thus, the stretches are $\lambda_1 = 0.88$ and $\lambda_2 = \lambda_3 = 0.91$ giving an average stretch of $\bar{\lambda} = 0.900$. This example leads us to two observations: 1. The estimated stretch transverse to the direction of alignment is far from that in the direction of alignment, and 2. The estimated behavior of the stretch transverse to the direction of alignment is not representative of the true average, and is, in fact, indicating the network is in tension when the true behavior of the network shows all the fibers in compression. This simple example drives home the point that the networks estimated using the structure tensor, H_{IJ} can be quite different from the real network behavior when the network is loaded transverse to its preferred direction of alignment. In this case, the network itself is very non-affine and should require a larger correction which is

observed in Figure 2.6d-e. Further, this result demonstrates the issue one can encounter when trying to fit the network behavior to the HGO model where the network itself develops almost no stress (effectively zero since the fibers buckle in compression) despite the fact that the HGO model using the structure tensor and calculating $\langle I_4 \rangle$ indicates the fibers should be in tension. This results in a fitted HGO fiber stiffness of ≈ 0, which is clearly unphysical in general, but may be true for certain deformations. This effect is one that we must account for in our fitting method as discussed in Section 2.5 above.

2.3.3 Case Study: Single-Network Model Performance for Non-Fitted Deformation

A simple validation of the initial HGO fit and refit process is shown in Figure 2.8. The initial HGO fit of uniaxial, biaxial, and shear deformations produces stresses of a similar magnitude as the network simulation under the deformation given in Eq. 2.10 (Figure 2.8a). However, the results show large discrepancies in the shape of the curve (Figure 2.8a), which are largely corrected in the refit process (Figure 2.8b). The study presented indicates the viability of fitting an HGO model using the underlying orientation and a generated W^f vs. λ^f for many deformations to give a rough estimate of parameters, while highlighting importance of the refit process to producing the proper behavior. Further, this case study demonstrates how network mechanics vary significantly from the extrapolated HGO model under different deformations.

2.3.4 Comparison to Full Multiscale Simulations

Maximum shear stress and strain fields are shown for the multiscale model, initial HGO model, and refit HGO model (Figure 2.9). The maximum shear stress and strain distribution of the HGO model compared to the multiscale model are visually similar, and the HGO model was able to predict the regions of high shear stress and strain. The initial HGO model parameters underpredicted the magnitude of the maximum shear stress and overpredicted

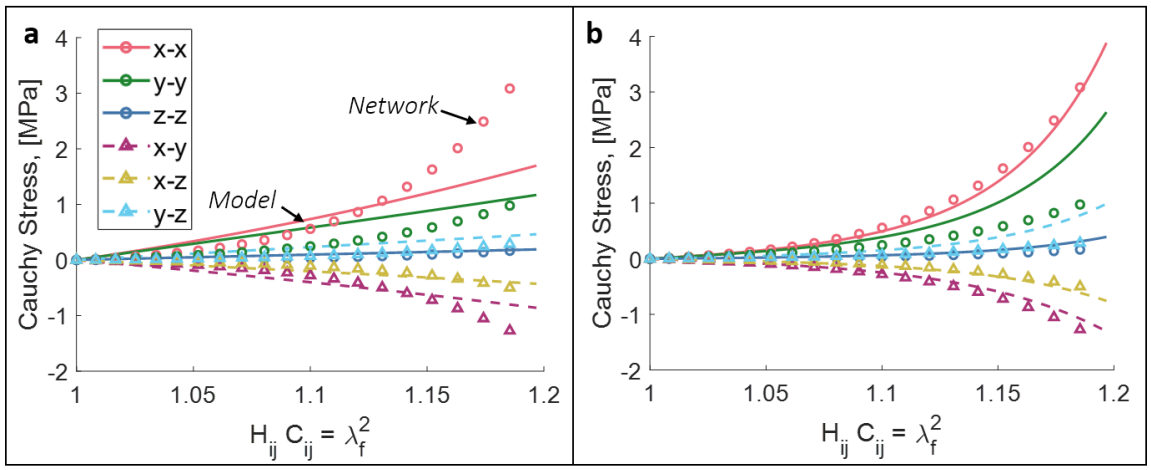

Figure 2.8: Comparison between HGO model and network simulation under complex deformation for a. initial fit and b. refit

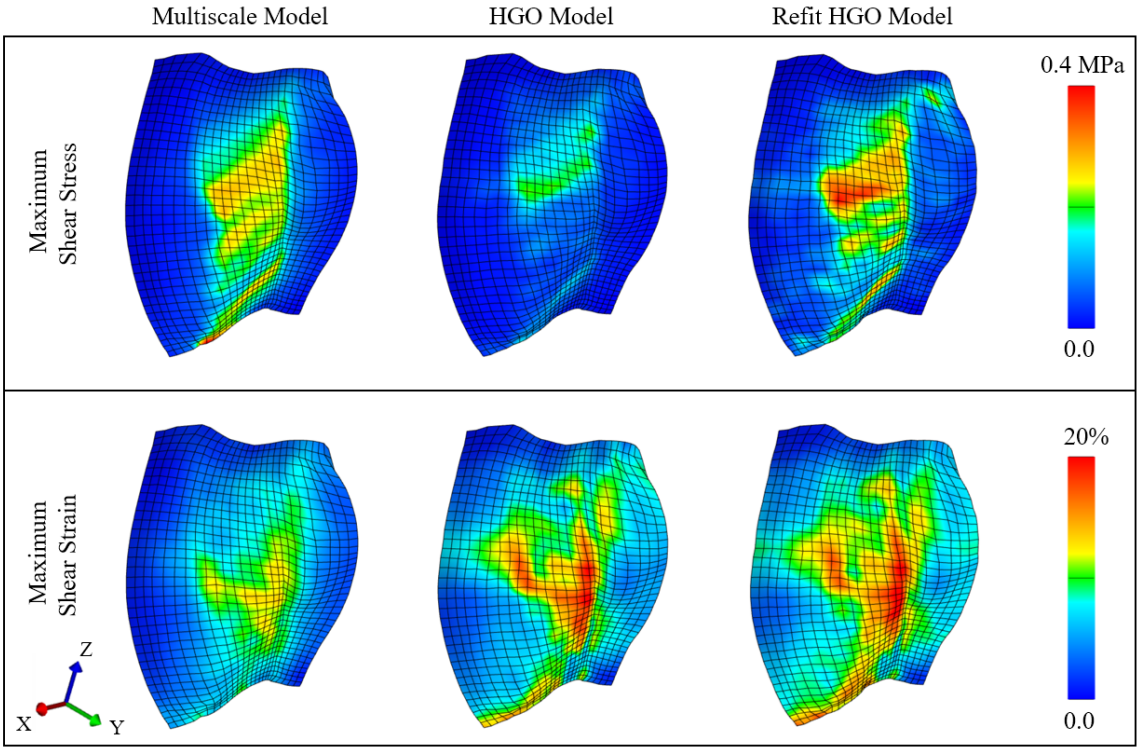

Figure 2.9: Maximum Shear Stresses and Strains of the multiscale, HGO, and refit HGO models for a single representative FCL sample during spinal flexion. The HGO model predicted the location of high shear stresses and strains while the refit HGO model improved the accuracy of magnitude of the maximum shear stress.

Table 2.2: Computation Time for Multiscale vs HGO FE model

	Multiscale	HGO
Task	Time [cpu-hour]	
Initial Simulation and Fit of 900 Networks (x 5 deformations x 20 steps)	NA	1.12
Re-simulation and Refit of 900 Networks (x 1 deformation x 20 steps)	NA	0.34
FE Simulation	2622.69	0.02
Total	2622.69	1.48

the max shear strains in these regions, but the accuracy of the tissue's stress prediction improved with a refit of the HGO parameters with each element's average deformation gradient tensor. The refit HGO model more accurately localized regions of high tissue shear stress, at the cost of a small increase in the tissue's strain, when compared to the initial HGO model. This observation is supported by the improvement of RMS error of the refit HGO model maximum shear stress compared to the initial HGO model. The RMS errors for the initial HGO model maximum shear stress and strain are 0.074 MPa, and 3.28%, respectively. The RMS errors for the refit HGO model maximum shear stress and strain are 0.062 MPa, and 4.12%, respectively. Further, the computation time for the entire HGO simulation including the final step refit is shown in Table 2.2. The time to run the HGO simulation is orders of magnitude decreased over the full multiscale simulation.

2.4 Discussion

2.4.1 Major Findings and Potential Significance

In this work, we developed a hybrid microstructural-continuum multiscale model to reproduce the macroscopic constitutive behavior of a structure-based multiscale simulation. This paper presents methods to speed up the model construction and full analysis of a discrete-fiber multiscale model while accounting for the microstructural details of a heterogeneous tissue such as FCL. The proposed work uses the structural parameters of discrete fiber net-

works in a continuous-fiber model such as HGO to decrease the computational cost of a full multiscale simulation of a heterogeneous tissue from 2622.69 to 1.48 CPU-hours as is shown in Table 2.

We found that the macroscopic-scale behavior of a Delaunay network can be reasonably described using the HGO model, but the accuracy of the approximation is dependent on the degree of alignment of the fiber network, the type of deformation imposed, and the magnitude of the deformation. The results of Figure 2.5 and Figure 2.6c indicate that simulations within a certain family of deformation types (uniaxial, biaxial, shear) can be fit with a high degree of confidence. The results of Figure 2.6c and Figure 2.8 suggest that extrapolating beyond the fitting range can give an overall rough estimate of behavior, but it is important to update the parameters based on the deformation. If the deformation of interest is known (e.g., one knows that the system will be loaded in equibiaxial extension), then one can simply fit a model to that deformation and use the model, but the deformation of interest is almost never known a priori. Even if the type of deformation or the boundary conditions are known, however, the magnitude of the deformation is often unknown, and tissue heterogeneity virtually assures that the local deformation is different from the applied (global) deformation, so it is essential to have a procedure that can be used to provide a good initial guess of the continuum model parameters one needs, as well as a method for updating the parameters. This work demonstrates reasonable methods for selection of initial parameters via fitting multiple deformations, and a refitting process based on the simulation deformation gradient.

In addition, we have described how stronger alignment of Delaunay networks results in more dissimilar behavior between deformations in terms of W^f vs. λ^f curves (Figure 2.6c). This result, while not unexpected based on previous studies [103], is significant because it further emphasizes the importance of the refit process and the challenges of trying to use an affine model to describe a material that exhibits non-affine behavior. The networks also

showed increased nonlinearity and fiber modulus with alignment, which further indicates that inherent non-affinity alters the apparent mechanical response of the tissue. We further offered a simple verification of this result in the example in Figure 2.7, which further demonstrates the pitfalls in assuming affine behavior in the modeling of fibrous tissues. Particularly, one must be cautious when one starts to probe local phenomena such as cell-ECM interactions or tissue failure in affine continuous models.

Taken together, these results indicate that the HGO model itself does not fully capture the change in network behavior with the generalized structure tensor, H_{IJ}. One issue with this structure tensor is that, to properly capture the behavior of a dispersed fiber population with a tension-compression switch, one needs to recalculate the tensor using only the tensile fibers. In an ideal case, this would be done for each deformation step (alternative approaches are not given here, but are discussed in [100, 128]). Such an approach could help alleviate some of these differences observed in the current study, but the cost of performing a spherical integration over 3D distributions of fibers might well prove greater than that of the simple refit process, especially for multiple fiber families or multiple fiber types. Some network models, might be better fit, to a certain extent, by a compressed-fiber-excluding macroscopic model, and a more thorough testing regimen achievable via computational vs. experimental tests may provide more insight into exactly what behaviors are captured or lost by such models. Future in-depth studies of on the translation of a discrete, fiber-level tension-compression switch to a macroscopic fiber compression exclusion model are merited.

As discussed above, we do not account for the fiber tension-compression asymmetry in the calculation of H_{IJ}. That is, H_{IJ} is calculated based on all fibers in the initial state. We instead capture the fiber tension-compression switch through the fiber constitutive law, which is much stiffer in tension than in compression. The tension-compression switch of fibers is intrinsic to the microstructural model, so we remove the requirement for fiber

exclusion from the structure tensor [71, 128]. The HGO parameters C_2 and C_3, which are fit to the results of the microstructural simulations, are thus informed by the tension-compression asymmetry inherent to the model. It may be possible that a better fit of the microstructural model could be obtained by an HGO model with a tension-compression switch, but that possibility was not explored in the current work.

We further described how a curve-fit of multiple simulations could allow one to select continuous model parameters to represent Delaunay networks with arbitrary orientation without rerunning simulations (Figure 2.6). The construction of such databases of properties for networks can further simplify the assessment of material parameters that describe network behavior. While the equations show a high degree of variance, construction of a broad curve-fit of parameter values can give us a reasonable starting point for a wide range of networks. The initial fitting of the network behavior to multiple deformations is the largest contribution to the overall time spent on simulation for the HGO FE model (Table 2). Thus, if one can select starting parameters based on network orientation and some other metric of network construction like network type (Delaunay, Voronoi, etc.), one can greatly reduce the time to produce simulations. In fact, this method of reproducing network parameters from pre-defined relations rather than having to generate and run the networks could have a significant impact on creation and simulation of multiscale tissue models, allowing for many hypotheses to be tested quickly with regards to fiber orientations, tissue composition, or localized defects. If such a strategy is to be pursued, however, it is imperative that the starting parameter values be based on networks similar to the ones being used in the simulation.

We describe the application of the microstructural-to-HGO modelling strategy to a finite-element simulation. This simulation shows similar results to a full multiscale simulation (Figure 2.9) while reducing the model construction and simulation time by orders of magnitude over a full multiscale approach (Table 2). As mentioned previously, this

approach, combined with estimation of material parameters without generating and simulating networks, could enable multiscale simulations without the need for a supercomputing cluster. Eliminating the necessity of bridging micro- to mm-scale could also open up opportunities to take tissue multiscale approaches up another scale level to organ or full-body kinematics, further helping us identify things like the role local FCL defects play in the spine or elucidating the role of microstructure in aneurysm mechanics.

2.4.2 Model Limitations

As with all models, the proposed system has several limitations. First, because the HGO model is an imperfect estimator of actual network behavior, there will be intrinsic errors even after the proposed refitting procedure. One could perform this analysis with other constitutive models that may capture specific behavior differently as compared to the HGO model (take for example the Blatz-Ko material for compressible materials like collagen gels [137], or any of a number of actively contracting models for vascular tissues such as [138–140]). The proposed technique is adaptable to different constitutive models, and could be fit to multiple affine models to select the best choice.

As noted above, the HGO model did not fully capture the observed network behavior. We observe that a strength of our approach is that the computational experiments are not limited by the physical realities of equipment design and sample damage, so one can perform any experiment desired and as many experiments as desired. As a result, any inability of the continuum-scale model to capture the micro-scale network model's behavior will be apparent. Whether this effect is a positive or negative feature depends on the perspective of the user: it virtually guarantees inconsistency between the micro- and macro-scale models in some deformation, but it enables the user to see exactly where and how severe such inconsistency is, which could be valuable. For example, one could decide that the inaccuracy is in a range of deformations that are not physiologically relevant, or the inconsistency

could inspire the development of new constitutive models at the continuum scale.

Another limitation of the approach in current form is the restriction to a single, non-evolving network. A major advantage of the full multiscale approach is the ability to accommodate changes in the network due to, e.g., failure [104, 122, 141] or remodeling [123, 142]. In the case of an evolving network, the macroscale parameters would necessarily have to be refit at each step. Knowing the deformation state at the previous step could allow for efficient re-fitting, but there is much work still to be done to identify the optimal strategy for such problems. Similarly, in particular in the case of the arterial wall, multicomponent models are important at both the microstructural [104, 122, 124] and macrostructural [143–146] scales, and the best strategy to fit a multicomponent, discrete-fiber microstructural model is by no means clear and has not been explored in this work.

Lastly, compressing the network in the direction in which most fibers are aligned might result in average of fiber stretch ($\hat{\lambda}_f$) less than one. In this case, some fibers are still stretched leading to a rise in the strain energy. The fitting procedure will be unable to capture these behaviors, and such artifacts will cause an increase in the stiffness of the model, since the slope of W^f vs. λ^f curve, i.e. stress, will be artificially increased as the fit attempts to match the network when average stretch becomes greater than one (i.e. W_f has been increasing from the network model since some fibers are in tension, but the overall average $\hat{\lambda}_f$ is still less than one, thus the fit must be stiffer than the network in order to minimize the distance between the curves). Conversely, as observed in the example given in Figure 2.7, it is also possible for the average fiber stretch $\hat{\lambda}_f$ to give a value greater than one, while the true average is less than one. This would indicate that the fibers themselves have a negligible effect on the behavior. While this might be true for a specific deformation, it is, in general, not an accurate representation of the material, and thus requires special care to be taken in the fitting process. These problems are mostly theoretical, since tissues are almost always loaded in the direction that their fibers are aligned, but it is nonetheless

important to make sure there is a method for dealing with this issue in this framework. We offer one solution in this work, but it is by no means the only way to deal with this issue.

2.5 CONCLUSIONS

In this work, we have demonstrated a novel technique for simulating multiscale biological tissues. This work focuses on simple microstructures applied to complex finite element geometries, but this technique can be expanded for any microstructural model. The present method gives us flexibility to perform large-scale simulations while maintaining microstructural detail.

CHAPTER 3

Load Transfer from Tissue to Neuron: Computational Analysis of Mechanical Differences between Facet Capsular Ligament and Collagen Gel Experiments

I was taught that the way of progress
was neither swift nor easy.

Marie Curie

3.1 INTRODUCTION

Back and neck pain is a leading cause of activity limitation [1–3]. Many sources for back and neck pain have been recognized, including the facet joint and its highly innervated capsular ligament [3, 147, 148]. The facet capsular ligament, a fibrous connective tissue encapsulating the posterior articular facet joints of adjacent vertebrae, plays a variety of mechanical and sensory roles in the spine. The facet capsular ligament helps to control and restrict the spinal motion, redirect spinal load, and maintain spinal stability [9]. Being highly innervated, the facet capsular ligament also plays a mechanosensory roles, including propagation of proprioceptive (position) and nociceptive (pain) signals to the brain [11–13].

The facet capsular ligament is a viscoelastic fibrous tissue that consists of two main regions: an elastin-rich inner region and a collagen-rich outer region [11, 12, 30, 39]. The unique microstructural composition of the facet capsular ligament enables it to undergo large strains [12]. Back and neck pain can be associated with excessive tension on the axons embedded in the facet capsular ligament [8]. This tension is believed to depend on both the magnitude and the rate of strain applied to the tissue [14–16]. Specifically, high-magnitude macroscale tissue strains due to excessive ligament elongation and/or strain rates can deform and reorganize the microstructure surrounding a neuron in the tissue, activating mechanosensitive ion channels of the cell membrane and resulting in the release of pain signals [14, 15, 17–19]. Several studies have shown that repetitive cyclic loading of the facet joint and its ligaments, even within the normal physiological range of the motion, can

cause laxity across the joint and increase the risk of mechanical instability in the spine [20–22]. Whiplash studies on the cervical facet capsular ligament suggest that a higher loading rate may correlate with microstructural changes and consequently cause laxity and pain in the tissue [22–25]. While all these studies have demonstrated a potential correlation between the loading rate and the changes observed in the tissue's mechanical response, much remains unknown about the relationship between tissue loading rate, microstructural loading, and neuronal response.

Since the facet capsular ligament's extracellular matrix primarily consists of type-1 collagen fibers [149], tissue-equivalent gel models involving axons embedded in collagen gels are an attractive choice for *in vitro* models of the facet capsular ligament's axonal responses to different environmental stimuli [14, 32–34]. These axon-gel models provide a simplified system to explore the effects of macroscopic loading on the microstructural reorganization of the collagen network and the neuronal response. Although collagen-gel-based models provide an experimental setting for systematic isolation and measurement of the contribution of different tissue constituents, one must be cautious in applying the results of gel model experiments to the native tissue response because of the inherent structural differences between the collagen gel and the facet capsular ligament. Specifically, differences in collagen concentration between gels (low concentration) and tissue (high concentration) must be considered. For example, it has been found that variation in collagen matrix concentration affects matrix stiffness and changes axonal outgrowth, resulting in more growth at lower collagen concentration [35, 36]. In their experiments, Cullen et al. [35] also showed that the neurite survival rate did not change with collagen concentration in gels exposed to a non-injurious deformation rate but decreased significantly with increasing collagen concentration in gels exposed to a high deformation rate. Thus, the question must be asked whether and how the differences between collagen gels and native ligament lead to differences in the stresses and strains experienced by an embedded neuron.

Since local axon strain is difficult to measure experimentally in realistic situations, computational models have been developed to analyze load transmission between a collagen gel and an axon [150–152]. Chan et al. [152] used confocal microscopy to generate an image-based multiscale finite-element model of dorsal root ganglion neurons embedded in a collagen gel, analyzing the strain distribution within the neuron due to macroscopic loading of the gel. They showed that the neuron-loading configuration is a determining factor for strain distribution over the neurons. They also showed that the macroscopic loading on the surrounding matrix can be amplified in the neuron such that even a moderately stretched tissue could lead to microscale neuronal injuries. By modeling a reinforced elastic cylindrical axon embedded in a non-linear elastic collagen fiber network, Zarei et al. [151] examined the effect of collagen concentration and collagen alignment on the forces and strains acting on the axon in different macroscopic loading cases. Their model showed that in all deformation cases, higher collagen volume fraction resulted in higher strains over the axon while fiber alignment only affected the axonal strain field during the transverse and axial deformation. Following this study, Middendorf et al. [150] used a similar model to examine the effect of network heterogeneity on the strains transmitted to an axon during uniaxial elongation. Although these studies provide insights on how the network structure surrounding the axon can affect the strains applied locally to the axon, they did not consider the effect of collagen viscoelasticity on the resulting strain field over the axon. In addition to the simple viscoelastic effect, there is also potential for complexity arising from highly interconnected viscoelastic fiber networks [132].

Expanding upon previous studies, we developed a computational method similar to [150, 151] to explore the effect of macroscopic strain rates, spanning a relevant range of values, on the viscoelastic micromechanical environment of an embedded neuron in the gel (lower collagen concentration) and tissue (higher collagen concentration) models.

3.2 METHODS

To model the fibrous environment of an innervated collagen matrix such as the facet capsular ligament or co-cultured collagen-axon gel, a 3D discrete fiber network model containing a cylindrical representation of an axon was created (Figure 3.1a-d) by modifying our previous discrete fiber models [150, 151]. Briefly, 3D Delaunay networks were created computationally using MATLAB (R2019a, MathWorks, Natick, MA). Each network contained a set of randomly distributed seed points representing the fiber network nodes. The edges of the Delaunay triangles represent collagen fibers. Networks with different collagen volume fraction (the ratio of the total volume of all collagen fibers to the domain volume) were generated to represent gel and tissue. The global collagen volume fraction of each network was adjusted by changing the number of the initial seed points in relation to the network's side dimensions while maintaining two conditions: (1) the fiber diameter was kept constant for all networks at 50 nm [153], and (2) the average fiber length was kept between 5% to 10% of the domain size. The gel representative networks were generated with a collagen volume fraction of 0.002 to match the collagen concentration of 2mg/mL in an existing experimental gel system [154]. Tissue representative networks were created with collagen volume fraction 0.04 and 0.1, much larger than gel representative networks. Networks were either isotropic or aligned in the Z direction to account for the role of fiber alignment [150, 151].

The network fibers were modeled as viscoelastic 2-node truss elements in Abaqus (R2018, Dassault Systèmes, Vélizy-Villacoublay, France) to account for rate-dependent behavior of the collagen. Each fiber in this network was modeled as a Prony viscoelastic material with four time constants (Figure 3.1e) - 2, 20, 200, 2000 s for gel fibers and 0.2, 2, 20, 200 s for tissue - to cover the broad spectrum of collagen fiber relaxation time observed experimentally [154, 155]. To calculate the contribution of each time constant,

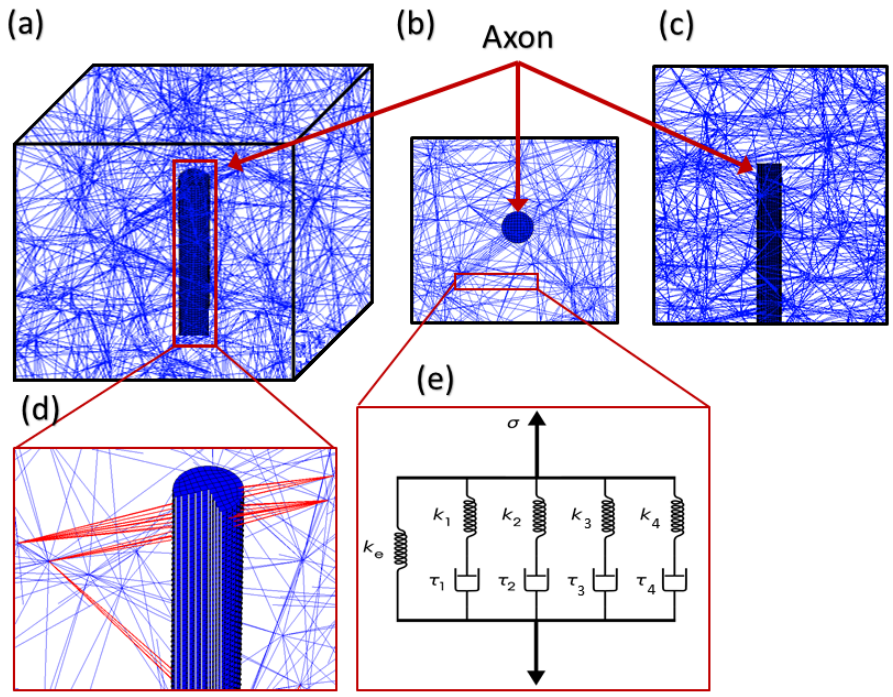

Figure 3.1: **(a)** Isometric, **(b)** top and, **(c)** side view of a 3D discrete fiber network model containing a cylindrical representation of an axon embedded in a fiber network. **(d)** Focal adhesion connection between the collagen fibers of the network to the axon. **(e)** Representation of the Prony viscoelastic material with four time constants used as collagen fiber materials.

available experimental data were fitted to a Prony series, and parameters were optimized so that stress relaxation results for a fiber network (without axon) matched the first Piola-Kirchhoff (PK1)-stress (S) - vs. – time (t) behavior for stress relaxation gel (Figure 3.2a, c) and rat facet capsular ligament (Figure 3.2b, d) experiments [154, 155]. This fitting process had 2 main steps. First, the normalized behavior of relaxation experiments of gel [154] and tissue [155] was fitted to a set of four exponential equations (Eq. 3.1) to find the Young's modulus (k_i) values.

$$S/\varepsilon_0 = k_0/\varepsilon_0 + \sum (k_i e^{-t/\tau_i})/\varepsilon_0 \tag{3.1}$$

where k_0, k_i, and τ_i are equilibrium Young's modulus, dynamic Young's modulus and time constant, respectively. Second, the parameter values were corrected based on simula-

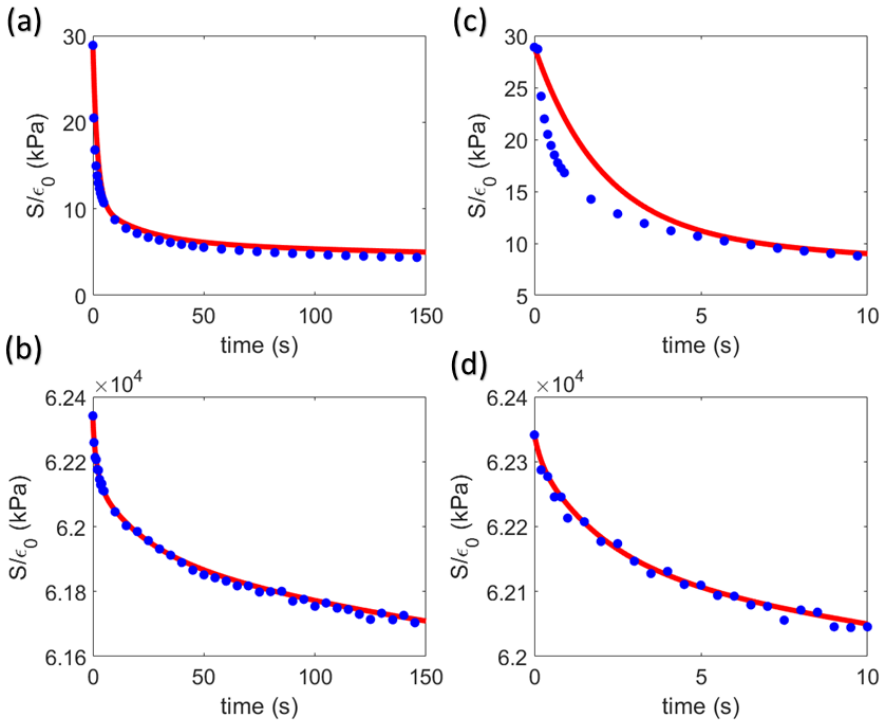

Figure 3.2: Parameter optimization by fitting the simulation (red line) to the experiment (blue dots) for **(a)** gel and **(b)** tissue. Blow-ups of the first 10 s of **(c)** gel and **(d)** tissue experiment.

tion of a 40×40×50 μm^3 fiber network for the gel model or a 16×16×16 μm^3 fiber network for the tissue model to find the value for fiber Young's modulus (k_0). This process was done iteratively, with the value of the Young's modulus adjusted such that the maximum PK1 stress from the network simulation matched the maximum PK1 stress of the experiment. The final fits are given in Figure 3.2, and the model parameters in Table 3.1.

Imaging of the cervical and lumbar facet capsular ligament has shown a large variety of fiber orientations [42, 45]. To explore the role of fiber orientation on the resulting strain fields affecting the axon at different loading rates, we performed the simulation with isotropic and mildly aligned networks for both the gel and tissue models. The degree of alignment of the networks was defined as the difference between the largest and smallest eigenvalues of the network orientation tensor, H_{ij}, with values in the range of zero, for the isotropic networks, and one, for fully aligned networks [42].

Table 3.1: Material properties and fitted viscoelastic parameters used in simulations

Component	Material Type	Parameter	Value for CVF = 0.002	Value for CVF = 0.04 and 0.1
Collagen Fibers	Linear viscoelastic, $F = k_0/\epsilon_0 + \sum(k_i \exp(-t/\tau_i))/\epsilon_0$	$\tau_i(s)$	2	0.2
			20	2
			200	20
			2000	200
		k_0 (GPa)	12.4	3278 and 5260
		$k_i(Nm^{-1})$	0.6616	0.0006
			0.1438	0.00259
			0.0668	0.00315
			0.0803	0.0074
Focal Adhesion Fibers	Linear viscoelastic, $F = k_0/\epsilon_0 + \sum(k_i \exp(-t/\tau_i))/\epsilon_0$	$\tau_i(s)$	2	0.2
			20	2
			200	20
			2000	200
		$k_i(Nm^{-1})$	*	*
Microtubules	Linear Elastic, $F = k\Delta L$	$k(Nm^{-1})$	0.942	0.94
Axon background material	Linear Elastic, $\sigma = E\varepsilon$	Young's Modulus (MPa)	4.33	4.33

* The spring constants for the focal adhesion fibers were set equal to half the corresponding k_i values for collagen fibers.

$$H_{ij} = \frac{1}{L^{(T)}} \sum_{k=network\ fibers} L^{(k)} a_i^{(k)} a_j^{(k)} \tag{3.2}$$

H_{ij}, $L^{(T)}$, $a^{(k)}$ and $L^{(k)}$ are the network orientation tensor, total length of all the fibers in the network, orientation of the fiber k and length of fiber k. The anisotropic networks studied herein had $H_{max} - H_{min} = 0.4$.

Once the collagen networks had been generated and fully characterized, a cylindrical space with diameter 2 μm and length equal to the half of network domain length was removed from the middle of the network to open up the space for the finite element representation of a cylindrical shape axon following [150, 151]. The diameter of the axon was selected based on histological images [13, 156]. The cylindrical representation of the axon was generated and meshed in Abaqus. A set of mesh independence studies including an axon subjecting to tensile loading on one end were performed to determine the optimal

mesh size (0.2 μm) to balance computational cost and accuracy. The cylinder was modeled as a composite of an elastic material reinforced with linear longitudinal microtubule fibers along the cylinder axis and circumferential nonlinear fibers wrapping around the cylinder perimeter (Figure 3.1 d). The elastic background material was modeled with 8-node linear brick (C3D8) elements using modulus $E = 4.33MPa$ to account for non-microtubular constituents of the axon such as microfilaments, neurofilaments, and axoplasm, as was used previously in [150, 151]. The microtubular fibers form the cytoskeletal architecture of the axon and are considered a primary factor contributing to the mechanical stiffness of the axon [157]. They were modeled with 2-nodes linear connector elements (CONN3D2) by connecting every node to its nearest node along the cylinder axis. The connector stiffness was set to $0.94N/m$ as was used previously in [151]. The circumferential fibers were defined as nonlinear connector springs [133] that wrapped around axon's perimeter following the force-stretch constitutive equation:

$$F = AS/B \left[\exp\left(\frac{B\left(\lambda^2 - 1\right)}{2} \right) - 1 \right] \tag{3.3}$$

where $F,\ A,\ S,\ B$ and λ represent the fiber force, fiber stiffness, fiber cross-sectional area, fiber nonlinearity and fiber stretch, respectively. The values for these variables are given in Table 3.1.

The cylinder was inserted into the network such that the bottom surface of the cylinder was located on the lower xy-plane of the network and the central axis of the cylinder was coincident with the center of the network (Figure 3.1a). Fibers that intersected the axon were connected to it using node-node join connections. This connection type requires that two nodes collocate, so, following the method of Zarei [151], each inserted point was moved to the nearest adjacent finite-element node on the axon's surface. Then, each intersected fiber was extended to 9-12 fibers (including the initial fiber) to reduce computational

instability due to point loads. These extra fibers were connected to the original fiber node from one side, and to the adjacent axon nodes nearest to the intersected node on the other side (red fibers in Figure 3.1d), and they were made half as stiff as normal fibers. The number of fibers that intersect with the axon correlates positively with the network's collagen volume concentration and negatively with degree of alignment (anisotropy) such that in general, fibers in isotropic networks have twice as many intersections with their embedded axon as the aligned ones.

After the axon-in-network model had been constructed in Abaqus, a set of displacement-controlled relaxation simulations were performed to investigate the effect of strain rate on the tension acting on the neuron. In each simulation, the network was displaced to 10% strain at a rate of 500%/s, 20%/s, 7%/s, 4%/s, 1%/s, 0.33%/s or 0.01%/s, by displacing the top surface of the network (normal to cylinder axis) in z direction while the opposite surface (including network and axon) was kept fixed with respect to all 6 degrees of freedom (DOF). The side surfaces of the network were free to move in the z direction and kept fixed in the other directions. To allow network contraction during stretch, the fibers with one node close to or attached to the side faces of the network were made two orders of magnitude less stiff than the rest of the network. Since cylinder height was considerably smaller than network height (half the length of the network height), the displacement of the network boundary was transferred through fiber-cylinder connections.

All simulations were performed in Abaqus CAE Standard using Visco analysis, and the overall average and the average of the top 1% maximum principal Green strain of the neuron elements were calculated for each network at each strain rate. To assess the variation due to random seed generation, five different networks were randomly generated for each collagen volume fraction and alignment and were simulated with all strain rates.

For very dense, three-dimensional networks, such as occur in the ligament, discrete-fiber-network models rapidly become computationally demanding, in some cases reaching

intractability. In such cases, however, the high fiber density makes a multiscale approach feasible since the characteristic tissue length scale becomes considerably lesser than the characteristic fiber segment length scale. We have explored multiscale simulations earlier in the context of purely elastic tissue-neuron intersections [151, 152], and herein we applied those principles to the viscoelastic problem, leveraging a simplified approach in which a macroscopic constitutive equation is fit to microscopic network model behavior [68]. Briefly, the approach incorporates the structural information deduced from a full multiscale model into a continuum-based finite element model without the need to run computationally expensive fully-connected multiscale models. First, a network (without an axon) undergoes a set of test deformations, and the macroscopic right Cauchy-Green tensor ($C_{ij} = F_{jk}F_{ik}$) and the volume-averaged second Piola-Kirchhoff (PK2) stress, S_{ij} are calculated. The latter is integrated with respect to Green strain, dE_{ij}, to calculate the total strain energy density function of the fiber network (Eq. 3.4).

$$W^f = \int_{E_{ij}=0}^{E_{ij}} S_{ij} dE_{ij} \tag{3.4}$$

Next, the generalized structure tensor of the network, H_{ij} (Eq. 3.2) is used to calculate the forth invariant of C_{ij}, which corresponds to the square of fiber stretch in the average fiber direction, $\left\langle \lambda_f^2 \right\rangle = \langle I_4 \rangle = H_{ij}C_{ij}$.

Finally the strain energy density of the fiber network (W^f) for all of the deformations is plotted as a function of the square root of $\langle I_4 \rangle$ and is fitted to a three-orthogonal-fiber-family strain energy density function,

$$W^f = C_2/(2C_3) \sum_{p=1}^{3} h^p \left(\exp\left(C_3 (I_4^p - 1)^2 \right) - 1 \right) \tag{3.5}$$

where C_2, C_3, h^p, I_4^p represent the fiber modulus, fiber nonlinearity, weighting factor for fiber family p, and the square of fiber stretch in the direction of fiber family p. This

strain energy density function is then used as the fiber component of the total strain energy density function, W, in a continuum model to account for the structural heterogeneity of the tissue.

$$W = W^m + W^f \tag{3.6}$$

The first term in Eq. 3.6 is the non-fiber part of the strain energy density function and is defined as a quasilinear viscoelastic (QLV) material.

For direct comparison between the discrete and hybrid models, we generated the hybrid model using the networks with identical geometrical, structural, and mechanical specifications to those of the discrete-fiber model for the high-density (collagen volume fraction = 0.1) cases. The networks were first stretched to 10 percent strain in the z-direction, and the stretches in other deformations were calculated such that the $\langle I_4 \rangle$ values for all deformations were equal to that for 10 percent z-direction stretch. The non-fiber part of the total strain energy density function was generated as a quasi-neo-Hookian material. The elastic modulus and viscoelastic parameters were equal to those calculated from the discrete model (Table 3.1). The Poisson's ratio for the non-fiber material ($\nu = 0.499$) was chosen to be nearly incompressible. The axon was generated as a fiber-reinforced composite material, as described earlier in this section. The hybrid model geometry was generated to replicate the discrete-fiber model except that we replaced the discrete networks with a continuous cubic box with the same dimensions as the discrete network domain. The axon was added to the model by partitioning a cylinder of 2 μm diameter out of the center of the box. Due to symmetry of the model, only one quarter of the geometry was modelled in the hybrid method. The boundary conditions on faces of the box normal to z direction were as in the discrete model while other faces were free. These simulations were run in FEBio Studio [135]. The displacement in the z-direction and the maximum principal Green strain within

the axon were calculated and compared to the corresponding values of the discrete-fiber network model.

Two types of hybrid models were generated and simulated in this study: (1) all the elements of the continuous cubic box had the same material model and fiber orientation as the discrete network that was deformed as a base for calculating strain energy density function parameters, (2) each element of the continuous cubic box had a material model and fiber orientation that was randomly picked from a bank of 7 different discrete fiber networks. We refer to the first hybrid model with one element type as **hybrid model with similar elements (HSE)** and the second model as **hybrid model with random elements (HRE)**. Also, for clarity, we restrict the term **maximum** to the phrase **maximum principal Green strain** where it refers to the largest eigenvalue of the local strain tensor. In contrast, **peak** is used to refer to the largest value of a measurement over time or space.

3.3 RESULTS

We begin by examining the results for fiber stress within the network, to be followed by the axon mechanics. Probability distributions of fibers' tensile stress at peak strain for 500%/s strain rate for isotropic and aligned networks are shown in Figure 3.3 along with representative deformed fiber networks. In both isotropic and aligned networks, the fiber stresses increase with increasing the collagen volume fraction (Figure 3.3 left to right). Increase in the fiber stress is more pronounced between gel and tissue representative networks (0.002 and 0.04 or 0.002 and 0.1 isotropic and aligned networks) compared to increase among tissue representative networks (0.04 networks to 0.1 networks), as would be expected given that the equilibrium Young's modulus (k_0) for the gel representative (0.002) networks ($k_0 = \ 12.4\, GPa$) is considerably smaller than the tissue representative (0.04 and 0.1) networks ($k_0 = \ 3278\, GPa$ for 0.04 networks and $k_0 = \ 5260\, GPa$ for 0.1 networks).

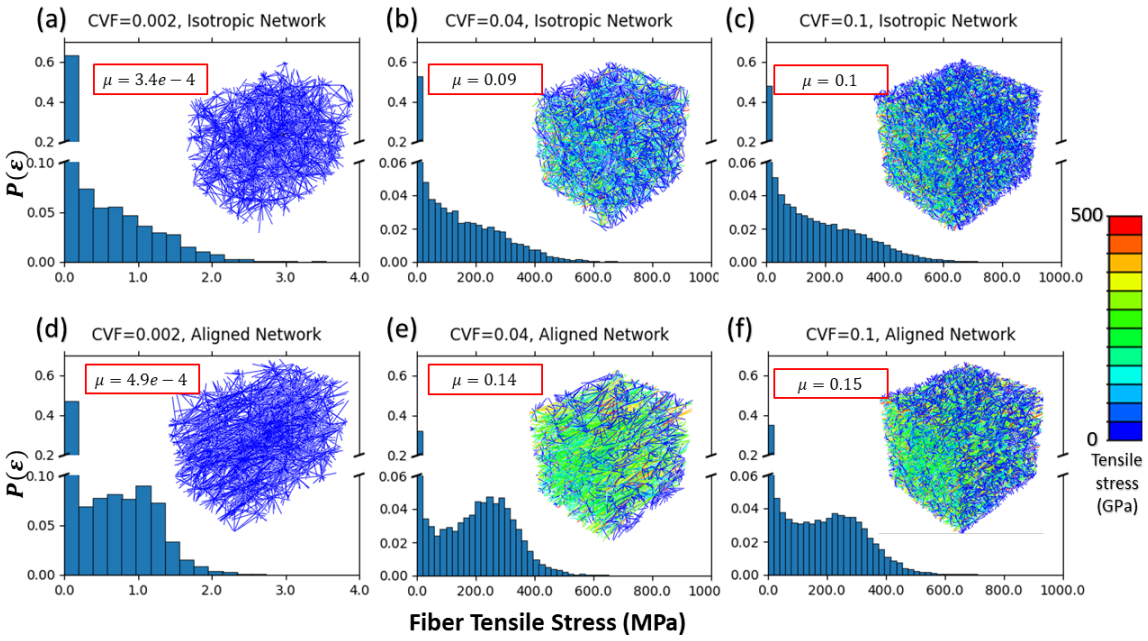

Figure 3.3: Representatives of deformed network and probability distribution of fiber maximum principal stress at 10% macroscopic stretch for isotropic **(a)** CVF = 0.002, **(b)** CVF = 0.04 and, **(c)** CVF = 0.1 networks and aligned **(d)** CVF = 0.002, **(e)** CVF = 0.04 and, **(f)** CVF = 0.1 networks. (*Network dimensions in (a) to (f) are not-to-scale. **Classes in (a) and (d) are grouped in intervals of $2 \times 10^2 MPa$ and for the rest of the graphs are $2 \times 10^4 MPa$).

Increasing the fiber alignment in the networks results in higher fiber stresses (Figure 3.3 top row vs bottom row). The probability distribution of fiber stresses seems to form a secondary peak at a non-zero stress in aligned networks in contrast to the single peak at the zero stress for isotropic networks.

Turning to the axon, probability distributions of maximum principal Green strain within the axon at peak strain for a 500%/s strain rate for isotropic and aligned networks are shown in Figure 3.4 along with axonal strain maps. The axonal strain maps (Figure 3.4) show regions of highly concentrated strain at the fiber-axon intersection, resulting in heterogeneous strain fields on axons in both isotropic and aligned fiber networks. In the low collagen volume fraction networks (0.002), the deformed axons contain a few isolated high-strain elements at the fiber-axon intersection regions, whereas the rest of the axon experiences little to no strain (Fig 4-a, d). When the collagen volume fraction is increased (left to right

in Figure 3.4), more fibers intersect with the axon, causing greater load transfer from network to axon; the mean strain in the axon (μ) increased from 0.06 (Figure 3.4a) to 0.13 (Figure 3.4b) and 0.15 (Figure 3.4c) in isotropic networks, with similar trends but lesser strains in aligned networks (Figure 3.4d-f). In general, a large percentage of elements in low collagen concentration isotropic and aligned networks (20 and 5 percent, respectively) experience zero-to-small strain (Figure 3.4a, d). In contrast as the collagen concentration increases in networks with 0.04 and 0.1 collagen volume fraction, less that 0.1 percent of elements experience small-to-zero strains (Figure 3.4 c-d and e-f). To reduce the effect of elements with negligible strain on the overall average strain values within the axon (μ) in dilute networks, a second average value, μ_+ was calculated as the average for those axon elements with strains greater than 1% of peak strain value. Removing the elements with zero-to-small strains raised the overall average values in gel representative (0.002 collagen volume fraction) networks (from 0.06 and 0.1 to 0.08 and 0.11 in isotropic and aligned network, respectively) but had no effect on denser networks. Similarly, the average strain within the axon elements increases in aligned networks (Figure 3.4 top and bottom rows). The difference between the average strain values within the axon in isotropic and aligned network increases as the collagen density increases. These results are all consistent with previous findings [150, 151]. As the collagen volume fraction in tissue representative networks increases (moving from 0.04 to 0.1 collagen volume fraction), the peak probability, and standard deviation of axon elements and skewness of the strain distribution withing the axon elements decrease.

Figure 3.5 depicts the effect of different strain rates on the overall and top 1% average maximum principal Green strain within the axon elements. The overall average maximum Green principal strains are calculated based on the entire axon elements while the top 1% average values are the average of the elements within the top 1% values of the maximum principal Green strain. The strain values represent the values averaged for 5 networks with

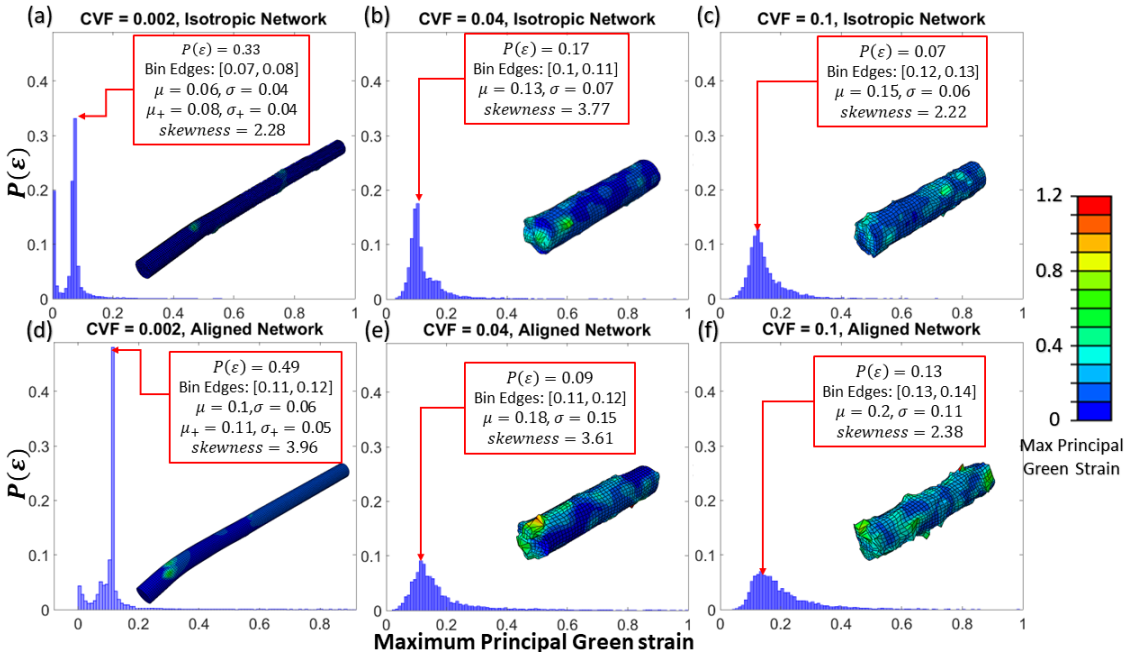

Figure 3.4: Probability distribution of maximum principal Green strain within the axon at peak macroscopic strain for 500%/s strain rate and axonal strain map for isotropic **(a)** CVF = 0.002, **(b)** CVF = 0.04 and, **(c)** CVF = 0.1 networks and aligned **(d)** CVF = 0.002, **(e)** CVF = 0.04 and, **(f)** CVF = 0.1 networks. (*Classes are grouped in intervals of 0.01; ** μ: average value of strain within axon elements; μ_+: average value of strain within axon elements after removing elements with strain less than 0.01 of peak strain).

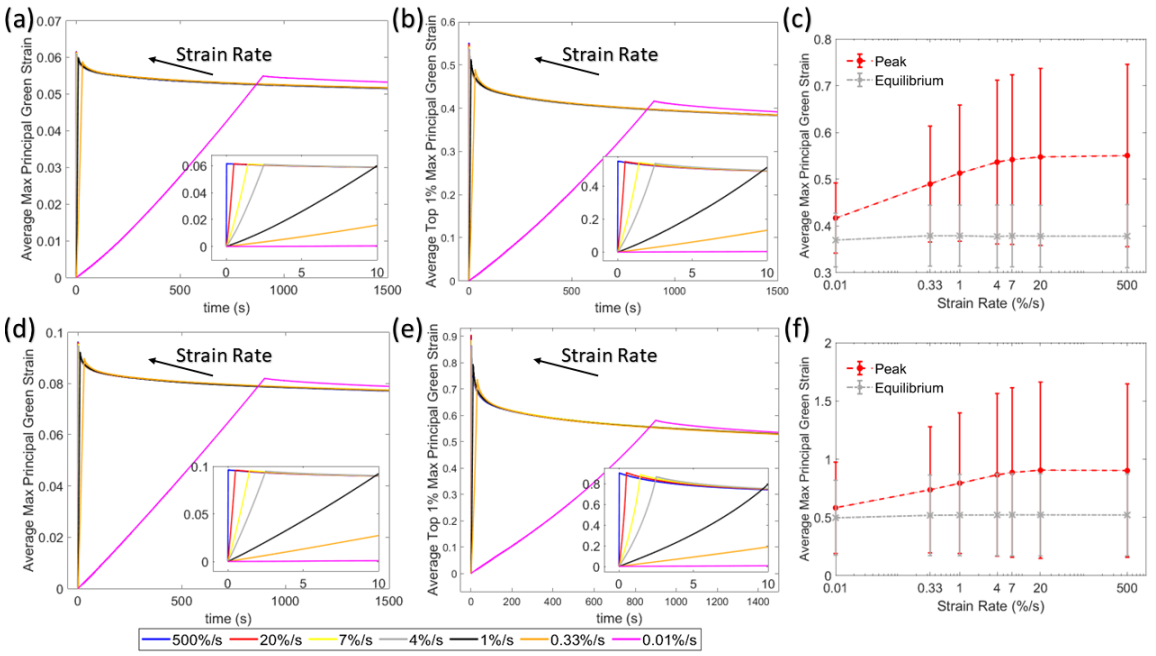

Figure 3.5: Average maximum principal Green strain vs time for **(a)** isotropic and **(d)** aligned networks with collagen volume fraction of 0.002 at 0.01%/s to 500%/s macroscopic strain rates. Average top 1% maximum principal Green strain vs time for **(b)** isotropic and **(e)** aligned networks with collagen volume fraction of 0.002 at 0.01%/s to 500%/s macroscopic strain rates. Average maximum principal Green strain at peak stretch and after reaching to equilibrium vs strain rate for **(c)** isotropic and **(f)** aligned networks with collagen volume fraction of 0.002. (Error bars represent 95% CI. N= 5).

similar collagen volume fraction and random collagen fiber architectures.

In the gel representative networks, increasing the strain rates causes both the overall (Figure 3.5a for isotropic and Figure 3.5d for aligned networks) and the top 1% (Figure 3.5b for the isotropic and Figure 3.5e for the aligned networks) average maximum principal Green strain within the axon rise to different values, which then relax to similar values after long time. All strain rates at or above 7%/s appear to increase axon strain to the same level. Increasing the strain rate from 0.01%/s to 500%/s increases the average strain by 12% and 17% for isotropic and aligned networks, respectively. The top 1% of strains were much more affected by the change in the strain rate. The top 1% of strains were increased by 32% for the isotropic and 57% for the aligned networks. For all strain rates the overall average

max principal Green strains reached a value of approximately 0.05 (isotropic networks) and 0.08 (aligned networks) after 1800sec of loading. Similarly, the top 1% of max principal strains reached approximately 0.38 (isotropic networks) and 0.52 (aligned networks) after 1800sec of loading.

To compare the effect of collagen density on the strain distribution within axon, the axon average maximum principal Green strains at peak value were plotted against the collagen volume fraction for both isotropic and aligned networks (Figure 3.6). The most striking feature of the plots is the increase in axon strain with collagen volume fraction, for both isotropic and aligned networks, at all strain rates. The higher-density networks (collagen volume fraction of 0.04 and 0.1) showed almost no effect of strain rate, as would be expected given that the tissue exhibited almost no relaxation (Fig 2b). In contrast, the gel model (networks with collagen volume fraction 0.002) showed a small but clear decrease in maximum principal Green strain at the lower strain rates, especially at the lowest strain rate of 0.01%/s. Again, this result is consistent with the gel mechanics. We recall from Figure 3.2a that the stress in the gel relaxed significantly during the first 10s of stress relaxation, so a drop in tissue stress for slower loading was to be expected.

Furthermore, the 95% confidence interval trends towards getting smaller at higher collagen volume fraction values for both isotropic and aligned networks, though the difference between the 0.04 and 0.1 collagen volume fraction values is less conspicuous. This observation was supported in Figure 3.7 where the coefficient of variation of average maximum Green strain of axon elements at peak indicates a downward trend towards higher collagen volume fraction networks for both aligned and isotropic networks, with gel representative (low collagen volume fraction) aligned and isotropic networks having larger coefficients of variation and 0.1-collagen volume fraction networks having the lowest variations. The coefficient of variation for hybrid isotropic HSE model was similar to the 0.1 collagen volume fraction discrete-fiber networks while the hybrid aligned HSE model has much smaller

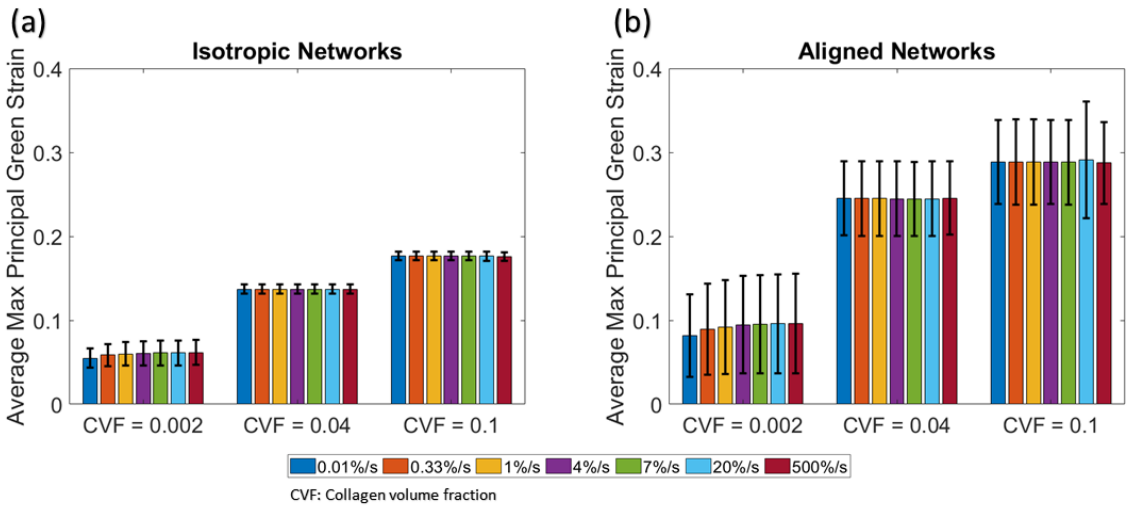

Figure 3.6: Average maximum principal Green strain at peak sample strain for strain rates of 0.01%/s to 500%/s vs. collagen volume fraction for **(a)** isotropic and **(b)** aligned networks. (Error bars represent 95% CI. N= 5). Strain rate increase from left to right within each group of bars.

variation than the corresponding discrete network model. In general, aligned networks have larger coefficient of variations compared to the isotropic networks of the same group, with the exception of HSE isotropic and aligned models. The coefficient of variation for HRE isotropic and aligned network was near zero.

A more detailed comparison between the discrete and hybrid models is given in Figure 3.8. The simulated strains were smoothly distributed within the axon in hybrid models (HSE and HRE types) compared to their equivalent of discrete network model (Figure 3.8a). Average maximum principal Green strains within the axon at the end of stretching period are predicted and shown for the discrete fiber network, HSE, and HRE models (Figure 3.8b). The average strain values for isotropic HSE and HRE models are similar to those for the isotropic discrete fiber network model, but both the aligned HSE and HRE models underpredicted the magnitude of the average maximum principal Green strain for the axon at its peak strain (Figure 3.8b), whereas the probability distribution of the strains in axon's elements are spread wider in discrete model (Figure 3.8c-d). Furthermore, comparison between isotropic and aligned, HSE and HRE models showed that the degree of

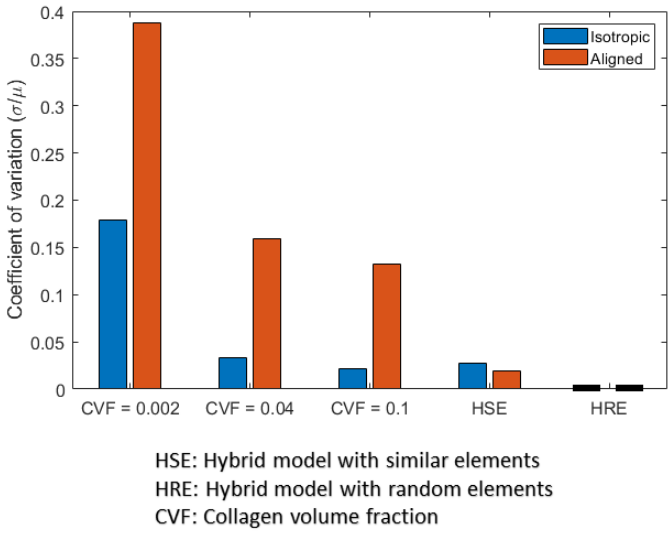

Figure 3.7: Coefficient of variation for the axon's maximum principal Green strain at 10% stretch of network for discrete fiber network models of 0.002, 0.04 and 0.1 collagen volume fraction and hybrid model with similar (HSE) and random (HRE) elements.

alignment in hybrid models seems to have an insignificant effect in the predicted strain values within the axon.

3.4 Discussion

In this work, we focused on three major differences between the gel and the facet capsular ligament: (1) The ligament is stiffer than the gel, (2) The ligament exhibits less viscoelastic relaxation than the gel, (3) The ligament has much higher collagen density than the gel, leading to a higher fiber density. We discuss the consequences of these differences in turn in the subsequent paragraph.

The major effect of the stiffness differences between the gel and tissue is a large change in the load transfer to the axon (Figure 3.6). For the same macroscopic stretch, the average peak maximum principal Green strain was almost three times higher in the tissue case than in the gel case. This result is intuitive and is consistent with previous findings [150, 151], but it is important to emphasize when interpreting gel experiments vs. tissue experiments.

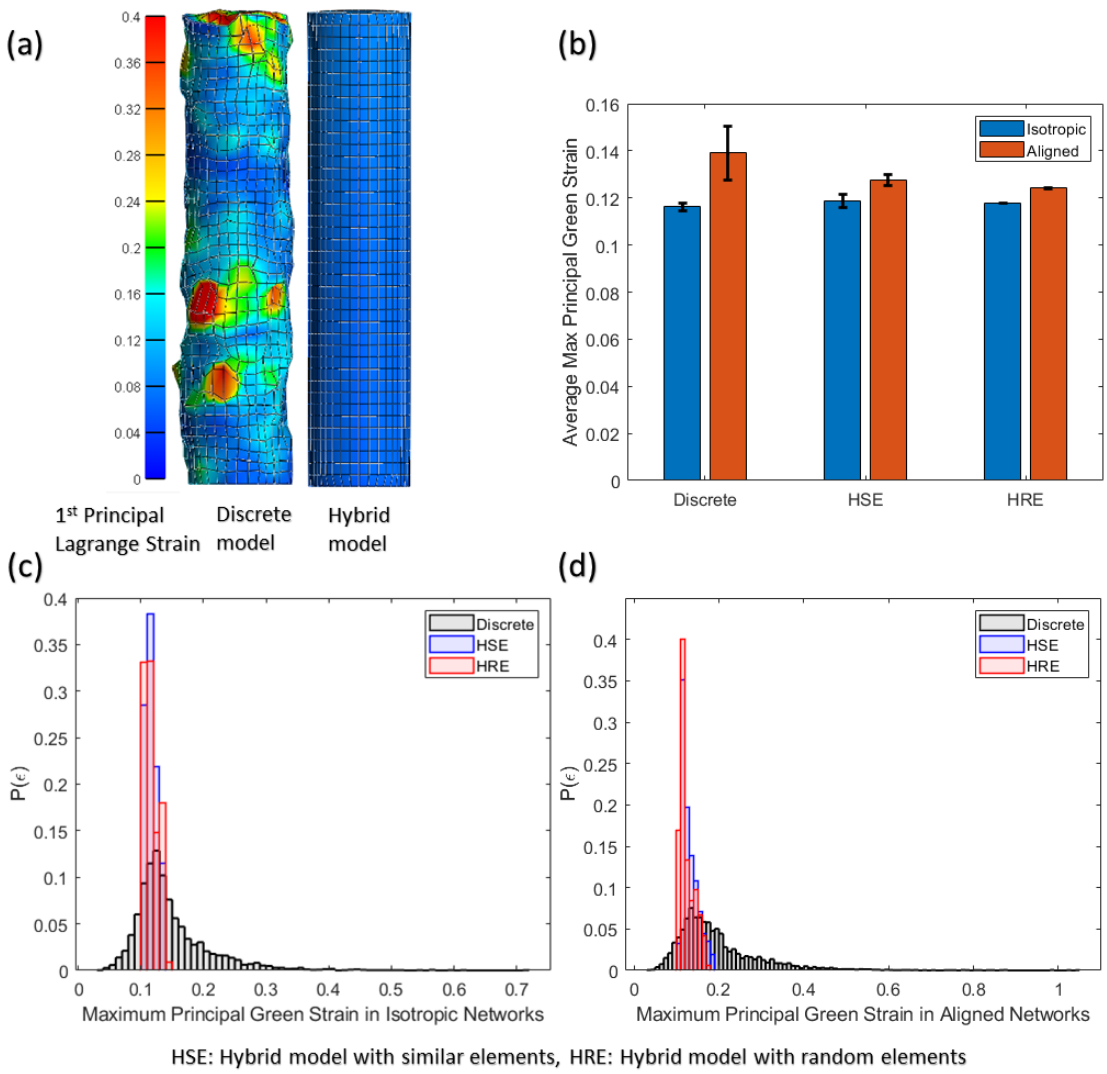

Figure 3.8: **(a)** Strain distribution within axon in hybrid and discrete model at 10% macroscopic stretch of network in equilibrium stretch. **(b)** Average maximum principal Green strains within the axon at peak for the discrete fiber network, HSE, and HRE models in equilibrium stretch. Probability distribution of maximum principal Green strain within the axon at peak macroscopic strain for the discrete fiber, HSE, and HRE **(c)** isotropic and **(d)** aligned models in equilibrium stretch.

Qualitatively similar results were seen in both isotropic and aligned networks, with larger strains in the aligned case.

There was also a discernible difference between the gel and tissue models in the context of viscoelasticity. Stress relaxation data (Figure 3.2 [154, 155]) showed that a 2 mg/ml collagen gel can relax up to 70% of its peak stress over time, whereas the rat cervical facet capsular ligament relaxes only about 1% of its peak stress. The consequences of this difference are particularly evident at lower-rate stretch conditions. The peak strain in the simulated gel experiment start to drop off at stretch rates of 1%/s, and the peak strain at a stretch rate of 0.01%/s was 12% and 17% lower than that at 500%/s for isotropic and aligned networks, respectively. In contrast, the simulated tissue stretch has almost no rate dependence, as would be expected for a tissue that is nearly elastic in its behavior. Importantly, and a point to which we will return shortly, the biological consequences of loading at high rates are quite different but are not addressed in this study; rather, we find that the tissue mechanics are largely rate-independent, so the amount of strain being transferred to the neuron would be rate-independent.

Turning to the effect of high fiber density, the tissue model had many more axon-fiber contacts than the gel model, resulting, in general, in a smoother distribution of load over the axon for the tissue case. This effect was seen in the coefficient of variation in strain values over the axon (Figure 3.7), which decreased monotonically with collagen density. For all discrete-fiber models, variation was notably higher in aligned networks, which tend to have fewer fiber-axon contacts for the same fiber density. We note that this difference is a consequence of the way we generated the models and may not be the case in the actual tissue and gel system.

The results of Figure 3.8 showed that the hybrid model can be a good substitute for the discrete-fiber network model if the average max principal Green strain within the axon is the purpose of the desirable, whereas, if the high-strain elements in the axon are desired,

then, the discrete-fiber network model is a better candidate.

Summarizing these observations, we conclude that the strains experienced by an axon embedded in a collagen gel are likely lower than those that would arise *in vivo* under the same tissue loading conditions, the result of both the lower stiffness and the more pronounced viscoelastic relaxation of the gel. Thus, the gel model is a conservative one in the context of mechanics – a macroscopic strain protocol might produce enough strain to injure an axon in model because of less efficient strain transfer.

As noted earlier, this study addresses the question of how mechanical and structural differences in the collagen fiber network affect the transfer of strain from the macroscopic (tissue) to the microscopic (neuronal) level. It does not, and in current form cannot, address the question of how that strain transfer affects the neuron or what specific cellular mechanisms respond to that strain. Those are extremely important questions, and indeed the nature of how the neuron senses and response to an imposed stretch may affect how it responds differently to different stretches or stretch rates. While our computational models can inform and be informed by experiment, they are limited in that they can only explore issues that are within their scope.

Even within its modest, mechanical scope, there are some model limitations that should be considered. First, this model did not consider any viscoelastic properties for the axon. In vivo, however viscoelastic properties of axons are expected to be important in axon's response to high rate deformations [158]. Additionally, the axon in our model was simplified to a cylinder placed in the center of the domain. However, an axon in a collagenous tissue such as facet capsular ligament has an extremely complex geometry which needs detailed high resolution imaging techniques to replicate its geometry [152]. Second, all the rate dependent deformations were limited to elongation of the network along the axon's length and no shear or transverse deformation were tested in this study.

CHAPTER 4

Estimating Cervical Facet Capsular Ligament Mechanics Based On Subject-Specific Anatomy and Kinematics

As always in life, people want a simple answer, and it's always wrong.

Susan Greenfield

4.1 INTRODUCTION

The cervical spine is a complex structure, comprised of the uppermost seven vertebrae of the spinal column (C1 to C7), intervertebral discs, and various other soft tissues. In addition to supporting the head and protecting the spinal cord, the cervical spine is the most mobile spinal region allowing a wide range of head movement and flexibility. Consequently, it is highly susceptible to injury. Neck pain is a leading cause of activity limitation, affecting 30-50% of the U.S. population annually [1]. Sources of neck pain are diverse and often unknown [4], spanning from degenerated joint [3, 148, 159] to degenerated disc [7, 160, 161] and ligaments [5, 148, 162, 163]. The highly innervated cervical facet capsular ligament, a fibrous connective tissue encapsulating the posterior articular facet joints of adjacent vertebrae, has been recognized as a potential source of neck pain [3, 5]. Because our understanding of facet joint mechanics remains incomplete [8], current noninvasive treatments cannot offer long term relief while invasive treatments have undesirable side effects on the mechanical functionality of the spine [3, 5].

Numerous experimental studies have been developed to distinguish the role of the facet capsular ligament in neck instability and pain [5, 13, 17, 24, 26–29]. For instance, Quinn et al. [27] showed that joint retraction simulating neck injury after trauma could alter cervical facet capsular ligament's collagen fiber organizations and consequently reduce ligament stiffness and increase ligament laxity. Numerous in vitro studies have also identified a relationship between extreme elongation of the facet capsular ligament, capsular ligament

laxity, and the resulting microstructural changes in the capsule fiber organization [24, 29, 31]. Whereas experimental data of this sort are an important tool to characterize the facet capsular ligament's biomechanical and mechanobiological behavior, they must be complemented by determination of the in vivo kinematics experienced by the ligament during normal and abnormal motions. One approach is to develop a finite element (FE) model of the cervical spine, simulating the motion segment and its components' behaviors as the vertebrae move. The objective of FE models is to estimate the stresses and strains in the spinal tissues under various loading conditions, such measurements being difficult or impossible in experimental examination [38, 53–56]. These FE models can ultimately facilitate the development of subject-specific models that can be adopted as a complimentary tool in clinical settings to advance prevention, diagnosis, and treatment plans in cervical injuries. The subject-specific modeling approach can be particularly attractive when patient's anatomical and kinematic data are available.

Every individual has unique spinal geometry, kinematics, and tissue properties. To design a true subject-specific FE model of the facet capsular ligament, the specificity of all these components would need to be considered. Recent advances in imaging technologies have led to individualized, image-based FE models of the cervical spine [38, 53, 54, 56–62]. In these studies, the vertebral geometries were reconstructed by processing and segmentation of diagnostic images such as computed tomography (CT) and magnetic resonance imaging (MRI) scans. The cervical ligaments, including facet capsular ligament, however, were usually represented as two-node, nonlinear, tension-only truss or spring elements [38, 53, 54, 56–59, 63]. These simplified representations of facet capsular ligament can provide insight into how the ligament affects the motion of the spine, but are not as useful in determining how spinal motion deforms the ligament. Therefore, a higher fidelity 3D volumetric model of capsule is needed to study the behavior of cervical facet capsular ligament during spinal motion.

Realistic boundary conditions that accurately replicate individualized in vivo neck motion are another key aspect in generating a subject-specific FE model. Despite their detailed imaged-based geometry representation of cervical spine, many studies have applied a simplified load, typically a rotational moment or a combination of several rotational moments around the vertebra's center of rotation [53, 54, 56–59, 61]. While this approach has merit and can provide general insights, it ignores the considerable variation in motion across individuals [164].

The output of an FE biomechanics model depends on the tissue constitutive model(s) used therein. In most cases, however, it is not feasible to obtain in vivo subject-specific material properties of cervical facet capsular ligament. Therefore, most FE studies of the cervical spine rely on soft tissue material properties from the literature. Recognizing the importance of interpatient variability, many studies have investigated the effect of various material nonlinearities [37–41] on the mechanical response of the facet capsular ligament and the spine as a whole. In their models of the C5-C6 motion segment, for example, Wang et al. [38] investigated the effect of ligament degeneration on segmental mobility by changing the stiffness value of the left C5-C6 cervical capsular ligament. Mattucci et al. [39] measured the mechanical properties of cervical spinal ligaments, including the facet capsular ligament, in a range of physiologically relevant elongation strain rates. In these studies, the mechanical behavior of the tissue was measured based on the macroscopic strain within the tissue. The cervical facet capsular ligament, however, is a fibrous tissue with a heterogenous collagen fiber organization throughout the tissue. Macroscopic tissue behavior has been shown to be dependent on its microscopic structure [37, 42]. Therefore, to study the complex mechanical behavior of the cervical facet capsular ligament, a multiscale approach is needed.

The goal of this study was to develop and demonstrate a method to create 3D subject-specific models of the lower cervical spine (C4-C7), with a focus on facet capsular ligament

biomechanics. This model incorporates individual spine geometry and replicates individual vertebral kinematics. Because subject-specific tissue properties were not available, image-based heterogeneous fiber structures from [27, 44] were incorporated in a hybrid multiscale model [68] to define nonlinear material properties for the facet capsular ligament.

4.2 METHODS

4.2.1 Overview

In this study, a model of a healthy 23-year-old female's cervical spine was developed using subject-specific bony geometry and vertebral motion. The facet capsular ligaments were implemented and executed in FEBio Studio [135]. Figure 4.1 briefly describes our methodology to generate the model. The geometries of vertebrae C4-C7 were created by segmenting the skeletal surfaces from CT scans (0.22x0.22x0.6 mm; 1.8 mSv; Siemens AG, Munich, Germany) of the participant's cervical spine (Figure 4.1a). The segmented geometry was then used as an initiation point to generate the facet capsular ligaments' geometry (Figure 4.1b), and digitally reconstructed radiographs (DRR) of C4-C7 that were used to extract the vertebral kinematics from biplane videoradiography (Figure 4.1c) [165]. The fiber structures and material characteristics of the tissue were specified based on available cervical facet capsular ligament data [27, 43, 44] and were incorporated in a hybrid multiscale model [68] to generate fiber characteristics for the facet capsular ligaments. The geometry, intervertebral kinematics, and constitutive material models were subsequently imported into FEBio Studio [135] to form the final FE model (Figure 4.1d).

The kinematically-driven subject-specific model was then compared with a model with neo-Hookean material definition, a generic geometry, and a model with mismatched geometry and kinematics (when the geometry of one subject is used with the kinematics of another) to study their respective effect on the model output.

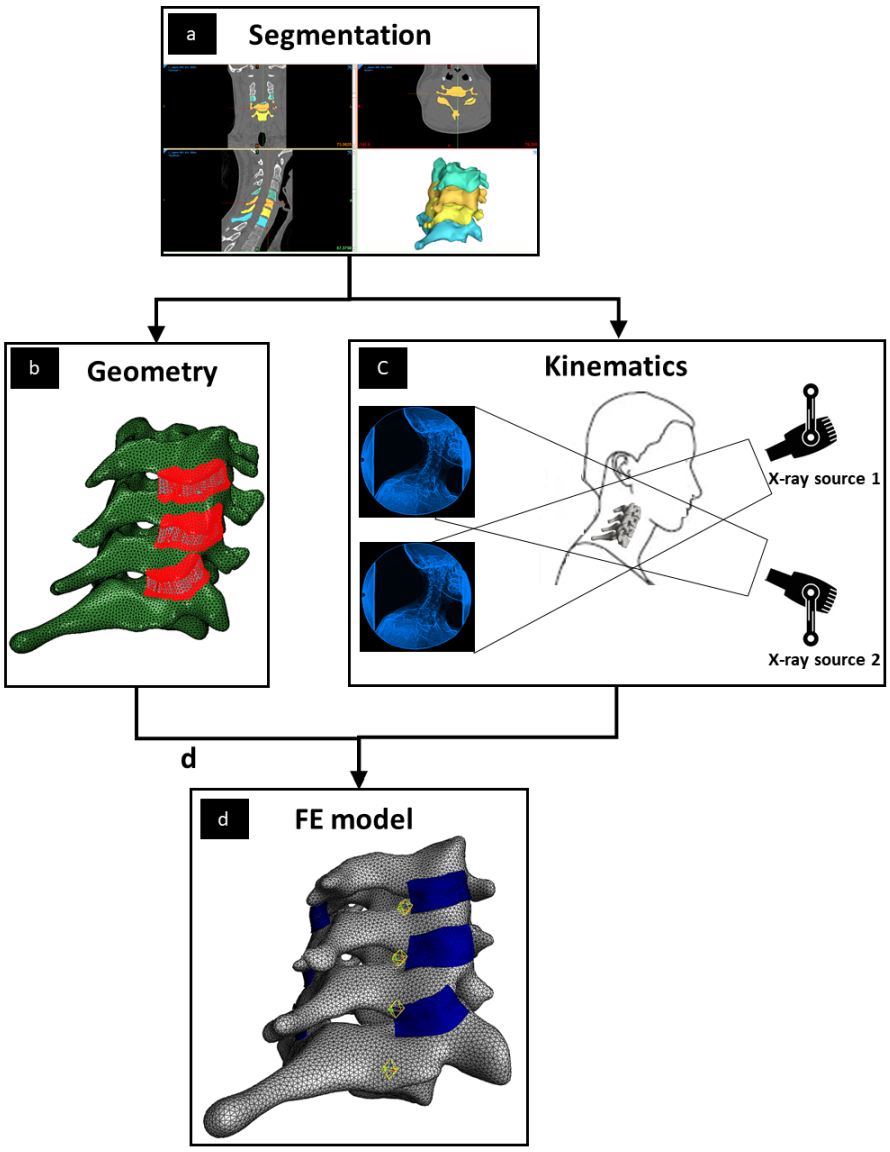

Figure 4.1: The overview of the methodology to generate a kinematically-driven, subject-specific model of a healthy 23-year-old female's cervical vertebrae and facet capsular ligaments. (a) Bone segmentation to generate the vertebral body. (b) Process of generating 3D geometry of facet capsular ligaments. (For more detail see Figure 4.2). (c) Biplane videoradiography to extract kinematics for the neck motions. (d) Resulted FE model of the lower cervical vertebrae and facet capsular ligaments.

4.2.2 Experimental Protocol

The subject-specific model was created from data collected from a healthy 23-year-old female with no history of neck pain. Consent was obtained in accordance with the University

of Minnesota IRB. A cervical spine CT scan was acquired (Siemens AG, Munich, Germany) with a radiation dose of 1.8 mSv and 0.22 x 0.22 x 0.6 mm voxel size. Kinematic data were collected using a custom biplane videoradiography system (Imaging Systems & Services, Inc. Painesville, OH, USA) with imaging parameters 160mA, 70kV, 30Hz, 0.16 mSv/trial. The participant performed 3 trials each of axial rotation (AR), lateral bending (LB), and flexion-extension (FE) to a metronome set to 50 beats per minute. AR trials began in left axial rotation, moved to right axial rotation, and returned to left axial rotation. LB trials began in left lateral bending, moved to right lateral bending, then returned to left lateral bending. FE trials began in full flexion, moved to full extension, and back to full flexion.

4.2.3 3D volumetric mesh of vertebral bodies

The CT image stack of the participant's cervical spine was imported into image processing software (Materialise Mimics, v23, Materialise NV, Leuven, Belgium), and the 3D vertebral shells of C4-C7 were segmented out using an automatic threshold mask based on pixel intensity, followed by manual refinement (Figure 4.1a). The resulting 3D surface meshes (3-node triangles – tri3) were created and exported in STL format using a custom MATLAB program that retains the same coordinate system between the extracted geometries and the shape-matching images. The 3D surface meshes were then re-meshed using 4-node tetrahedra (tet4) in Materialise 3-Matic (v15, Materialise NV, Leuven, Belgium) to construct volumetric geometries of the cervical vertebrae. The 3D volumetric meshes of vertebral bodies were imported into the FEBio Studio [135] software as rigid bodies.

4.2.4 3D geometry of facet capsular ligaments

Extraction of facet capsular ligament geometry from participants in vivo is not feasible due to the ligament's small size and low radiopacity. To generate the facet capsular ligament in

the model, first, we approximated the anatomy, including the insertion sites of the capsule into the bone on each side of the joint, as shown in Figure 4.2a. Next, a surface was generated using Abaqus (R2018, Dassault Systèmes, Vélizy-Villacoublay, France) to conform to the geometry and to cover the identified regions while encapsulating the facet joint. The method of Liang et al. [166] was next used to generate high quality 4-node quadrilateral (quad4) elements defining the surface (Figure 4.2b). The new surface mesh was extruded to an average thickness of 0.42 ± 0.07 mm (mean $\pm$ std) [43] to generate a volumetric 8-node hexahedron (hex8) mesh for each facet capsular ligament (Figure 4.2c). Finally, the facet capsular geometry was imported into FEBio studio [135] such that the insertion areas of the facet joints on each side of the joint conformed to the corresponding areas on the inferior side of the facet capsular ligaments.

4.2.5 Fiber structures and material properties for the facet capsular ligaments

The cervical facet capsular ligament is a collagenous tissue with high spatial heterogeneity in its collagen organization [43]. To incorporate fiber heterogeneity into our continuum FE model, we used a hybrid multiscale method presented elsewhere in detail [68] and described briefly here. First, a set of previously inferred fiber structures from quantitative polarized light imaging (Figure 4.3a) [27, 44] was used to generate fiber alignment maps (Figure 4.3b) [42, 49]. The inferred high-resolution fiber alignment maps from quantitative polarized light imaging were morphed to the planar 2D mesh map of each facet capsular ligament (Figure 4.3a-f). Then, a tensor-based averaging method was used to calculate the mean alignment strength and fiber orientation for each finite element of the 2D planar facet capsular ligament (Figure 4.3g). Next, the 2D planar orientation map was morphed back to the original 3D geometry of each facet capsular ligament (Figure 4.3h). The 3D structural information (including the mean fiber orientation and alignment strength) for each finite element was used to generate a nondimensional $1 \times 1 \times 1$ Delaunay network in MATLAB

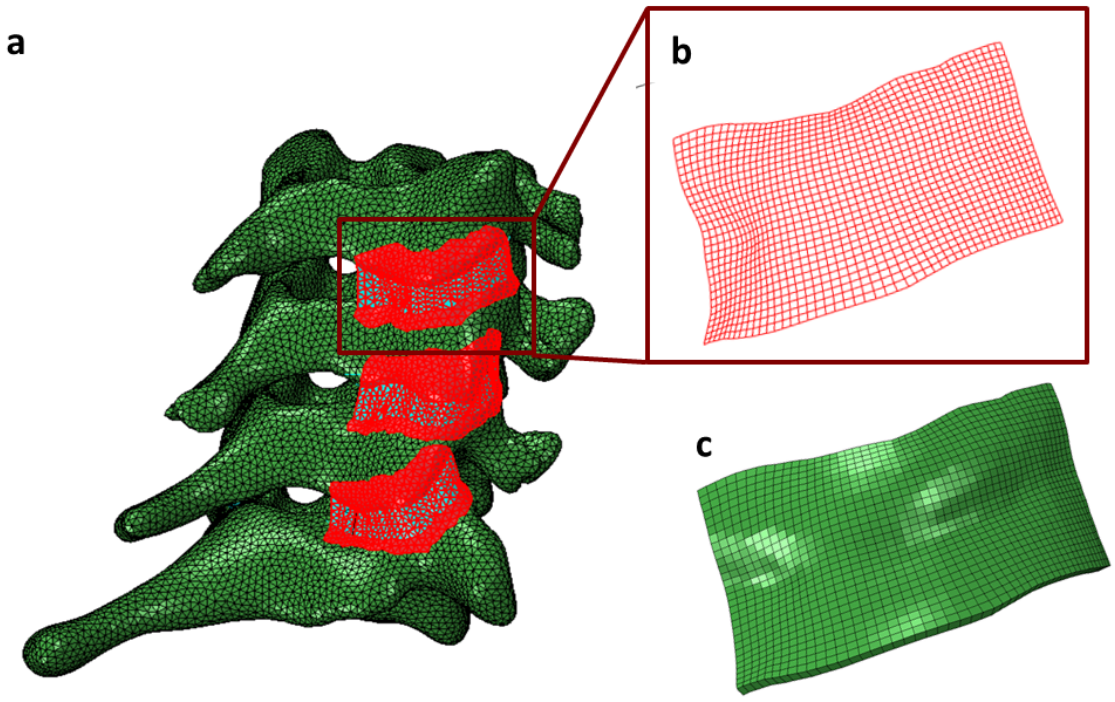

Figure 4.2: The process of generating 3D geometry of facet capsular ligaments. (a) Identifying the insertion sites of the facet capsular ligament into the bone and fitting a surface to encapsulating the facet joints. (b) Structured high quality 4-node quadrilateral-shaped mesh of the right C4C5 facet capsular ligament. (c) Extruded 8-node hexahedron-shaped mesh of the right C4C5 facet capsular ligament.

(R2019a, MathWorks, Natick, MA) to serve as a representative volume element (RVE) in computational domain [133]. Each network contains a set of randomly dispersed 3D seed points representing the network nodes. The edges of Delaunay triangular regions represent collagen fibers and can freely rotate around their contact point at each node. Networks were generated with the global collagen density (the ratio of the total volume of the collagen fibers to the overall network volume) of 0.04 [66] and the degree of alignment equal to the corresponding element's calculated alignment strength. The global collagen volume fraction of each network was adjusted by changing the number of the initial seed points in relation to the network's side dimensions while holding the fiber diameter constant for all networks (100 nm). The degree of alignment for each network was adjusted by stretching

the networks in x-direction until it reaches to the element's alignment strength. The network was then cropped to a cubic form of $1 \times 1 \times 1$ and was checked to maintain the 0.04 collagen density. Finally, the primary network alignment was aligned with the calculated fiber orientation for its corresponding element. The network fibers were modeled with 2-node nonlinear springs:

$$F = AS/B \left[\exp\left(\frac{B\left(\lambda^2 - 1\right)}{2} \right) - 1 \right] \tag{4.1}$$

where F, A, S, B and λ represent the fiber force, fiber stiffness, fiber cross section area, fiber nonlinearity and fiber stretch, respectively. The values for A and B were 324 MPa and 10, respectively [37].

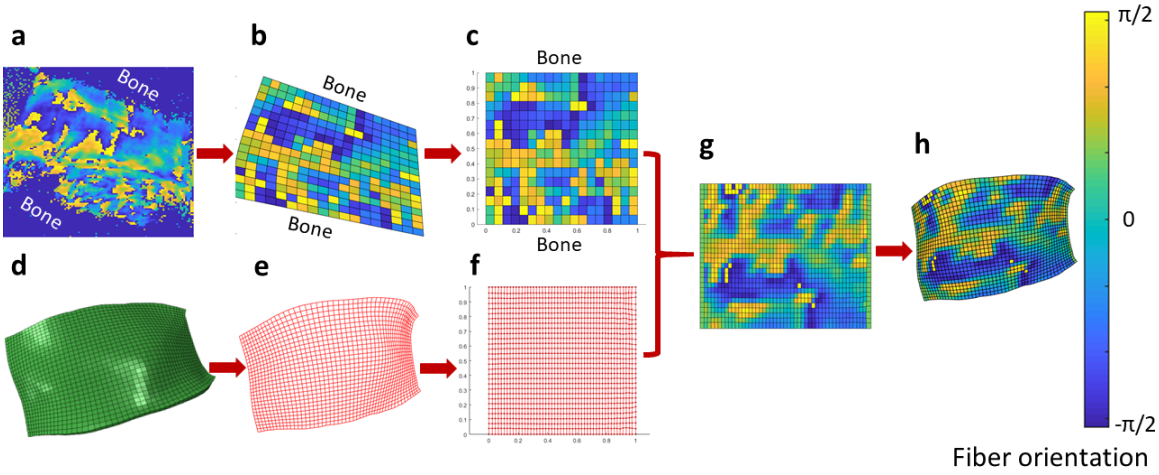

Figure 4.3: Steps to map fiber orientation onto facet capsular ligament geometry. (a) Inferred fiber structures from quantitative polarized light imaging. (b) Fiber alignment maps. (c) Mapped 2D planar fiber alignments. (d) 3D geometry of the C4-C5 facet capsular ligament. (e) Surface mesh of the C4-C5 facet capsular ligament. (f) Mapped 2D planar mesh of the C4-C5 facet capsular ligament. (g) The fiber orientation map for the 2D planar facet capsular ligament. (h) Fiber orientation map mapped to the original 3D geometry of the C4-C5 facet capsular ligament.

The fiber parameters for a three-orthogonal-fiber-family strain energy density function for each RVE network were calculated using the network-to-continuum scheme described in [68]. The goal of the hybrid model is to take advantage of the simplicity of continuous

finite element models in a structure-based multiscale model to increase efficiency. Briefly, the hybrid model incorporates the structural information deduced from a full multiscale model into a continuum-based finite element model without the need to run a computationally expensive fully connected multiscale model. To extract the structural heterogeneity of the RVE networks in this model, first, the network undergoes a set of deformations such as x-, y- and z-direction uniaxial stretch, simple shear on the xy-, yz-, and xz-faces, and equibiaxial stretch in the xy-, yz- and xz-plane and then, the macroscopic right Cauchy-Green tensor ($C_{ij} = F_{jk}F_{ik}$) and the volume-averaged Cauchy stress (σ_{ij}) [47] are calculated. The volume-averaged Cauchy stress is then converted to the second Piola-Kirchhoff (PK2) stress, S_{ij}, and is integrated with respect to Green strain, dE_{ij}, to calculate the total strain energy density function of the network:

$$w^f = \int_{E_{ij}=0}^{E_{ij}} S_{ij} dE_{ij} \tag{4.2}$$

Then, the network structure tensor, H_{ij} (Eq. 4.3) is calculated and used in $\langle I_4 \rangle = H_{ij}C_{ij}$ to calculate the square of fiber stretch in the average fiber direction.

$$H_{ij} = \frac{1}{L^{(T)}} \sum_{k=network\ fibers} L^{(k)} a_i^{(k)} a_j^{(k)} \tag{4.3}$$

where H_{ij}, $L^{(T)}$, $a^{(k)}$ and $L^{(k)}$ are the network orientation tensor, total length of all the fibers in the network, orientation of the fiber k and length of fiber k.

Finally, the strain energy density of the fiber network (w^f) for all test deformations are plotted as a function of the square root of $\langle I_4 \rangle$ and is fitted to a three-orthogonal-fiber-family strain energy density function of Eq. 4.4. This strain energy density function is then used as the fiber component of the total strain energy density function, W, in a continuum model to account for the structural heterogeneity of the model (Eq. 4.5).

$$W^f = C_2/(2C_3)\sum_{p=1}^{3} h^p \left(exp(C_3(I_4^p - 1)^2) - 1\right) \tag{4.4}$$

$$W = W^m + W^f \tag{4.5}$$

C_2, C_3, h^p, I_4^p represent the fiber modulus, fiber nonlinearity, weighting factor for fiber family p and the square of fiber stretch in the direction of fiber family p. This fiber-based strain energy density function, W^m, was combined with a neo-Hookean ground matrix (W^m in Eq. 4.5) in FEBio to form a coupled solid mixture material for each element. The Poisson's ratio and shear modulus for the neo-Hookean part of material model were 0.48 and 1.2 kPa, respectively [37].

4.2.6 Boundary conditions on the ligaments

Anatomical studies have shown that only part of the interior side of the facet capsular ligament in contact to the superior vertebra is rigidly attached to the bone, dividing the contact area to two separate parts as we call them: (1) two *ligament-bone rigid attachment regions* where the ligament is rigidly attached to the bone and is bound to move with the bone, and (2) a *sliding contact region* where the ligament is in contact with the bone but it is not rigidly bound to the vertebra and can slide over the bone (Figure 4.4b). Taking this division into account, four different types of boundary conditions were used for the ligament:

- The ligament-bone rigid attachment areas in the anterior side of the ligament (Figure 4.4b) were defined as tied connections controlled by the bone motion. These connections had full kinematic coupling (i.e., displacements $u^{ligament}$ and u^{bone} were forced to be equal).

- Areas of potential ligament bone contact without attachment were modeled as sliding

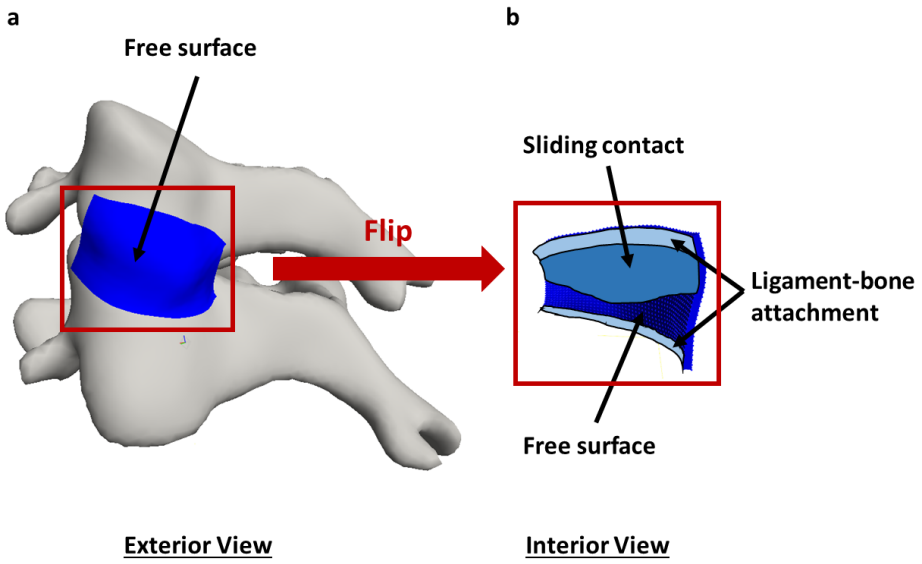

Figure 4.4: Boundary conditions on the facet capsular ligament. (a) Exterior view of left C4-C5 facet capsular ligament, showing that the external surface is entirely free. (b) Interior view of the same ligament, showing rigid attachment to bone (fixed boundary conditions) in the superior and inferior portions of the ligament, sliding contact (free motion parallel to surface but no penetration) where the ligament overlays the bone but is not attached, and free surface where the ligament overlays the joint space.

contact regions (Figure 4.4b) using the "sliding-elastic" algorithm in FEBio Studio. The boundary condition allows tangential motion of the ligament along the bone surface but introduces a penalty normal force if the ligament would overlap the vertebral domain.

- Self-contact was checked for each side of the ligament in case of folding / buckling during spinal motion.

Other surfaces were specified as free surfaces (Figure 4.4a).

4.2.7 Biplane videoradiography and shape-matching to extract kinematics for the neck motions

Biplane videoradiographic images were undistorted and filtered (DSX Suite, C-Motion Inc., USA), and calibration was performed (XMALab, XROMM) [167]. The digitally

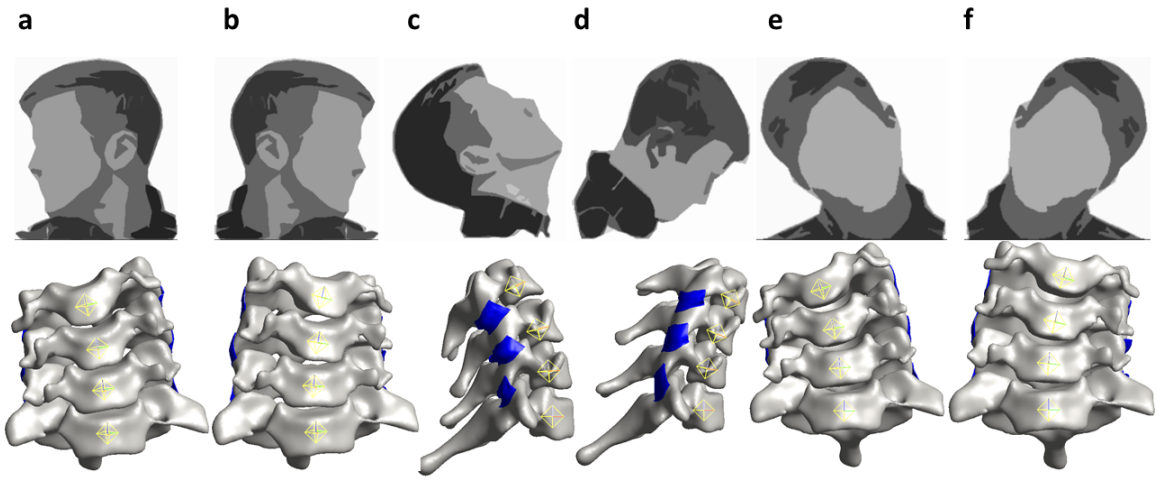

Figure 4.5: The loading configuration. (a) Axial rotation to the left. (b) Axial rotation to the right. (c) Flexion. (d) Extension. (e) Lateral bending to the left. (f) Lateral bending to the right.

reconstructed radiographs (DRR) of the C4-C7 vertebrae were created from the segmented CT scans in the same coordinate system as the exported STLs. Vertebral kinematics were computed in a semi-automated shape-matching software (Autoscoper, XROMM) [168]. Kinematic data were filtered with a moving average filter, and relative kinematics were extracted (Kinematics Toolbox v4.0, Becky Lawrence, PT, PhD).

4.2.8 Loading configuration and FE analysis

Prescribed displacements were applied to the bone geometries based on the kinematics extracted from biplane videoradiography [165]. First, the kinematic data were transformed into a fixed-C7 coordinate system. Then, to simulate each motion in FEBio, the relative motions of C4-C6 vertebrae were calculated. Since FEBio defines the rotation of a rigid body in terms of quaternion angles, the relative Euler angles measured for each vertebral body were converted to their corresponding quaternion angles and imported into FEBio as load curves. The different loading configurations used in the model can be seen in Figure 4.5.

Three types of motion were simulated using the FE model: axial rotation to right and

left, lateral bending to right and left, and flexion-extension (three trials each). The first principal strains were recorded for all facet capsular ligaments in each trial and was taken to be an acceptable representative measure of model performance. Other metrics of strain may be more relevant to specific questions, but the first principal offered a reasonable and easily analyzed kinematic output from the model. Similarly, first principal stress was taken to be a representative stress metric even though other stresses may, in fact, be more important depending on the question to be answered. The full stress and strain tensors were calculated in the FEBio simulations; we restrict our discussion to the first principal strain and stress for brevity. Based on a mesh convergence study (see below), all computations were performed using quad4 meshes with an element size of approximately 0.3 mm. Similarly, based on the ligament-bone attachment area sensitivity study below, we chose a model in which four rows of elements (a band of $\sim$ 1.2 mm) were attached rigidly to the bone at the superior and inferior ends of each ligament, for all other simulations.

As described in the subsequent paragraphs, the model was used for a series of sensitivity studies to evaluate its performance and assess the importance of different factors in determining the results.

4.2.9 Sensitivity study: mesh convergence

A mesh convergence study was performed to ensure sufficient refinement of the model mesh. In this study, the facet capsular ligament on the left C4-C5 motion segment with element size of approximately 0.3 mm was used as the coarse mesh model (1421 elements). To generate the fine mesh model, each element of this ligament was divided to 4 elements using FEBio "Refine Mesh" algorithm. Both models were subjected to axial rotation, lateral bending, and flexion-extension motions and the results of the simulations were compared to determine the optimal mesh size for the rest of simulations.

4.2.10 Sensitivity study: ligament-bone attachment area

The exact region of ligament-bone attachment has not been defined in the literature and is not measurable from the CT scans. We therefore performed a sensitivity study on the effect that the location of this fixed boundary has on the simulated strain within the facet capsular ligament. For this study, we started with binding the first two rows of elements in the interior surface of the ligament to the superior vertebra (ligament-bone rigid attachment regions) while the rest of the elements were able to slide over the bone (sliding contact region). Then, we enlarged the attachment area in steps of one row of elements until the entire contact area between the ligament and the superior vertebra was represented as a rigid attachment.

4.2.11 Sensitivity study: material model

The facet capsule ligament is a fibrous connective tissue, comprised of two main regions: (1) a collagen-rich exterior region and, (2) an elastin-rich interior region [11, 12]. This unique, heterogeneous fiber structure allows the facet capsular ligament to undergo large stretches during the neck physiological motions. To investigate the effect of collagen fibers in the output stresses within the facet capsular ligament, we compared the first principal strains computed for the facet capsular ligaments with two different material models: (1) a solid mixture composed of a 3-orthogonal-fiber-family material model and a neo-Hookean ground matrix, and (2) a purely neo-Hookean material. The parameters for the fiber families and neo-Hookean ground matrix are defined earlier in "*Fiber structures and material properties for the facet capsular ligaments*" section.

4.2.12 Sensitivity study: subject-specific vs. generic geometry

In the present study, we developed an anatomy-detailed, subject-specific, CT-based FE model of lower cervical spine. To study the influence of geometric specificity on the output strain patterns within the facet capsular ligament, we compared the facet capsular ligament strain results to those obtained using an available generic geometrically symmetric bone model [60]. This open-access model was originally generated based on a 26-year-old female subject. After modifying the model to include only the C6-C7 motion segment, the vertebrae were transformed such that C7 vertebra of the generic model aligned with the C7 vertebra of the subject-specific model. The facet capsular ligament geometries were generated as defined earlier in the "*3D geometry of face capsular ligaments*" section to match the generic vertebral geometry. The same kinematics as the subject-specific model were applied to the generic model to move the bones. The boundary conditions on the ligaments were as in subject-specific model with similar ligament-bone rigid attachment to sliding contact regions ratios.

4.2.13 Sensitivity study: subject-specific vs. mismatched geometry and kinematics model

A basic requirement to generate a subject-specific model is a detailed knowledge of the bone kinematics that drive the model. The boundary conditions for this study were generated based on displacements extracted from a biplane videoradiography of axial rotation, lateral bending, and flexion-extension of participant's neck. To assess the effect of subject-specific kinematics, we paired the subject-specific geometry with the kinematics extracted for another healthy participant, otherwise following the same computational protocols as above.

4.3 RESULTS

4.3.1 Mesh convergence study

The left C4-C5 facet capsular ligament was chosen as a representative model for detailed analysis. Strain distribution maps of the left facet capsular ligament for both coarse and fine mesh model in axial rotation, lateral bending, and flexion-extension motions are shown in Figure 4.6. Head is in its ultimate position (AR to left, LB to left, flexion, and extension) in all of these representations. The small difference between the coarse and fine mesh results in Figure 4.6 indicates that the refinements of the coarse mesh is sufficient to generate accurate strain maps within the facet capsular ligament.

4.3.2 Sensitivity study: ligament-bone attachment area

The left C4-C5 facet capsular ligament was again as a representative model. The first principal strain within the ligament varied with rigid ligament-bone connection area (left to right in Figure 4.7). Three trials of maximum left axial rotation (AR1-3) and maximum flexion (FE1-3) are shown in Figure 4.7a and b, respectively. The first notable feature of the plot is that, despite having identical geometry and constitutive equation for their materials, different trials of the same motion resulted in different strain maps as is shown in Figure 4.7. The difference is most pronounced in the flexion models, where the kinematics of flexion varied between runs, leading to visible differences among rows FE1-3. In contrast, there was relatively little qualitative change along a given row, indicating that the regions of high and low strain are largely independent of attachment boundary condition, but the strains in the unattached regions increase (shift towards red) with greater attachment area (left to right).

The increase in the rigid ligament-bone attachment area resulted in slightly higher first principal strain values experienced by the remaining ligament's elements in all trials of

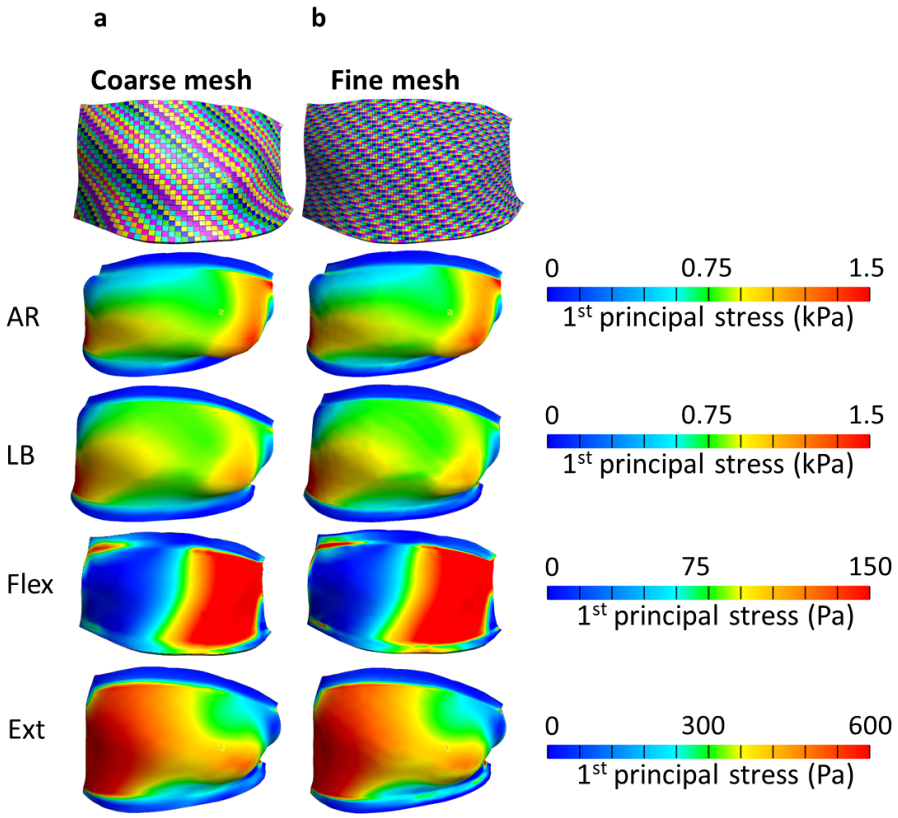

Figure 4.6: Mesh convergence study on the left C4-C5 facet capsular ligament. The exterior view of mesh visualization and stress distribution maps of the left C4C5 facet capsular ligament for (a) coarse mesh and (b) fine mesh models in axial rotation (AR) to left, lateral bending (LB) to left, flexion (Flex.) , and extension (Ext) motions.

the axial rotation and flexion-extension experiments. This observation is confirmed by the small upward trend in the first principal strain of the selected elements shown in Figure 4.8. When the rigid ligament-bone attachment constraint was imposed on all the facet capsular ligament elements in contact with bone – a nearly certain overestimate of the attachment area – the first principal strain in the free elements increased significantly. The first principal strain in the element marked E1 doubled when the all-elements-bonded model was implemented. The drop in the elements marked E2 and E3 in the same model is a result of being rigidly connected to the bone. Figure 4.8 also shows that the effect of an element's location on the first principal strain is more pronounced compared to the effect of

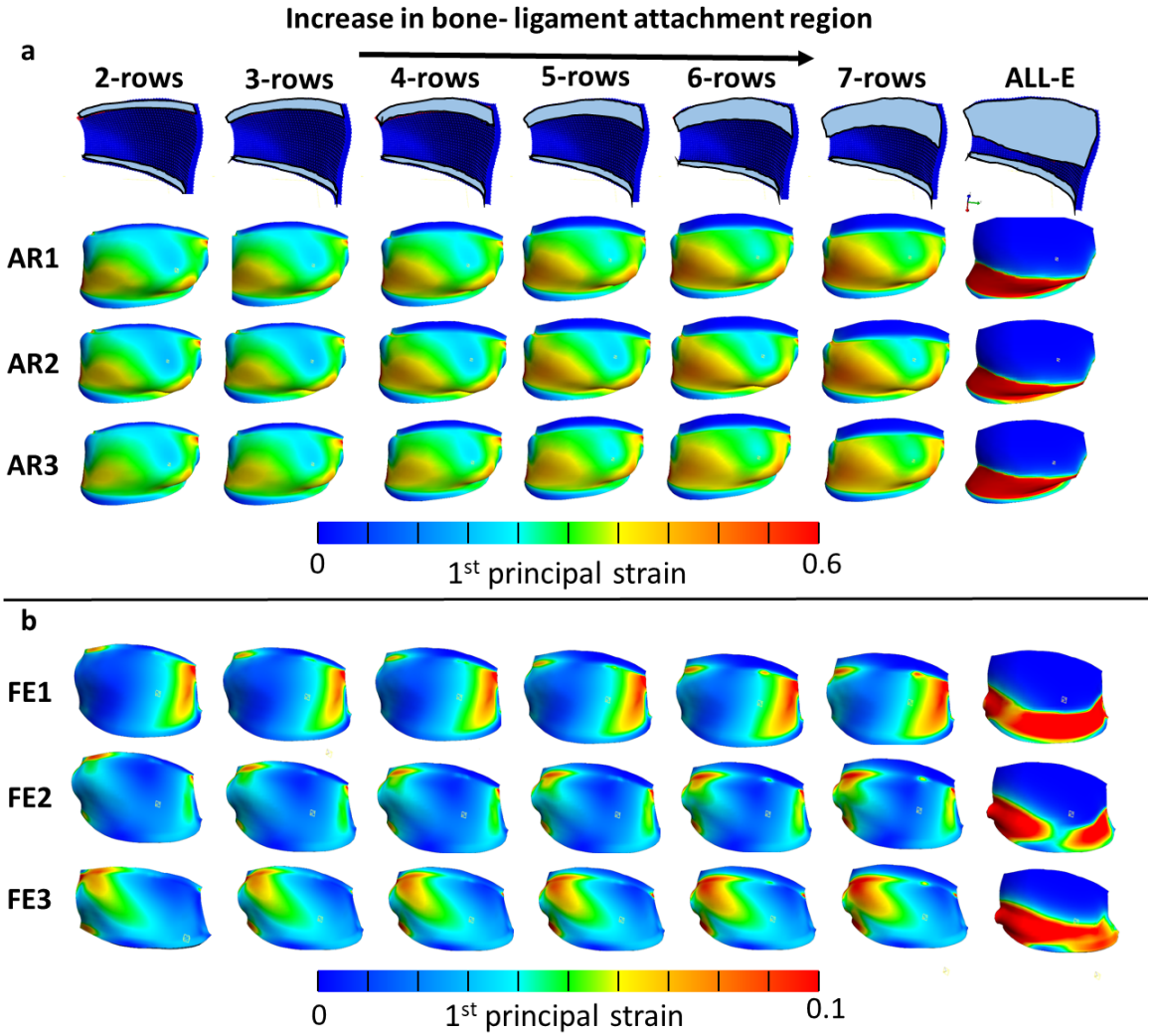

Figure 4.7: First principal strain distribution maps of the C4-C5 facet capsular ligament with different sizes of rigid ligament-bone connection regions. (a) Three trials of axial rotation (AR1-3) and (b) flexion-extension (FE1-3) motions.

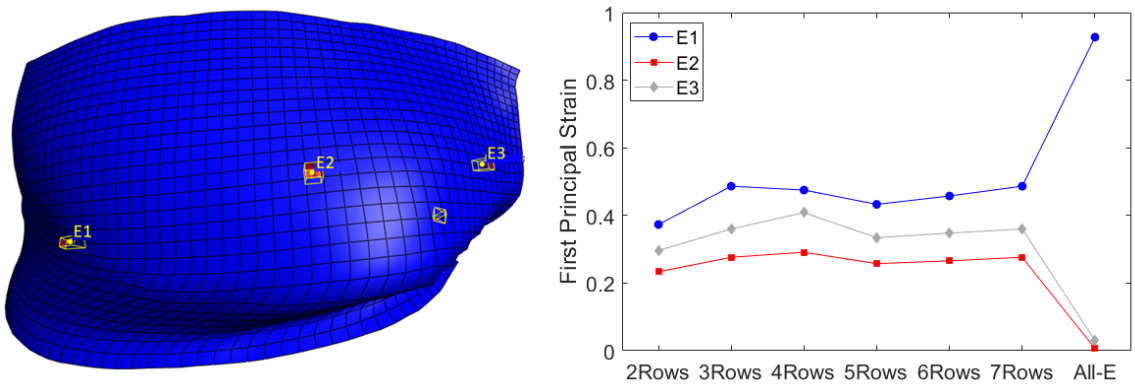

Figure 4.8: First principal strain vs. number of rows for selected elements (E1-E3) in the left, middle and right side of the left C4-C5 facet capsular ligament during axial rotation of the neck to the left. (Head is in its ultimate position).

the boundary condition for the more reasonable cases, as the strain increases by at least 60% moving from E1 to E3 compared to 32% increase in E1 strain between the models with the lowest and highest attachment areas.

4.3.3 FE simulations and data analysis

As a demonstration of application method, we generated a 3D, subject-specific FE models of a healthy 23-year-old female's cervical spine and simulated axial rotation (AR1-3), lateral bending (LB1-3), and flexion-extension (FE1-3) motions. The average of first principal strain within the right (dashed lines) and left (solid lines) C4 to C7 facet capsular ligaments is depicted in Figure 4.9a. Vertical dashed lines in this figure identify when the head was in its ultimate position in that motion. The strain values at the ultimate positions of Figure 4.9a were averaged over the three trials to produce an overall average first principal strain for each motion, shown in the bar graphs in Figure 4.9b. For example, the leftmost dark blue column of the "AR to Right" section of Figure 4.9b is the first principal strain on the C4C5 left facet capsular ligament averaged over the three corresponding trials (AR1, AR2, AR3) in Figure 4.9a at time point of 1.4 second (marked by a vertical dashed line

named “Right”). The axial rotation and lateral bending to left and flexion motions that are depicted in Figure 4.9b correspond to the latter incident (around 2.5 sec.) of the respective motions in Figure 4.9a.

As shown in Figure 4.9a, the right C4-C5 facet capsular ligament of this individual is more affected by the ipsilateral axial rotation motion (panels AR1-3), experiencing approximately twice as much strain as the rest of the ligaments experience on average in the same motion. A similar observation can be made for the right C6-C7 facet capsular ligament in flexion motion (panels FE1-3). As can be seen in Figure 4.9b, the results were, as expected, roughly symmetric between the right and left sides (e.g., the strains in the C5-C6 right and left facet capsular ligaments were high in axial rotation to right and left, respectively), but some differences were also observed (the first principal strain was noticeably higher on the right C6-C7 facet capsular ligament than the left in flexion even though flexion would be expected to produce symmetric facet capsular ligament stretches). Another asymmetry arose in lateral bending, with the strains generally higher for left than for right bending.

4.3.4 Sensitivity study: material model

Figure 4.10 illustrates the effects of the material model on the first principal strain and stress distributions within the left C4-C5 facet capsular ligament for different motions. For the case of axial rotation to left, the first principal strain in the hybrid and neo-Hookean (NH) material models are depicted in Figure 4.10a with the percent difference between the two (normalized to the strain and stress in the hybrid model) presented in Figure 4.10b. Similarly, for the axial rotation to left, the first principal stress in the two material models and their percent difference are presented in Figure 4.10c and Figure 4.10d. For all other motion types, the average first principal strain and stress for the two material models and the average percent differences for respective motions are depicted in Figure 4.10e through h. The strains and stresses in Figure 4.10e and g are averaged over the entire surface of

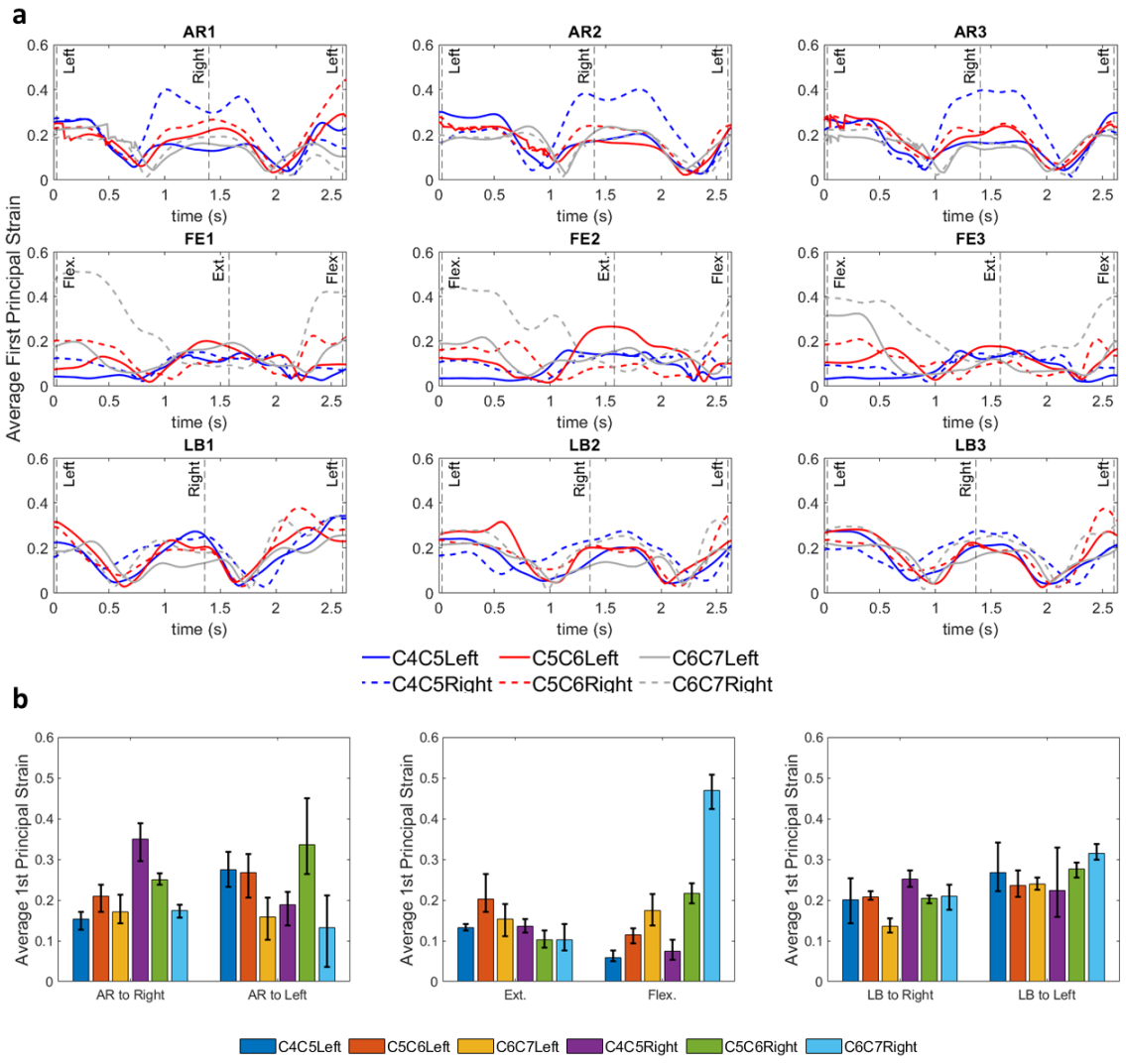

Figure 4.9: FE simulation results. (a) The average of first principal strain within the facet capsular ligaments of C4 to C7 spinal segments in a full head motion. (b) The average of average first principal strain values of part a over three different trials for each motion type and each facet capsular ligament at the time designated by the vertical dashed lines (Right, Left, Flex., and Ext.).

the C4-C5 facet capsular ligament first and then over three different trials with error bars indicating the max and min ligament-averaged values of different trials.

The first principal strain and stress distribution maps for hybrid and NH material models (shown in Figure 4.10a and c) are visually similar. Figure 4.10b and d show that 83% of elements defined by neo-Hookean materials have the first principal strain and stress values within $\pm 10\%$ of those in the respective element defined by hybrid material model. Figure 4.10e-h demonstrate that the normalized percent difference in the first principal strain resulting from a change in the material model is limited to less than 2% while this difference is more pronounced in the first principal stress by up to 10% as is shown in Figure 4.10g and h. The neo-Hookean material underestimates the first principal stress and overestimates the first principal strain for all motions except axial rotation to right.

4.3.5 Sensitivity study: subject-specific vs. generic geometry

The effect of geometry on the first principal strain within the right C6-C7 facet capsular ligament is shown in Figure 4.11. As is shown in Figure 4.11a, despite having an identical motion pattern as dictated by the kinematics, the generic geometric model consistently overpredicted the average first principal strain. The values in Figure 4.11b are the average values of ligament-averaged first principal strains over three different trials for each motion type at the time designated by the vertical dashed lines marked by Right, Left, Flex., and Ext. in the corresponding subfigure in Figure 4.11a. The difference in average strains is more pronounced in axial rotation (with 88% difference) and lateral bending to left (with 43% difference) compared to the respective motions to right (4% difference for axial rotation and 8% for lateral bending).

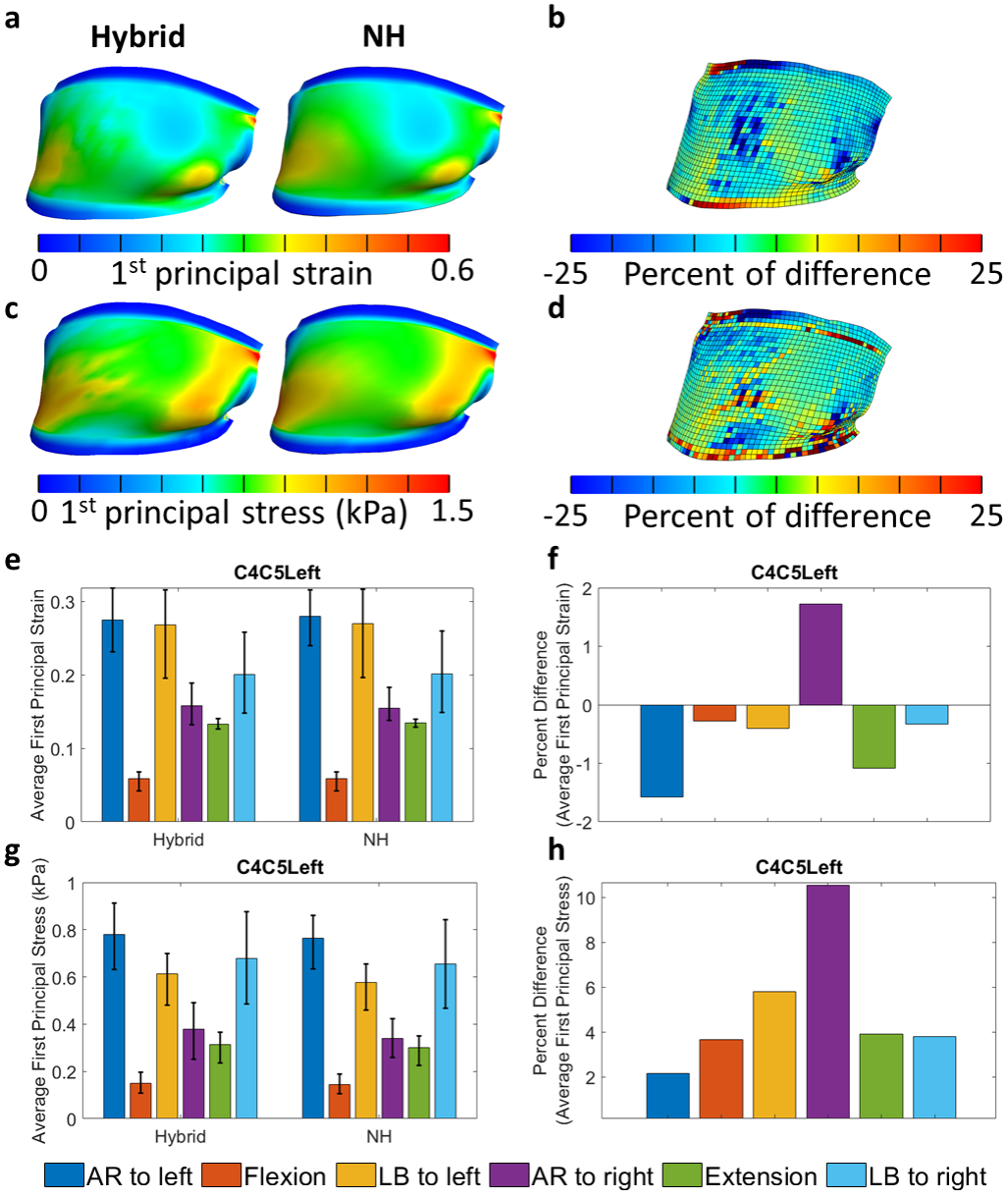

Figure 4.10: Effect of material on model results. (a) The first principal strain and (c) stress within the left C4-C5 facet capsular ligament in axial rotation for hybrid and neo-Hookean (NH) material model when the head is in ultimate position to left. The percent difference of (b) the first principal strain and (d) first principal stress between the hybrid and neo-Hookean (NH) material model shown in part a and c, respectively. Average first principal (e) strain and (g) stress within the left C4-C5 facet capsular ligament in different motions for hybrid and neo-Hookean (NH) material model. The percent of difference of the (f) first principal strain and (h) between the hybrid and neo-Hookean (NH) material model shown in part e and g, respectively.

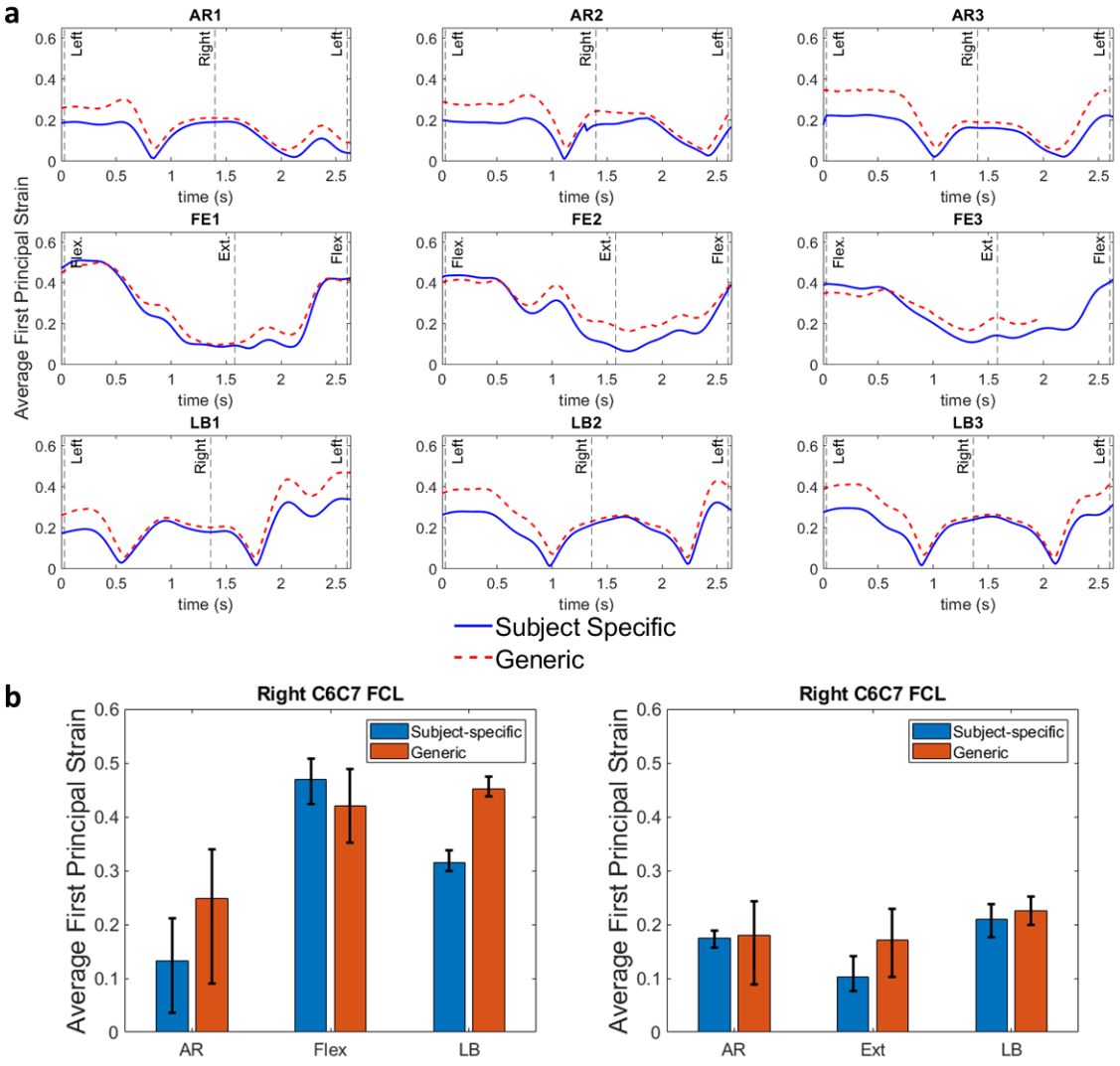

Figure 4.11: Effect of geometry on model results. (a) The average of first principal strain in range of 2.5 seconds head motion within the right C6-C7 facet capsular ligament for axial rotation (AR1-3), flexion-extension (FE1-3), and lateral bending (LB1-3) for a symmetric generic geometry and the subject-specific model. (b) The average values of ligament-averaged first principal strains over three different trials for each motion type at the time designated by the vertical dashed lines marked by Right, Left, Flex., and Ext. (* The axial rotation and lateral bending to left and flexion motions that are depicted in part b correspond to the latter incident (around 2.5 sec.) of the respective motions on part a. ** Error bars in this figure represent the range of strain across three trials for each motion).

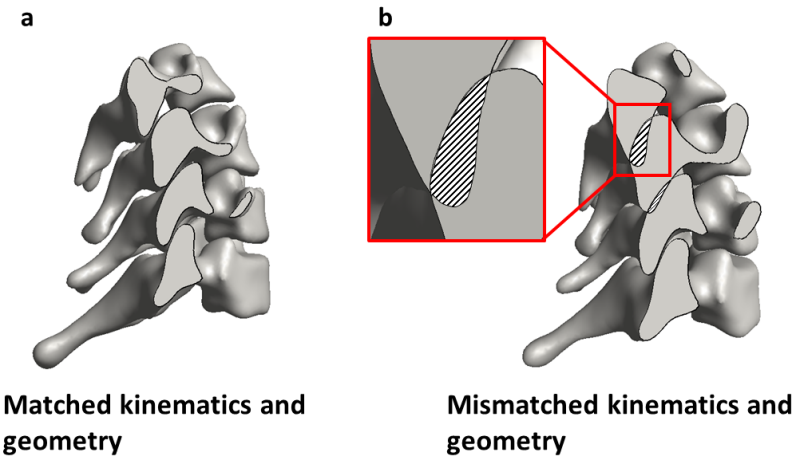

Figure 4.12: Effect of kinematics on model results. (a) When the geometry and kinematics from the same subject are used, there is no overlap between the vertebrae during extension. (b) When the geometry of one subject is used with the kinematics of another, the inconsistency leads to overlap between the vertebrae during extension. This impossible situation demonstrates the importance of subject-specific kinematics and anatomy.

4.3.6 Sensitivity study: subject-specific vs. generic kinematics

Figure 4.12 illustrates the importance of using the subject-specific kinematics for the model. As shown in Fig 12a, when the anatomy and kinematics are matched, the vertebrae remain distinct from each other. In contrast (Figure 4.12b) when a mismatched set of geometry and kinematics is used, the model fails during extension because the vertebral body of C4 intersects that of C5, a physical impossibility.

4.4 Discussion

In this study, we demonstrated a method to generate a kinematically driven, geometrically accurate, FE model of the facet capsular ligaments of the lower cervical spine. The model takes as input realistic vertebral anatomy (from CT) and kinematics (from biplane videoradiography). Although the methodology employed herein was applied only to C4-C7, it could in principle be applied to any range within the spine or to other joints if the nec-

essary data and a reasonable estimate of the ligament location were available. The major conclusions from this study, discussed in more detail in subsequent paragraphs, are:

1. the choice of constitutive equation in the model has relatively little effect on the calculated ligament strain field but has a stronger effect on the calculated stress field,

2. the attachment area between the ligament and the bone must be estimated, but the sensitivity to that estimate is relatively small over a wide range of possible areas,

3. subject-specific vertebral anatomy and kinematics are both important in estimating the strain in the facet capsular ligament, and

4. there is substantial asymmetry in the strains between the left and right side, at least for the individual studied.

Two types of constitutive material models (an isotropic neo-Hookean model and a heterogeneous hybrid microstructural-continuum multiscale model) were used to estimate the biomechanics of the facet capsular ligaments during different physiological motions. The neo-Hookean model was able to accurately estimate the average of the strain and stress values over the tissue (Figure 4.10e-h); however, it was shown that a structure-based material model is needed to obtain the detailed local information for each element (Figure 4.10a-d). Because subject-specific structural information is not obtainable *in vivo*, this result points to a limitation of the proposed approach: the ability to describe detailed, small-scale behavior of the tissue is limited by our ability to describe its small-scale material properties. For instance, to study the effect of the macroscopic loading mechanisms on the local microscopic structural deformation surrounding a neuron in the ligament, a detailed structure-based multiscale model would be needed and would not, with current technology, be available on a subject-specific basis. If, however, the overall average strain in the ligament in different physiological motion is one's objective, then a simple neo-Hookean model could generate an acceptable estimate of strain values.

It is still unclear exactly where the rigid ligament-bone attachment ends in a native tissue, and the ligament-bone attachment area may change as humans age and the facet capsular ligament degenerates because bone growth, calcification of the ligament, and osteophyte formation are common during aging and in disease states such as osteoarthritis [169–171]. This bone growth may restrict ligament function, segmental mobility, and eventually lead to boney fusion of the facet joints [8, 169]. Our sensitivity study on attachment area showed that by increasing the rigid ligament-bone connection areas, mildly higher first principal strain values are experienced by the remaining ligament's elements until the entire ligament is attached to the bone.

Perhaps one of the most important outcomes of this study was to provide a tool that can be used to help us gain insights on how unique anatomy of each individual, in combination with that individual's specific kinematics, dominates the biomechanics of the cervical spine and its facet capsular ligaments. For instance, the extremely higher strain average on the right C6-C7 facet capsular ligament in comparison to the facet capsular ligament on the left side of this motion segment in subject-specific model (Figure 4.9b) can be attributed primarily to kinematic effects rather than geometry, since, despite having a perfectly symmetric geometry, the same effect has been observed in the generic geometry model (Figure 4.11b). The fact that different trials of the same motion resulted in different strain maps over the tissue (Figure 4.7), emphasizes the effects that subject-specific kinematic differences have on the biomechanics of the model since the anatomy is obviously unchanged between trials. Finally, as the result of Figure 4.12 suggests, the subject-specific geometry and kinematics are intertwined with each other, and having one without the other in a model may result in a physically impossible model.

To summarize, the current study provides a methodology to create a subject-specific model of the cervical facet capsular ligaments (C4-C7) and can investigate various clinical questions by coupling experimental kinematics with multiscale computational models.

Extension to other locations and ligaments would be possible if appropriate information could be obtained. Finally, we note that the primary purpose of this study was to explore the method and not to perform a scientific study of spinal motion. Only one subject was examined, and while the data from that subject allowed us to probe our modeling scheme's capabilities and to identify the potential importance of subject-specific effects, one should not attempt to extrapolate from those results to the population at large.

CHAPTER 5

Conclusions and Future Directions

Let us choose for ourselves

our path in life.

Emilie du Chatelet

5.1 SUMMARY

The research presented in this dissertation uses computational modeling to introduce a methodology of creating a hybrid microstructural-continuum, 3D, subject-specific model of the lower cervical spine. This model can demonstrates the importance of subject-specificity on the tissue-level mechanical response of the cervical facet capsular ligament during flexion-extension, axial rotation, and lateral bending. As the first step towards this new modeling framework, I developed a structure-based continuum computational platform that uses the structural information of the macroscopically and/or microscopically heterogeneous tissues, such as facet capsular ligament, in a continuum-based finite element modeling and reduces the computational costs dramatically relative to discrete-fiber network multiscale models (Chapter 2). Next, I modified existing fiber-axon models to explore the effect of macroscopic strain rates, spanning a relevant range of values, on the viscoelastic micromechanical environment of an embedded neuron in reconstituted collagen gel (lower collagen concentration) and ex vivo tissue (higher collagen concentration) models (Chapter 3). Finally, anatomical and kinematic data of a 23-year-old participant, in combination with structural information from cadaveric facet capsular ligaments, were used to construct a hybrid microstructural-continuum subject-specific finite element model of the lower cervical spine as it undergoes various spinal motions, such as flexion-extension, lateral bending, axial rotation (Chapter 4).

5.2 IMPACT

The research studies described here have used different computational methods to introduce new techniques or expand the current knowledge in several aspects:

1. The hybrid microstructural-continuum multiscale approach (Chapter 2) can convert the structural information of a collagenous tissue (such as facet capsular ligament) to an affine constitutive material model (such as the Holzapfel-Gasser-Ogden (HGO) model). This constitutive material model, then, can be used in commercial finite element platforms and can leverage the speed of classical continuum-based finite element modeling. In a test problem, the hybrid method matched the fully-coupled multiscale results to within 0.062 MPa and 4.12% RMS error for the maximum shear stress and strain, respectively, while required only 0.05% of the CPU-hr.

2. In the viscoelasticity study (Chapter 3), we focused on the fundamental differences (such as stiffness, viscoelastic relaxation, and collagen density) between the co-cultured axon-gel models and the facet capsular ligament and showed that these differences become important when interpreting the gel experiments vs. tissue experiments. For instance, we showed that the strains experienced by an axon embedded in a collagen gel are likely lower than those that would arise in native tissue under the same loading conditions. The viscoelastic simulations of this study showed that differences in gel stiffness are important to consider at all loading rates, and that gel viscoelasticity leads to differences, especially, for macroscopic strain rates in the 0.01-7 %/s range.

3. Lastly, we demonstrated a method to generate a kinematically driven, geometrically accurate, hybrid multiscale FE model of the facet capsular ligaments of the lower cervical spine (Chapter 4). The conducted methodology highlights the importance

of subject-specificity in generating human cervical facet capsular ligament models and provides a paradigm for development of subject-specific models that can serve as decision support technologies in diagnosis and treatment of cervical injuries. One instance of the significance of subject specificity in cervical motion simulations is the finding that subject-specific kinematics plays a critical role in accurate characterization of strain as evidenced by the left-right asymmetry in strain results during flexion motion in both asymmetric subject-specific and symmetric generic geometry models once both models incorporate subject-specific kinematics.

5.3 Future Direction

The research conducted in this thesis introduced a step-by-step method to create a hybrid multiscale 3D subject-specific model of lower cervical spine and was used to characterize the mechanical properties of the cervical facet capsular ligament in a healthy 23-year-old subject. This methodology has the potential to be modified and used in different directions.

The first and the most obvious next stage for this study is to obtain more subject-specific kinematics and CT scans of the human cervical spine with different facet joint health conditions and use the new methods to generate more subject-specific models. These models can be used to explore how different aspects of the specificity such as anatomy, kinematics, and degree of the facet joints' degeneration contribute to the distribution of loads in the facet capsular ligament. Similar methodology can also be utilized to generate models of other spinal levels such as thoracic and lumbar motion segments, as well as other spinal ligaments.

In the hybrid model, the transition between the microstructural and the continuum level was incorporated by estimating the structural parameters for a 3-fiber-family model. Different constitutive models may represent specific aspects of behavior more accurately and

therefore be better suited for future investigations. Fortunately, the current research constructs the model in a modular format which makes such future adjustments straightforward.

Due to the low-speed nature of the physiological neck motions in daily activities, all the components, including the collagen structures that were used to estimate material properties of the facet capsular ligaments, were modeled as nonlinear elastic material models. This model, however, can be modified to incorporate viscoelastic material models, such as the ones that have been used in Chapter 3 of this dissertation. Such a viscoelastic subject-specific model, then, can be used to study the pathophysiological states due to the incidents involving higher rates of motions such as certain sports- or trauma-associated injuries.

Bibliography

[1] S. Safiri *et al.*, "Global, regional, and national burden of neck pain in the general population, 1990-2017: systematic analysis of the Global Burden of Disease Study 2017," *BMJ (Clinical research ed.)*, vol. 368, Mar. 2020. [Online]. Available: https://pubmed.ncbi.nlm.nih.gov/32217608/.

[2] G. B. Andersson, "Epidemiological features of chronic low-back pain," *The Lancet*, vol. 354, no. 9178, pp. 581–585, Aug. 1999. [Online]. Available: https://linkinghub.elsevier.com/retrieve/pii/S0140673699013124.

[3] S. A. O'Leary *et al.*, "Facet Joints of the Spine: Structure–Function Relationships, Problems and Treatments, and the Potential for Regeneration," *Annual Review of Biomedical Engineering*, vol. 20, no. 1, pp. 145–170, 2018.

[4] J. D. Childs *et al.*, "Neck Pain: Clinical Practice Guidelines Linked to the International Classification of Functioning, Disability, and Health From the Orthopaedic Section of the American Physical Therapy Association," *Journal of Orthopaedic & Sports Physical Therapy*, vol. 38, no. 9, A1–A34, Sep. 2008. [Online]. Available: https://www.jospt.org/doi/abs/10.2519/jospt.2008.0303%20http://www.jospt.org/doi/10.2519/jospt.2008.0303.

[5] D. Steilen *et al.*, "Chronic Neck Pain: Making the Connection Between Capsular Ligament Laxity and Cervical Instability," *The Open Orthopaedics Journal*, vol. 8, no. 1, pp. 326–345, Oct. 2014. [Online]. Available: /pmc/articles/PMC4200875/%20/pmc/articles/PMC4200875/?report=abstract%20https://www.ncbi.nlm.nih.gov/pmc/articles/PMC4200875/%20https://openorthopaedicsjournal.com/VOLUME/8/PAGE/326/.

[6] A. Fujiwara *et al.*, "The relationship between facet joint osteoarthritis and disc degeneration of the lumbar spine: an MRI study," *European Spine Journal*, vol. 8, no. 5, pp. 396–401, Oct. 1999. [Online]. Available: http://link.springer.com/10.1007/s005860050193.

[7] L. H. Yahia and S. Garzon, "Structure on the capsular ligaments of the facet joints," *Annals of Anatomy*, vol. 175, no. 2, pp. 185–188, 1993.

[8] N. V. Jaumard, W. C. Welch, and B. A. Winkelstein, "Spinal Facet Joint Biomechanics and Mechanotransduction in Normal, Injury and Degenerative Conditions," *Journal of Biomechanical Engineering*, vol. 133, no. 7, p. 071 010, 2011. [Online]. Available: http://biomechanical.asmedigitalcollection.asme.org/article.aspx?articleid=1430256.

[9] R. Izzo *et al.*, *Biomechanics of the spine. Part I: Spinal stability*, Jan. 2013.

[10] E. A. Bermel, V. H. Barocas, and A. M. Ellingson, "The role of the facet capsular ligament in providing spinal stability," *Computer Methods in Biomechanics and Biomedical Engineering*, vol. 21, no. 13, pp. 712–721, 2018. [Online]. Available: https://doi.org/10.1080/10255842.2018.1514392.

[11] J. S. Little and P. S. Khalsa, "Material Properties of the Human Lumbar Facet Joint Capsule," *Journal of Biomechanical Engineering*, vol. 127, no. 1, pp. 15–24, Feb. 2005. [Online]. Available: https://asmedigitalcollection.asme.org/biomechanical/article/127/1/15/445137/Material-Properties-of-the-Human-Lumbar-Facet.

[12] T. Yamashita *et al.*, *A morphological study of the fibrous capsule of the human lumbar facet joint*, 1996.

[13] S. Kallakuri, "Innervation of cervical ventral facet joint capsule: Histological evidence," *World Journal of Orthopedics*, vol. 3, no. 2, p. 10, 2012. [Online]. Available: /pmc/articles/PMC3302050/%20/pmc/articles/PMC3302050/?report=abstract%20https://www.ncbi.nlm.nih.gov/pmc/articles/PMC3302050/%20http://www.wjgnet.com/2218-5836/full/v3/i2/10.htm.

[14] S. Zhang *et al.*, "Tissue Strain Reorganizes Collagen With a Switchlike Response That Regulates Neuronal Extracellular Signal-Regulated Kinase Phosphorylation In Vitro: Implications for Ligamentous Injury and Mechanotransduction," *Journal of Biomechanical Engineering*, vol. 138, no. 2, p. 0 210 131, Feb. 2016. [Online]. Available: https://asmedigitalcollection.asme.org/biomechanical/article/doi/10.1115/1.4031975/371478/Tissue-Strain-Reorganizes-Collagen-With-a.

[15] M. Solomonow, "Ligaments: a source of work-related musculoskeletal disorders," *Journal of Electromyography and Kinesiology*, vol. 14, no. 1, pp. 49–60, Feb. 2004. [Online]. Available: https://linkinghub.elsevier.com/retrieve/pii/S1050641103001317.

[16] D. Vader *et al.*, "Strain-Induced Alignment in Collagen Gels," *PLOS ONE*, vol. 4, no. 6, e5902, Jun. 2009. [Online]. Available: https://journals.plos.org/plosone/article?id=10.1371/journal.pone.0005902.

[17] Y. Lu *et al.*, "Development of an in vivo method to investigate biomechanical and neurophysiological properties of spine facet joint capsules," *European Spine Journal*, vol. 14, no. 6, pp. 565–572, Aug. 2005. [Online]. Available: https://link.springer.com/article/10.1007/s00586-004-0835-9.

[18] L. Dong and B. A. Winkelstein, "Simulated Whiplash Modulates Expression of the Glutamatergic System in the Spinal Cord Suggesting Spinal Plasticity Is Associated with Painful Dynamic Cervical Facet Loading," *Journal of Neurotrauma*, vol. 27, no. 1, p. 163, Jan. 2010. [Online]. Available: /pmc/articles/PMC2824231/%20/pmc/articles/PMC2824231/?report=abstract%20https://www.ncbi.nlm.nih.gov/pmc/articles/PMC2824231/.

[19] C. Chen *et al.*, "Distribution of A-δ and C-Fiber Receptors in the Cervical Facet Joint Capsule and Their Response to Stretch," *The Journal of Bone & Joint Surgery*, vol. 88, no. 8, pp. 1807–1816, Aug. 2006. [Online]. Available: http://journals.lww.com/00004623-200608000-00018.

[20] J. S. Little and P. S. Khalsa, "Human Lumbar Spine Creep during Cyclic and Static Flexion: Creep Rate, Biomechanics, and Facet Joint Capsule Strain," *Annals of Biomedical Engineering*, vol. 33, no. 3, pp. 391–401, Jan. 2005. [Online]. Available: http://link.springer.com/10.1007/s10439-005-1742-x.

[21] K. King *et al.*, "High magnitude cyclic load triggers inflammatory response in lumbar ligaments," *Clinical Biomechanics*, vol. 24, no. 10, pp. 792–798, Dec. 2009. [Online]. Available: https://linkinghub.elsevier.com/retrieve/pii/S0268003309001727.

[22] S. Kartha *et al.*, "Repeated High Rate Facet Capsular Stretch at Strains That are Below the Pain Threshold Induces Pain and Spinal Inflammation With Decreased Ligament Strength in the Rat," *Journal of Biomechanical Engineering*, vol. 140, no. 8, Aug. 2018. [Online]. Available: http://asmedigitalcollection.asme.org/biomechanical/article-pdf/140/8/081002/6414238/bio_140_08_081002.pdf%20https://asmedigitalcollection.asme.org/biomechanical/article/doi/10.1115/1.4040023/424445/Repeated-High-Rate-Facet-Capsular-Stretch-at.

[23] L. Dong *et al.*, "Whiplash-like facet joint loading initiates glutamatergic responses in the DRG and spinal cord associated with behavioral hypersensitivity," *Brain Research*, vol. 1461, pp. 51–63, Jun. 2012. [Online]. Available: https://linkinghub.elsevier.com/retrieve/pii/S0006899312007196.

[24] K. P. Quinn *et al.*, "Structural changes in the cervical facet capsular ligament: potential contributions to pain following subfailure loading.," *Stapp car crash journal*, vol. 51, pp. 169–87, Oct. 2007. [Online]. Available: http://repository.upenn.edu/be_papersPublisherURL: http://www.sae.org/technical/books/P-401http://repository.upenn.edu/be_papers/105%20http://www.ncbi.nlm.nih.gov/pubmed/18278597.

[25] P. C. Ivancic *et al.*, "Whiplash causes increased laxity of cervical capsular ligament," *Clinical biomechanics (Bristol, Avon)*, vol. 23, no. 2, p. 159, Feb. 2008. [Online]. Available: /pmc/articles/PMC2701103/%20/pmc/articles/PMC2701103/?report=abstract%20https://www.ncbi.nlm.nih.gov/pmc/articles/PMC2701103/.

[26] K. E. Lee *et al.*, "Tensile cervical facet capsule ligament mechanics: Failure and subfailure responses in the rat," *Journal of Biomechanics*, vol. 39, no. 7, pp. 1256–1264, Jan. 2006. [Online]. Available: https://linkinghub.elsevier.com/retrieve/pii/S0021929005001491.

[27] K. P. Quinn and B. A. Winkelstein, "Detection of Altered Collagen Fiber Alignment in the Cervical Facet Capsule After Whiplash-Like Joint Retraction," *Annals of Biomedical Engineering 2011 39:8*, vol. 39, no. 8, pp. 2163–2173, May 2011. [Online]. Available: https://link.springer.com/article/10.1007/s10439-011-0316-3.

[28] J. J. CRISCO *et al.*, "Transections of the C1-C2 Joint Capsular Ligaments in the Cadaveric Spine," *Spine*, vol. 16, S474–S479, Oct. 1991. [Online]. Available: http://journals.lww.com/00007632-199110001-00003.

[29] M. M. Panjabi *et al.*, *Capsular ligament stretches during in vitro whiplash simulations*, 1998.

[30] K. L. Troyer and C. M. Puttlitz, "Human cervical spine ligaments exhibit fully nonlinear viscoelastic behavior," *Acta Biomaterialia*, vol. 7, no. 2, pp. 700–709, Feb. 2011. [Online]. Available: https://linkinghub.elsevier.com/retrieve/pii/S1742706110004046.

[31] S. Zhang, D. S. Bassett, and B. A. Winkelstein, "Stretch-induced network reconfiguration of collagen fibres in the human facet capsular ligament," *Journal of The Royal Society Interface*, vol. 13, no. 114, p. 20 150 883, Jan. 2016. [Online]. Available: https://royalsocietypublishing.org/doi/10.1098/rsif.2015.0883.

[32] S. Zhang, E. Zhao, and B. A. Winkelstein, "A Nociceptive Role for Integrin Signaling in Pain After Mechanical Injury to the Spinal Facet Capsular Ligament," *Annals of Biomedical Engineering*, vol. 45, no. 12, pp. 2813–2825, Dec. 2017. [Online]. Available: https://link.springer.com/article/10.1007/s10439-017-1917-2.

[33] S. Zhang, S. Singh, and B. A. Winkelstein, "Collagen organization regulates stretch-initiated pain-related neuronal signals in vitro: Implications for structure-function relationships in innervated ligaments," *Journal of orthopaedic research : official publication of the Orthopaedic Research Society*, vol. 36, no. 2, p. 770, Feb. 2018. [Online]. Available: /pmc/articles/PMC5775066/%20/pmc/articles/PMC5775066/?report=abstract%20https://www.ncbi.nlm.nih.gov/pmc/articles/PMC5775066/.

[34] M. E. Ita and B. A. Winkelstein, "Concentration-Dependent Effects of Fibroblast-Like Synoviocytes on Collagen Gel Multiscale Biomechanics and Neuronal Signaling: Implications for Modeling Human Ligamentous Tissues," *Journal of Biomechanical Engineering*, vol. 141, no. 9, Sep. 2019. [Online]. Available: http://asmedigitalcollection.asme.org/biomechanical/article-pdf/141/9/091013/6423910/bio_141_09_091013.pdf.

[35] D. K. Cullen, M. C. Lessing, and M. C. Laplaca, "Collagen-dependent neurite outgrowth and response to dynamic deformation in three-dimensional neuronal cultures," *Annals of Biomedical Engineering*, vol. 35, no. 5, pp. 835–846, May 2007. [Online]. Available: https://link.springer.com/article/10.1007/s10439-007-9292-z.

[36] R. K. Willits and S. L. Skornia, "Effect of collagen gel stiffness on neurite extension," *Journal of Biomaterials Science, Polymer Edition*, vol. 15, no. 12, pp. 1521–1531, Jan. 2004. [Online]. Available: https://www.tandfonline.com/doi/abs/10.1163/1568562042459698%20https://www.tandfonline.com/doi/full/10.1163/1568562042459698.

[37] S. Zhang *et al.*, "Multiscale mechanics of the cervical facet capsular ligament, with particular emphasis on anomalous fiber realignment prior to tissue failure," *Biomechanics and Modeling in Mechanobiology*, vol. 17, no. 1, pp. 133–145, 2018.

[38] H. Wang *et al.*, "Effects of facet joint degeneration on stress alterations in cervical spine C5–C6: A finite element analysis," *Mathematical Biosciences and Engineering*, vol. 16, no. 6, pp. 7447–7457, 2019. [Online]. Available: http://www.aimspress.com/journal/MBE%20http://www.aimspress.com/article/10.3934/mbe.2019373.

[39] S. F. Mattucci *et al.*, "Strain rate dependent properties of younger human cervical spine ligaments," *Journal of the Mechanical Behavior of Biomedical Materials*, vol. 10, pp. 216–226, Jun. 2012. [Online]. Available: https://linkinghub.elsevier.com/retrieve/pii/S1751616112000537.

[40] N. Yoganandan *et al.*, "Finite element applications in human cervical spine modeling," *Spine*, vol. 21, no. 15, pp. 1824–1834, Aug. 1996. [Online]. Available: https://pubmed.ncbi.nlm.nih.gov/8855470/.

[41] N. Yoganandan, S. Kumaresan, and F. A. Pintar, "Geometric and mechanical properties of human cervical spine ligaments," *Journal of Biomechanical Engineering*, vol. 122, no. 6, pp. 623–629, 2000.

[42] V. Zarei *et al.*, "Image-based multiscale mechanical modeling shows the importance of structural heterogeneity in the human lumbar facet capsular ligament," *Biomechanics and Modeling in Mechanobiology*, vol. 16, no. 4, pp. 1425–1438, Aug. 2017. [Online]. Available: http://link.springer.com/10.1007/s10237-017-0896-4.

[43] E. Ban *et al.*, "Collagen Organization in Facet Capsular Ligaments Varies With Spinal Region and With Ligament Deformation," *Journal of Biomechanical Engineering*, vol. 139, no. 7, Jul. 2017. [Online]. Available: https://asmedigitalcollection.asme.org/biomechanical/article/doi/10.1115/1.4036019/371345/Collagen-Organization-in-Facet-Capsular-Ligaments.

[44] K. P. Quinn and B. A. Winkelstein, "Vector correlation technique for pixel-wise detection of collagen fiber realignment during injurious tensile loading," *Journal of Biomedical Optics*, vol. 14, no. 5, p. 054 010, 2009. [Online]. Available: http://biomedicaloptics.spiedigitallibrary.org/article.aspx?doi=10.1117/1.3227037.

[45] ——, "Altered collagen fiber kinematics define the onset of localized ligament damage during loading," *Journal of Applied Physiology*, vol. 105, no. 6, pp. 1881–1888, 2008.

[46] S. P. Lake and V. H. Barocas, "Mechanics and kinematics of soft tissue under indentation are determined by the degree of initial collagen fiber alignment," *Journal of the Mechanical Behavior of Biomedical Materials*, vol. 13, pp. 25–35, Sep. 2012. [Online]. Available: https://linkinghub.elsevier.com/retrieve/pii/S1751616112001063.

[47] T. Stylianopoulos and V. H. Barocas, "Volume-averaging theory for the study of the mechanics of collagen networks," [Online]. Available: www.elsevier.com/locate/cma.

[48] P. L. Chandran and V. H. Barocas, "Deterministic material-based averaging theory model of collagen gel micromechanics," *Journal of Biomechanical Engineering*, vol. 129, no. 2, pp. 137–147, 2007.

[49] V. Zarei *et al.*, "Multiscale modelling of the human lumbar facet capsular ligament: analysing spinal motion from the joint to the neurons," *Journal of The Royal Society Interface*, vol. 15, no. 148, p. 20 180 550, Nov. 2018. [Online]. Available: https://royalsocietypublishing.org/doi/10.1098/rsif.2018.0550.

[50] G. A. Holzapfel, T. C. Gasser, and R. W. Ogden, "A New Constitutive Framework for Arterial Wall Mechanics and a Comparative Study of Material Models," *Journal of Elasticity*, vol. 61, pp. 1–48, 2000.

[51] D. H. E. Yoon *et al.*, "Rapid determination of internal strains in soft tissues using an experimentally calibrated finite element model derived from magnetic resonance imaging," *Quantitative Imaging in Medicine and Surgery*, vol. 10, no. 1, pp. 57–65, Jan. 2020. [Online]. Available: http://dx.doi.org/10.21037/qims.2019.10.16%20http://qims.amegroups.com/article/view/31495/27318.

[52] A. M. Ellingson *et al.*, "Comparative role of disc degeneration and ligament failure on functional mechanics of the lumbar spine," *Computer Methods in Biomechanics and Biomedical Engineering*, vol. 19, no. 9, pp. 1009–1018, 2015.

[53] M. R. Herron *et al.*, "Febio finite element models of the human cervical spine," *Journal of Biomechanics*, vol. 113, p. 110 077, Dec. 2020. [Online]. Available: https://linkinghub.elsevier.com/retrieve/pii/S0021929020305017.

[54] K. Brolin and P. Halldin, "Development of a Finite Element Model of the Upper Cervical Spine and a Parameter Study of Ligament Characteristics," *Spine*, vol. 29, no. 4, pp. 376–385, 2004.

[55] Y. H. Kim, B. Khuyagbaatar, and K. Kim, "Recent advances in finite element modeling of the human cervical spine," *Journal of Mechanical Science and Technology*, vol. 32, no. 1, pp. 1–10, Jan. 2018. [Online]. Available: https://link.springer.com/article/10.1007/s12206-017-1201-2%20http://link.springer.com/10.1007/s12206-017-1201-2.

[56] N. Nishida *et al.*, "Soft Tissue Injury in Cervical Spine Is a Risk Factor for Intersegmental Instability: A Finite Element Analysis," *World Neurosurgery*, May 2022. [Online]. Available: https://linkinghub.elsevier.com/retrieve/pii/S1878875022005654.

[57] P. S. Manickam and S. Roy, "The biomechanical study of cervical spine: A Finite Element Analysis," *The International Journal of Artificial Organs*, vol. 45, no. 1, pp. 89–95, Jan. 2022. [Online]. Available: https://journals.sagepub.com/doi/full/10.1177/0391398821995495%20http://journals.sagepub.com/doi/10.1177/0391398821995495.

[58] N. Kallemeyn *et al.*, "Validation of a C2–C7 cervical spine finite element model using specimen-specific flexibility data," *Medical Engineering & Physics*, vol. 32, no. 5, pp. 482–489, Jun. 2010. [Online]. Available: http://dx.doi.org/10.1016/j.medengphy.2010.03.001%20https://linkinghub.elsevier.com/retrieve/pii/S1350453310000524.

[59] J. A. Wheeldon *et al.*, "Validation of a finite element model of the young normal lower cervical spine," *Annals of Biomedical Engineering*, vol. 36, no. 9, pp. 1458–1469, 2008.

[60] J. Östh *et al.*, "A Female Ligamentous Cervical Spine Finite Element Model Validated for Physiological Loads," *Journal of Biomechanical Engineering*, vol. 138, no. 6, 2016.

[61] T. Mustafy *et al.*, "Investigation of impact loading rate effects on the ligamentous cervical spinal load-partitioning using finite element model of functional spinal unit C2–C3," *Journal of Biomechanics*, vol. 47, no. 12, pp. 2891–2903, Sep. 2014. [Online]. Available: https://linkinghub.elsevier.com/retrieve/pii/S0021929014003972.

[62] A. P. del Palomar, B. Calvo, and M. Doblaré, "An accurate finite element model of the cervical spine under quasi-static loading," *Journal of Biomechanics*, vol. 41, no. 3, pp. 523–531, Jan. 2008. [Online]. Available: https://linkinghub.elsevier.com/retrieve/pii/S0021929007004605.

[63] T. L. Bredbenner *et al.*, "Development and validation of a statistical shape modeling-based finite element model of the cervical spine under low-level multiple direction loading conditions," *Frontiers in Bioengineering and Biotechnology*, vol. 2, no. NOV, p. 58, 2014.

[64] M. Nikpasand *et al.*, "Can an affine model capture the macroscopic response of a non-affine model by appropriate choice of parameters?" *Summer Biomechanics, Bioengineering, and Biotransport Conference*, no. 2, pp. 17–18, 2020.

[65] T. C. Gasser, R. W. Ogden, and G. A. Holzapfel, "Hyperelastic modelling of arterial layers with distributed collagen fibre orientations," *Journal of The Royal Society Interface*, vol. 3, no. 6, pp. 15–35, Feb. 2005. [Online]. Available: https://royalsocietypublishing.org/doi/abs/10.1098/rsif.2005.0073.

[66] M. Nikpasand *et al.*, "Load Transfer from Tissue to Neuron : Computational Analysis of Mechanical Differences between Facet Capsular Ligament and Collagen Gel Experiments," *In preparation*, 2022.

[67] M. Nikpasand *et al.*, "Estimating Cervical Facet Capsular Ligament Mechanics Based on Subject-Specific Anatomy and Kinematics," *In preparation*, 2022.

[68] M. Nikpasand *et al.*, "A Hybrid Microstructural-Continuum Multiscale Approach for Modeling Hyperelastic Fibrous Soft Tissue," *Journal of Elasticity*, vol. 145, no. 1-2, pp. 295–319, Aug. 2021. [Online]. Available: https://doi.org/10.1007/s10659-021-09843-7%20https://link.springer.com/10.1007/s10659-021-09843-7.

[69] G. A. Holzapfel, "Biomechanics of Soft Tissue," in *The Handbook of Materials Behavior Models*, Academic Press, 2001, ch. Champter 1, pp. 1049–1063.

[70] J. D. Humphrey, *Cardiovascular Solid Mechanics*. Springer New York, 2002.

[71] K. Volokh, "On arterial fiber dispersion and auxetic effect," *Journal of Biomechanics*, vol. 61, pp. 123–130, Aug. 2017.

[72] R. Gatt *et al.*, "Negative Poisson's ratios in tendons: An unexpected mechanical response," *Acta Biomaterialia*, vol. 24, pp. 201–208, Sep. 2015.

[73] D. R. Nolan and J. P. Mcgarry, "On the Compressibility of Arterial Tissue," *Annals of Biomedical Engineering*, vol. 44,

[74] F. D. Puccio, S. Celi, and P. Forte, "Review of Experimental Investigations on Compressibility of Arteries and Introduction of a New Apparatus,"

[75] Z. Yosibash *et al.*, "Experimental evidence of the compressibility of arteries," *Journal of the Mechanical Behavior of Biomedical Materials*, vol. 39, pp. 339–354, Nov. 2014.

[76] O. E. Yossef *et al.*, "Further experimental evidence of the compressibility of arteries," *Journal of the Mechanical Behavior of Biomedical Materials*, vol. 65, pp. 177–189, Jan. 2017.

[77] X. Guo and G. S. Kassab, "Variation of mechanical properties along the length of the aorta in C57bl/6 mice," *American Journal of Physiology-Heart and Circulatory Physiology*, 2003.

[78] Y. C. Fung, "Elasticity of soft tissues in simple elongation.," *The American journal of physiology*, vol. 213, no. 6, pp. 1532–1544, 1967.

[79] C. Bellini *et al.*, "A Microstructurally Motivated Model of Arterial Wall Mechanics with Mechanobiological Implications,"

[80] G. A. Holzapfel and R. W. Ogden, "An arterial constitutive model accounting for collagen content and cross-linking," *Journal of the Mechanics and Physics of Solids*, vol. 136, p. 103 682, Mar. 2020.

[81] K. Li, R. W. Ogden, and G. A. Holzapfel, "An exponential constitutive model excluding fibres under compression: Application to extension–inflation of a residually stressed carotid artery," *Mathematics and Mechanics of Solids*, vol. 23, no. 8, pp. 1206–1224, Aug. 2018.

[82] J. K. Cheng *et al.*, "A fiber-based constitutive model predicts changes in amount and organization of matrix proteins with development and disease in the mouse aorta," *Biomechanics and Modeling in Mechanobiology*, vol. 12, no. 3, pp. 497–510, Jun. 2013.

[83] T. C. Gasser, C. A. Schulze-Bauer, and G. A. Holzapfel, "A three-dimensional finite element model for arterial clamping," *Journal of Biomechanical Engineering*, vol. 124, no. 4, pp. 355–363, Aug. 2002.

[84] L. A. Mihai *et al.*, "A family of hyperelastic models for human brain tissue," *Journal of the Mechanics and Physics of Solids*, vol. 106, pp. 60–79, Sep. 2017.

[85] A. A. Claeson and V. H. Barocas, "Planar biaxial extension of the lumbar facet capsular ligament reveals significant in-plane shear forces," *Journal of the Mechanical Behavior of Biomedical Materials*, vol. 65, pp. 127–136, Jan. 2017. [Online]. Available: https://linkinghub.elsevier.com/retrieve/pii/S175161611630279X.

[86] D. Guan *et al.*, "On the AIC-based model reduction for the general Holzapfel–Ogden myocardial constitutive law," *Biomechanics and Modeling in Mechanobiology*, vol. 18, no. 4, pp. 1213–1232, Aug. 2019.

[87] G. A. Holzapfel and R. W. Ogden, "Constitutive modelling of passive myocardium: a structurally based framework for material characterization," *Trans. R. Soc. A*, vol. 367, pp. 3445–3475, 2009.

[88] D. W. Laurence *et al.*, "A pilot ¡i¿in silico¡/i¿ modeling-based study of the pathological effects on the biomechanical function of tricuspid valves," *International Journal for Numerical Methods in Biomedical Engineering*, vol. 36, no. 7, Jul. 2020.

[89] N. M. Shahraki *et al.*, "On the use of biaxial properties in modeling annulus as a Holzapfel-Gasser-Ogden material," *Frontiers in Bioengineering and Biotechnology*, vol. 3, no. JUN, p. 69, Jun. 2015.

[90] T. C. Gasser and G. A. Holzapfel, "Modeling plaque fissuring and dissection during balloon angioplasty intervention," *Annals of Biomedical Engineering*, vol. 35, no. 5, pp. 711–723, May 2007.

[91] E. McEvoy, G. A. Holzapfel, and P. McGarry, "Compressibility and Anisotropy of the Ventricular Myocardium: Experimental Analysis and Microstructural Modeling," *Journal of Biomechanical Engineering*, vol. 140, no. 8, Aug. 2018.

[92] H. Khayyeri *et al.*, "Comparison of structural anisotropic soft tissue models for simulating Achilles tendon tensile behaviour," *Journal of the Mechanical Behavior of Biomedical Materials*, vol. 61, pp. 431–443, Aug. 2016.

[93] C. Laville, C. Pradille, and Y. Tillier, "Mechanical characterization and identification of material parameters of porcine aortic valve leaflets," *Journal of the Mechanical Behavior of Biomedical Materials*, vol. 112, p. 104 036, Aug. 2020.

[94] J. F. Rodríguez *et al.*, "Mechanical stresses in abdominal aortic aneurysms: Influence of diameter, asymmetry, and material anisotropy," *Journal of Biomechanical Engineering*, vol. 130, no. 2, Apr. 2008.

[95] G. A. Holzapfel *et al.*, "Modelling non-symmetric collagen fibre dispersion in arterial walls,"

[96] K. Li, R. W. Ogden, and G. A. Holzapfel, "A discrete fibre dispersion method for excluding fibres under compression in the modelling of fibrous tissues," *Journal of The Royal Society Interface*, vol. 15, no. 138, p. 20 170 766, Jan. 2018.

[97] ——, "Modeling fibrous biological tissues with a general invariant that excludes compressed fibers," *Journal of the Mechanics and Physics of Solids*, vol. 110, pp. 38–53, Feb. 2018.

[98] D. R. Nolan *et al.*, "A robust anisotropic hyperelastic formulation for the modelling of soft tissue," *Journal of the Mechanical Behavior of Biomedical Materials*, vol. 39, pp. 48–60, Nov. 2014. [Online]. Available: https://linkinghub.elsevier.com/retrieve/pii/S1751616114001805.

[99] M. Latorre and F. J. Montáns, "On the tension-compression switch of the Gasser-Ogden-Holzapfel model: Analysis and a new pre-integrated proposal," *Journal of the Mechanical Behavior of Biomedical Materials*, vol. 57, pp. 175–189, Apr. 2016.

[100] A. V. Melnik, H. Borja Da Rocha, and A. Goriely, "On the modeling of fiber dispersion in fiber-reinforced elastic materials," *International Journal of Non-Linear Mechanics*, vol. 75, pp. 92–106, 2015. [Online]. Available: http://dx.doi.org/10.1016/j.ijnonlinmec.2014.10.006.

[101] Y. Lanir, "Constitutive equations for fibrous connective tissues," *Journal of Biomechanics*, vol. 16, no. 1, pp. 1–12, Jan. 1983.

[102] P. L. Chandran and V. H. Barocas, "Affine Versus Non-Affine Fibril Kinematics in Collagen Networks: Theoretical Studies of Network Behavior," *Journal of Biomechanical Engineering*, vol. 128, no. 2, pp. 259–270, 2006.

[103] H. Hatami-Marbini and R. C. Picu, "Effect of fiber orientation on the non-affine deformation of random fiber networks," *Acta Mechanica*, vol. 205, no. 1-4, pp. 77–84, Jun. 2009. [Online]. Available: https://link.springer.com/article/10.1007/s00707-009-0170-7.

[104] C. E. Korenczuk *et al.*, "Ex Vivo Mechanical Tests and Multiscale Computational Modeling Highlight the Importance of Intramural Shear Stress in Ascending Thoracic Aortic Aneurysms," *Journal of Biomechanical Engineering*, vol. 141, no. 12, Dec. 2019.

[105] M. Marino and G. Vairo, "Stress and strain localization in stretched collagenous tissues via a multiscale modelling approach," *Computer Methods in Biomechanics and Biomedical Engineering*, vol. 17, no. 1, pp. 11–30, 2014.

[106] E. J. Weinberg and M. R. Kaazempur Mofrad, "A multiscale computational comparison of the bicuspid and tricuspid aortic valves in relation to calcific aortic stenosis," *Journal of Biomechanics*, vol. 41, no. 16, pp. 3482–3487, Dec. 2008.

[107] E. J. Weinberg and M. R. K. Mofrad, "Three-dimensional, multiscale simulations of the human aortic valve," *Cardiovascular Engineering*, vol. 7, no. 4, pp. 140–155, Dec. 2007.

[108] T. Stylianopoulos and V. H. Barocas, "Multiscale, structure-based modeling for the elastic mechanical behavior of arterial walls," *Journal of Biomechanical Engineering*, vol. 129, no. 4, pp. 611–618, Aug. 2007.

[109] E. Sander *et al.*, "Image-based biomechanics of collagen-based tissue equivalents," *IEEE Engineering in Medicine and Biology Magazine*, vol. 28, no. 3, pp. 10–18, May 2009.

[110] P. Gonc -Alves Coelho, P. R. Fernandes, and H. Carric -O Rodrigues, "Multiscale modeling of bone tissue with surface and permeability control,"

[111] K. M. Virgilio *et al.*, "Multiscale models of skeletal muscle reveal the complex effects of muscular dystrophy on tissue mechanics and damage susceptibility," *Interface Focus*, vol. 5, no. 2, p. 20 140 080, Apr. 2015.

[112] C. E. Korenczuk, V. H. Barocas, and W. J. Richardson, "Effects of Collagen Heterogeneity on Myocardial Infarct Mechanics in a Multiscale Fiber Network Model," *Journal of Biomechanical Engineering*, vol. 141, no. 9, Sep. 2019.

[113] F. Maceri, M. Marino, and G. Vairo, "A unified multiscale mechanical model for soft collagenous tissues with regular fiber arrangement," *Journal of Biomechanics*, vol. 43, no. 2, pp. 355–363, Jan. 2010.

[114] H. Hatami-Marbini, A. Shahsavari, and R. C. Picu, "Multiscale modeling of semiflexible random fibrous structures," *CAD Computer Aided Design*, vol. 45, no. 1, pp. 77–83, Jan. 2013.

[115] T. C. Gasser and G. A. Holzapfel, "Modeling the propagation of arterial dissection," *European Journal of Mechanics, A/Solids*, vol. 25, no. 4, pp. 617–633, Jul. 2006.

[116] N. Horvat *et al.*, "A finite element implementation of a growth and remodeling model for soft biological tissues: Verification and application to abdominal aortic aneurysms," *Computer Methods in Applied Mechanics and Engineering*, vol. 352, pp. 586–605, Aug. 2019.

[117] B. Fereidoonnezhad *et al.*, "A Mechanobiological model for damage-induced growth in arterial tissue with application to in-stent restenosis," *Journal of the Mechanics and Physics of Solids*, vol. 101, pp. 311–327, Jan. 2017.

[118] M. Rolf-Pissarczyk *et al.*, "A discrete approach for modeling degraded elastic fibers in aortic dissection," *Computer Methods in Applied Mechanics and Engineering*, vol. 373, p. 113 511, Jan. 2021.

[119] W. Mao *et al.*, "Fully-coupled fluid-structure interaction simulation of the aortic and mitral valves in a realistic 3D left ventricle model," *PLOS ONE*, vol. 12, no. 9, D. Tang, Ed., e0184729, Sep. 2017.

[120] D. Balzani, S. Brinkhues, and G. A. Holzapfel, "Constitutive framework for the modeling of damage in collagenous soft tissues with application to arterial walls," *Computer Methods in Applied Mechanics and Engineering*, vol. 213-216, pp. 139–151, Mar. 2012.

[121] A. Erdemir *et al.*, "Multiscale cartilage biomechanics: technical challenges in realizing a high-throughput modelling and simulation workflow," *Interface Focus*, vol. 5, no. 2, p. 20 140 081, Apr. 2015.

[122] C. M. Witzenburg *et al.*, "Failure of the Porcine Ascending Aorta: Multidirectional Experiments and a Unifying Microstructural Model," 2017. [Online]. Available: https : / / asmedigitalcollection . asme . org / biomechanical / article - pdf / 139 / 3 / 031005 / 6095215 / bio_139_03_031005.pdf.

[123] L. M. Bersie-Larson *et al.*, "Glomerular filtration and podocyte tensional homeostasis: importance of the minor type IV collagen network," *Biomechanics and Modeling in Mechanobiology*,

[124] R. Mahutga and V. H. Barocas, "Investigation of Pathophysiological Aspects of Aortic Growth, Remodeling, and Failure Using a Discrete-Fiber Microstructural Model," *Journal of Biomechanical Engineering*, vol. 142, no. 11, Aug. 2020.

[125] S. S. Sajjadinia, B. Carpentieri, and G. A. Holzapfel, "A backward pre-stressing algorithm for efficient finite element implementation of in vivo material and geometrical parameters into fibril-reinforced mixture models of articular cartilage," *Journal of the Mechanical Behavior of Biomedical Materials*, p. 104 203, Nov. 2020.

[126] O. Gültekin, H. Dal, and G. A. Holzapfel, "Numerical aspects of anisotropic failure in soft biological tissues favor energy-based criteria: A rate-dependent anisotropic crack phase-field model," *Computer Methods in Applied Mechanics and Engineering*, vol. 331, pp. 23–52, Apr. 2018.

[127] G. A. Holzapfel, M. Stadler, and T. C. Gasser, "Changes in the mechanical environment of stenotic arteries during interaction with stents: Computational assessment of parametric stent designs," *Journal of Biomechanical Engineering*, vol. 127, no. 1, pp. 166–180, Feb. 2005.

[128] G. A. Holzapfel, R. W. Ogden, and S. Sherifova, *On fibre dispersion modelling of soft biological tissues: A review*, 2019.

[129] S. Federico and T. C. Gasser, "Nonlinear elasticity of biological tissues with statistical fibre orientation," *Journal of The Royal Society Interface*, vol. 7, no. 47, pp. 955–966, Jun. 2010. [Online]. Available: https://royalsocietypublishing.org/doi/10.1098/rsif.2009.0502.

[130] C. J. Stender *et al.*, "Modeling the effect of collagen fibril alignment on ligament mechanical behavior," *Biomechanics and Modeling in Mechanobiology*, vol. 17, no. 2, pp. 543–557, Apr. 2018. [Online]. Available: /pmc/articles/PMC5880545/?report=abstract%20https://www.ncbi.nlm.nih.gov/pmc/articles/PMC5880545/.

[131] R. Y. Dhume, E. D. Shih, and V. H. Barocas, "Multiscale model of fatigue of collagen gels," *Biomechanics and Modeling in Mechanobiology*, vol. 18, no. 1, pp. 175–187, Feb. 2019. [Online]. Available: http://link.springer.com/10.1007/s10237-018-1075-y.

[132] R. Y. Dhume and V. H. Barocas, "Emergent structure-dependent relaxation spectra in viscoelastic fiber networks in extension," *Acta Biomaterialia*, vol. 87, pp. 245–255, Mar. 2019.

[133] K. L. Billiar and M. S. Sacks, "Biaxial mechanical properties of the native and glutaraldehyde-treated aortic valve cusp: Part II - A structural constitutive model," *Journal of Biomechanical Engineering*, vol. 122, no. 4, pp. 327–336, 2000.

[134] E. Gacek *et al.*, "Through-thickness Regional Variation in the Mechanical Characteristics of the Lumbar Facet Capsular Ligament," *Biomechanics and Modeling in Mechanobiology*, vol. In Review, 2020.

[135] S. A. Maas *et al.*, "FEBio: Finite elements for biomechanics," *Journal of Biomechanical Engineering*, vol. 134, no. 1, p. 11 005, 2012. [Online]. Available: /pmc/articles/PMC3705975/?report=abstract%20https://www.ncbi.nlm.nih.gov/pmc/articles/PMC3705975/.

[136] S. A. Maas *et al.*, *FEBio User Manual v2.8*, 2018.

[137] B. A. Lane *et al.*, "Constitutive modeling of compressible type-I collagen hydrogels," *Medical Engineering and Physics*, vol. 53, pp. 39–48, Mar. 2018.

[138] M. Böl *et al.*, "Computational modeling of muscular thin films for cardiac repair," *Computational Mechanics*, vol. 43, no. 4, pp. 535–544, Sep. 2009.

[139] T. Eriksson *et al.*, "Influence of myocardial fiber/sheet orientations on left ventricular mechanical contraction," *Mathematics and Mechanics of Solids*, vol. 18, no. 6, pp. 592–606, Aug. 2013.

[140] Z. Win, J. M. Buksa, and P. W. Alford, "Architecture-Dependent Anisotropic Hysteresis in Smooth Muscle Cells," *Biophysical Journal*, vol. 115, no. 10, pp. 2044–2054, Nov. 2018.

[141] S. M. Vanderheiden, M. F. Hadi, and V. H. Barocas, "Crack Propagation Versus Fiber Alignment in Collagen Gels: Experiments and Multiscale Simulation," 2015.

[142] M. F. Hadi *et al.*, "Simulated remodeling of loaded collagen networks via strain-dependent enzymatic degradation and constant-rate fiber growth," *Mechanics of materials : an international journal*, vol. 44, pp. 72–82, Jan. 2012.

[143] S. Zeinali-Davarani *et al.*, "Contribution of collagen fiber undulation to regional biomechanical properties along porcine thoracic aorta," *Journal of Biomechanical Engineering*, 2015.

[144] M. Smoljkić *et al.*, "Biomechanical Characterization of Ascending Aortic Aneurysms," *Biomechanics and Modeling in Mechanobiology*, 2017.

[145] G. A. Holzapfel and R. W. Ogden, "Modelling the layer-specific three-dimensional residual stresses in arteries, with an application to the human aorta," *Journal of the Royal Society, Interface / the Royal Society*, vol. 7, no. 46, pp. 787–799, May 2010.

[146] S. Baek, A. Valentin, and J. D. Humphrey, "Biochemomechanics of cerebral vasospasm and its resolution: II. Constitutive relations and model simulations," *Annals of Biomedical Engineering*, vol. 35, no. 9, pp. 1498–1509, Sep. 2007.

[147] S. P. Cohen and S. N. Raja, "Pathogenesis, Diagnosis, and Treatment of Lumbar Zygapophysial (Facet) Joint Pain," *Anesthesiology*, vol. 106, no. 3, pp. 591–614, 2007.

[148] L. Manchikanti *et al.*, "Is There Correlation of Facet Joint Pain in Lumbar and Cervical Spine? An Evaluation of Prevalence in Combined Chronic Low Back and Neck Pain," *Pain Physician*, vol. 5, no. 4, pp. 365–371,

[149] R. E. BURGESON and M. E. NIMNI, "Collagen Types. Molecular Structure and Tissue Distribution," *Clinical Orthopaedics and Related Research*, vol. 282, no. 282, 250???272, Sep. 1992. [Online]. Available: http://journals.lww.com/00003086-199209000-00033.

[150] J. M. Middendorf *et al.*, "Local tissue heterogeneity may modulate neuronal responses via altered axon strain fields: insights about innervated joint capsules from a computational model," *Biomechanics and Modeling in Mechanobiology*, pp. 1–17, Sep. 2021. [Online]. Available: https://link.springer.com/article/10.1007/s10237-021-01506-9%20https://link.springer.com/10.1007/s10237-021-01506-9.

[151] V. Zarei *et al.*, "Tissue loading and microstructure regulate the deformation of embedded nerve fibres: Predictions from single-scale and multiscale simulations," *Journal of the Royal Society Interface*, vol. 14, no. 135, 2017.

[152] V. W. L. Chan *et al.*, "Image-based multi-scale mechanical analysis of strain amplification in neurons embedded in collagen gel," *Computer Methods in Biomechanics and Biomedical Engineering*, vol. 22, no. 2, pp. 113–129, Jan. 2019. [Online]. Available: https://www.tandfonline.com/doi/full/10.1080/10255842.2018.1538414.

[153] V. K. Lai *et al.*, "Mechanical behavior of collagen-fibrin co-gels reflects transition from series to parallel interactions with increasing collagen content," *Journal of Biomechanical Engineering*, vol. 134, no. 1, Jan. 2012. [Online]. Available: https://asmedigitalcollection.asme.org/biomechanical/article/134/1/011004/455642/Mechanical-Behavior-of-Collagen-Fibrin-Co-Gels.

[154] C. Korenczuk, V. Lai, and V. Barocas, "Quasilinear and Non-Quasilinear Viscoelastic Behavior of Collagen Gels During Stress Relaxation," *Summer Biomechanics, Bioengineering, and Biotransport Conference*, 2015.

[155] J. Marcelin, S. Singh, and B. A. Winkelstein, "MACROSCALE & MICROSCALE RESPONSES OF THE RAT LUMBAR FACET CAPSULAR LIGAMENT TO SUBFAILURE REPEATED CYCLIC LOADING & A RAMP-AND-HOLD," *Summer Biomechanics, Bioengineering and Biotransport Conference*, 2021.

[156] R. Fadić, J. Vergara, and J. Alvarez, "Microtubules and caliber of central and peripheral processes of sensory axons," *Journal of Comparative Neurology*, vol. 236, no. 2, pp. 258–264, Jun. 1985. [Online]. Available: https://onlinelibrary.wiley.com/doi/full/10.1002/cne.902360209%20https://onlinelibrary.wiley.com/doi/abs/10.1002/cne.902360209%20https://onlinelibrary.wiley.com/doi/10.1002/cne.902360209.

[157] H. Ouyang, E. Nauman, and R. Shi, "Contribution of cytoskeletal elements to the axonal mechanical properties," *Journal of Biological Engineering*, vol. 7, no. 1, pp. 1–8, Sep. 2013. [Online]. Available: https://jbioleng.biomedcentral.com/articles/10.1186/1754-1611-7-21.

[158] F. J. Ahmad *et al.*, "Motor proteins regulate force interactions between microtubules and microfilaments in the axon," *Nature Cell Biology 2000 2:5*, vol. 2, no. 5, pp. 276–280, Apr. 2000. [Online]. Available: https://www.nature.com/articles/ncb0500_276.

[159] L. Manchikanti *et al.*, "Prevalence of Cervical Facet Joint Pain in Chronic Neck Pain," *Pain Physician*, vol. 5, no. 3, pp. 243–249,

[160] B. Peng and N. Bogduk, "Cervical Discs as a Source of Neck Pain. An Analysis of the Evidence," *Pain Medicine*, vol. 20, no. 3, pp. 446–455, Mar. 2019. [Online]. Available: https://academic.oup.com/painmedicine/article/20/3/446/5232305.

[161] A. M. Ellingson and D. J. Nuckley, "Altered helical axis patterns of the lumbar spine indicate increased instability with disc degeneration," *Journal of Biomechanics*, vol. 48, no. 2, pp. 361–369, 2015. [Online]. Available: http://dx.doi.org/10.1016/j.jbiomech.2014.11.010.

[162] B. R. Kaale *et al.*, "Head position and impact direction in whiplash injuries: associations with MRI-verified lesions of ligaments and membranes in the upper cervical spine," *Journal of neurotrauma*, vol. 22, no. 11, pp. 1294–1302, Nov. 2005. [Online]. Available: https://pubmed.ncbi.nlm.nih.gov/16305317/.

[163] M. S. Caird *et al.*, "Isolated alar ligament disruption in children and adolescents as a cause of persistent torticollis and neck pain after injury: A report of three cases," *Journal of Bone and Joint Surgery - Series A*, vol. 91, no. 11, pp. 2713–2718, Nov. 2009. [Online]. Available: https://journals.lww.com/jbjsjournal/Fulltext/2009/11000/Isolated_Alar_Ligament_Disruption_in_Children_and.25.aspx.

[164] W. J. Anderst, "Bootstrap prediction bands for cervical spine intervertebral kinematics during in vivo three-dimensional head movements," *Journal of Biomechanics*, vol. 48, no. 7, pp. 1270–1276, May 2015. [Online]. Available: https://linkinghub.elsevier.com/retrieve/pii/S0021929015001463.

[165] C. C. Kage *et al.*, "Validation of an automated shape-matching algorithm for biplane radiographic spine osteokinematics and radiostereometric analysis error quantification," *PLOS ONE*, vol. 15, no. 2, X. Zhang, Ed., e0228594, Feb. 2020. [Online]. Available: /pmc/articles/PMC7021291/%20/pmc/articles/PMC7021291/?report=abstract%20https://www.ncbi.nlm.nih.gov/pmc/articles/PMC7021291/%20https://dx.plos.org/10.1371/journal.pone.0228594.

[166] L. Liang *et al.*, "A Machine Learning Approach to Investigate the Relationship between Shape Features and Numerically Predicted Risk of Ascending Aortic Aneurysm HHS Public Access," *Biomech Model Mechanobiol*, vol. 16, no. 5, pp. 1519–1533, 2017.

[167] E. L. Brainerd *et al.*, "X-ray reconstruction of moving morphology (XROMM): precision, accuracy and applications in comparative biomechanics research," *Journal of Experimental Zoology Part A: Ecological Genetics and Physiology*, vol. 9999A, no. 5, n/a–n/a, Jun. 2010. [Online]. Available: https://onlinelibrary.wiley.com/doi/full/10.1002/jez.589%20https://onlinelibrary.wiley.com/doi/abs/10.1002/jez.589%20https://onlinelibrary.wiley.com/doi/10.1002/jez.589.

[168] B. Akhbari *et al.*, "Accuracy of biplane videoradiography for quantifying dynamic wrist kinematics," *Journal of biomechanics*, vol. 92, pp. 120–125, Jul. 2019. [Online]. Available: https://pubmed.ncbi.nlm.nih.gov/31174845/.

[169] A. Fujiwara *et al.*, "The Effect of Disc Degeneration and Facet Joint Osteoarthritis on the Segmental Flexibility of the Lumbar Spine," *Spine*, vol. 25, no. 23, pp. 3036–3044, Dec. 2000. [Online]. Available: http://journals.lww.com/00007632-200012010-00011.

[170] A. C. Gellhorn, J. N. Katz, and P. Suri, "Osteoarthritis of the spine: the facet joints," *Nature Reviews Rheumatology*, vol. 9, no. 4, pp. 216–224, Apr. 2013. [Online]. Available: /pmc/articles/PMC4012322/%20/pmc/articles/PMC4012322/?report=abstract%20https://www.ncbi.nlm.nih.gov/pmc/articles/PMC4012322/%20http://www.nature.com/articles/nrrheum.2012.199.

[171] M. S. Park *et al.*, "Facet Joint Degeneration of the Cervical Spine," *Spine*, vol. 39, no. 12, E713–E718, May 2014. [Online]. Available: https://journals.lww.com/spinejournal/Fulltext/2014/05200/Facet_Joint_Degeneration_of_the_Cervical_Spine__A.8.aspx%20http://journals.lww.com/00007632-201405200-00008.